Remote Sensing Systems for Ocean: A Review (Part 2: Active Systems)

Meisam Amani ⓘ, *Senior Member, IEEE*, Farzane Mohseni, Nasir Farsad Layegh ⓘ,
Mohsen Eslami Nazari ⓘ, *Member, IEEE*, Farzam Fatolazadeh, Abbas Salehi, Seyed Ali Ahmadi ⓘ,
Hamid Ebrahimy, Arsalan Ghorbanian ⓘ, Shuanggen Jin ⓘ, *Senior Member, IEEE*, Sahel Mahdavi ⓘ,
and Armin Moghimi ⓘ

Abstract—As discussed in the previous part of this review article, remote sensing (RS) creates unprecedented opportunities by providing a variety of systems with different characteristics to study and monitor oceans. Part 1 of this review article was dedicated to reviewing passive RS systems and their main applications in the ocean. Here, in part 2, seven active RS systems, including scatterometers, altimeters, gravimeters, synthetic aperture radar, light detection and ranging, sound navigation and ranging, high-frequency radars are comprehensively reviewed. For consistency, this part is structured similarly to part 1. The aforementioned systems, along with their characteristics and primary applications, are introduced in separate sections. This review article provides useful information to all students and researchers who are interested in the oceanographic applications of active RS systems.

Index Terms—Altimeter, gravimeter, high-frequency (HF) Radar, lidar, ocean, remote sensing, synthetic aperture radar (SAR), scatterometer, sound navigation and ranging (SONAR).

I. INTRODUCTION

OCEANS covering more than two-thirds of the earth's surface, provide numerous services. Thus, it is crucial to

Meisam Amani and Sahel Mahdavi are with the Wood Environment and Infrastructure Solutions, Ottawa, ON K2E 7L5, Canada (e-mail: meisam.amani@woodplc.com; sahel.mahdavi@woodplc.com).

Farzane Mohseni, Abbas Salehi, Seyed Ali Ahmadi, Arsalan Ghorbanian, and Armin Moghimi are with the Department of Photogrammetry and Remote Sensing, Faculty of Geodesy and Geomatics Engineering, K. N. Toosi University of Technology, Tehran 1969764999, Iran (e-mail: farzanemohseni@ymail.com; ab.s1989@mails.ucas.ac.cn; cpt.ahmadisnipiol@yahoo.com; a.ghorbanian@email.kntu.ac.ir; moghimi.armin@gmail.com).

Nasir Farsad Layegh is with the Capgemini Invent, 3543 KA Utrecht, The Netherlands (e-mail: farsad_layegh@yahoo.com).

Mohsen Eslami Nazari is with the Memorial University of Newfoundland, St. John's, NL A1C5S7, Canada (e-mail: mohsen.nazari@mun.ca).

Farzam Fatolazadeh is with the Centre d'applications et de recherches en télédétection, Département de Géomatique appliquée Université de Sherbrooke, Sherbrooke, QC J1K 2R1, Canada (e-mail: farzam.fatolazadeh@usherbrooke.ca).

Hamid Ebrahimy is with the Center for Remote Sensing and GIS Research, Faculty of Earth Sciences, Shahid Beheshti University, Tehran 19839 69411, Iran (e-mail: h_ebrahimy@sbu.ac.ir).

Shuanggen Jin is with the School of Remote Sensing and Geomatics Engineering, Nanjing University of Information Science and Technology, Nanjing 210044, China, and also with the Shanghai Astronomical Observatory, Chinese Academy of Sciences, Shanghai 200030, China (e-mail: sgjin@shao.ac.cn).

Digital Object Identifier 10.1109/JSTARS.2022.3141980

TABLE I
CLASSIFICATION OF THE ACTIVE RS SYSTEMS BASED ON THE RANGES OF THE SPECTRUM

RS systems	Wavelength (µm)	Frequency (GHz)
Scatterometer	2.0×10^4 - 6.0×10^4	5.0 – 15.0
Altimeter	7.5×10^3 - 1.0×10^5	3.0 – 40.0
Gravimetry	13.0×10^4 - 15.0×10^4	2.0 - 2.3
SAR	25.0×10^3 - 1.0×10^6	0.3 – 12.0
LiDAR	$0.3 – 1.0$	3×10^5 - 1.0×10^6
SONAR	15.0×10^2-15.0×10^6	1.0×10^{-6} - 1.0×10^{-3}
HF Radar	1.0×10^7 - 1.0×10^8	$3 \times 10^{-3} – 3 \times 10^{-2}$

monitor these valuable resources using advanced technologies, such as remote sensing (RS, see Table III for the list of acronyms) systems. RS systems provide a wide range of datasets for various oceanographic applications. The capability to collect data at various temporal and spatial scales, along with the possibility for retrospective analyses of oceanographic parameters, has turned the applications of RS systems into a must.

RS systems can be generally divided into two broad groups of passive and active. The Part 1 of this review article was about the passive systems for ocean studies (see [1] for more details). In this part of the article, various active RS systems for ocean studies are discussed. It should be noted that the main focus of this review article is on the spaceborne active RS systems for oceanographic applications. However, two nonspaceborne active RS systems (i.e., sound navigation and ranging (SONAR), and high frequency (HF) radar) are also discussed due to their important applications in ocean environments.

Active RS systems mostly measure the backscattering radiation from different objects on earth at different parts of the electromagnetic spectrum (see Table I). Scatterometer (SCA), altimeter, gravimeter, synthetic aperture radar (SAR), light detection and ranging (LiDAR), SONAR, and HF radar are the most commonly used active systems for ocean studies. For many oceanographic applications, active RS systems outperform passive systems because they have their own source of illumination and can operate at any time and in almost any weather conditions [2]. Therefore, they are the major systems for ocean mapping and monitoring over different areas, especially polar regions, which are covered by clouds, and the darkness is prevalent most of the time.

Before discussing various active RS systems for ocean studies, several concepts, such as orbit, swath, spatial and temporal

resolutions, polarization, and frequency, which are required to better understand the descriptions of these systems are provided below.

The paths of the satellite tracks are known as its orbits, which are based on the imaging mechanism and objectives of the sensor(s) mounted on the RS platforms [3]. Depending on the orbital characteristics (e.g., orbital geometry and repeat cycle), RS systems can mainly be categorized into two groups of geosynchronous and sun-synchronous [4], [5]. A geosynchronous satellite is an earth-orbiting satellite with the same direction that earth rotates. These satellites are located at an altitude around $35\,800\ Km^2$ over a specific location on earth. Telecommunication and meteorological satellites are examples of geosynchronous satellites [3]. In contrast, sun-synchronous satellites are on orbits with high inclination angles travelling nearly over the Polars, coordinately with the rotation of the sun. Thus, these satellites can continuously observe a point on the earth at a constant local time of day (i.e., local sun time), making them helpful for different RS applications [3], [4].

Most of active RS systems are in near-polar orbits and collect data in both ascending and descending passes [5], [6]. The sun-synchronous RS satellites revisit and obtain data from a specific location within a time range, which is called temporal resolution [7]. Accordingly, polar regions are scanned on every orbit repeat cycle by these satellites. Consequently, the polar/high latitude regions are imaged more than the equatorial zone due to the increasing overlap of adjacent orbital swaths in such areas [8]. The swath is denoted as an area imaged on the earth surface by a system, typically varying from tens to hundreds of kilometers, depending on the types of air/spaceborne RS systems. Active RS sensors operated in either nadir-looking or side looking geometries [7], [8].

In nadir-looking active systems (e.g., altimeters), the scanned ground swath is a function of the instrument's scan angle and flying height, while the antenna width is also crucial in side-looking systems (e.g., SAR) [8]. The pulses of such side-looking systems hit the earth surface, enhancing physical features (e.g., subtle folds) [9]. The spatial resolution of data derived from nadir-looking systems is defined only in a single direction (i.e., azimuth direction), while this is described in two directions of range and azimuth for side looking systems [6].

The range resolution depends on the pulse duration and is independent of the distance between the RS system and scatterer. This can be expressed into two formats, including slant range and ground range resolutions (i.e., projection of the slant plane onto the ground plane). The azimuth resolution is a function of the sensor wavelength, slant range, and antenna length. Accordingly, the higher spatial resolution for a given wavelength is generated by the longer the antenna, which is impractical for a spaceborne satellite. Such a limitation means that real aperture radar systems (e.g., scatterometers) could not have a high spatial resolution, but still can acquire high radiometric resolution data. To address this limitation, researchers developed SAR systems that synthesize a long antenna aperture by storing the data collected sequentially and coherently from a physically shorter antenna and, then, processing them, resulting in much higher spatial resolution data. Accordingly, the SAR azimuth resolution is equal to half of the antenna length. Thus, the lesser the antenna length, the better the resolution by considering ambiguity conditions [6], [9]–[11].

Most active RS systems employ visible/near-infrared (e.g., LiDAR) and microwave waves (e.g., SAR, SCA, radar altimeter, and HF radar). For example, LiDAR typically uses a laser beam for detecting the distance between the sensor and the object, while SONAR uses an acoustic beam for this purpose. Moreover, radar altimeters generally utilize microwave beams to determine the altitude of an object above a fixed level (e.g., ocean surface) [3], [9], [12].

Active RS systems generally record data either in single or multiple channels in terms of integrating frequency channels. These systems can also gather data in different polarizations by governing the analyzed polarization in both the transmit and receive paths [6], [13], [14]. For example, if the polarized energy is vertically/horizontally transmitted and received, it is indexed by VV/HH (known as copolarized data). Moreover, if the polarized energy is vertically transmitted and horizontally received, or vice versa, it is indexed by VH/HV (known as cross-polarized data). Accordingly, the microwave systems can be categorized into two main groups: single-polarization (or single-pol) and multiple polarization (or multipol). For example, European Sentinel 1 and Canadian RADARSAT-2 SAR systems are dual and quad-polarization satellites [11].

In the following seven sections, detailed discussions are provided about seven active RS systems, which are commonly employed for various oceanographic applications. Within each section, a brief introduction of the systems and their main characteristics are first provided. Then, different systems, which have been so far launched or have been planned to launch are discussed. Finally, the oceanographic applications of the systems are briefly explained.

II. SCATTEROMETER

SCAs are active high-frequency microwave systems that are commonly used for ocean applications [15]. As an active sensor, a SCA emits pulses at a well-defined frequency and polarization to the ocean from an aircraft or a satellite. Information on the sea surface roughness or short gravity waves can be extracted by recording and analyzing the reflection or backscattering of the emitted pulses [16].

Over the ocean, the scattering process, occurring by the interaction between the radar signal and the surface, is defined by the Bragg scattering concept. Here, the wavelength of the scattering components on the ocean surface waves has a distinct relationship to the emitted microwave pulse [6]. SCAs take advantage of this relationship, making it unique among satellite-based ocean sensors due to their capabilities in determining the ocean surface wind (OSW) speed and direction. This is performed by studying the radar signal interaction with distinct scattering elements of the ocean surface called gravity-capillary waves. These waves are surface elements that are centimeter-level ripples on the water surface. The main assumption is that there is a direct relationship between the amplitude and directional movement

of the gravity-capillary waves and the speed and direction of the OSW [17].

The power of the received backscattering signal from the ocean is defined by the backscattering coefficient, or the normalized radar cross section of the ocean surface, which is a function of 1) azimuth and incident angles, 2) radar polarization, 3) radar wavelength, 4) wind speed, 5) relative wind direction, 6) surface reflectivity, and 7) surface objects, such as sea ice (SI) sheets. The azimuth and incident angles are horizontal and vertical angles between the radar look direction and the relative wind direction and scattering surface, respectively, which are determined from sensor observation geometry. Radar polarization and wavelength are fixed values representing the SCA characteristics [18]. The other parameters are related to OSW and surface dynamics and are characterized by local air-sea interaction. According to previous studies, these parameters are highly influential on the strength of the backscattering signal received from the ocean surface [15].

A. Systems

Different satellites that have carried or are carrying SCAs are briefly provided in Table IV and are discussed in more detail in the following.

The first SCA in space was the SeaSat-A/Scatterometer System (SASS) launched by the National Aeronautics and Space Administration (NASA) in 1978. Despite its short lifetime, the three-month data acquisition of the SASS demonstrated the capability of SCAs for OSW measurements [19]. The SASS had four antennas, two on each side of the satellite, pointing at respectively 45°, 135°, 225°, and 315° with respect to the ground track, limiting its coverage to four locations. The SASS worked by irradiating the target twice, first with a fore beam and then a few seconds later with the aft beam. Therefore, each target had two backscattering measurements obtained with a 90° difference in azimuth. For each received backscattering signal, the OSW speed was derived as a function of all possible OSW directions. The SASS can provide global coverage in 1.5 days. The main limitation of the SASS was the directional ambiguity phenomenon. In this phenomenon, even though the different measurements (obtained with 90° apart in azimuth) result in the same OSW speed, the OSW direction for each measurement is different. In the case of SASS, this was negatively affecting its capability in accurately determining OSW directions due to the uncertainty caused by ambiguities in the results [20], [21].

Two decades later, the European Remote-Sensing Satellite-1 (ERS-1) and ERS-2 were launched by the European Space Agency (ESA) in 1991 and 1995, respectively. These satellites were carrying the Advanced Microwave Instrument (AMI) SCA. Both SCAs were identical and had three antennas pointing at azimuth angles of 45°, 90°, and 135° in vertical polarization mode. The AMI operated by having a fore beam with the incidence angle ranging between 22° and 59°, and the aft beam between 18° and 51°. Three view angles resulted in two OSW speed estimates, and the most accurate one was selected by comparing with the Numerical Weather Prediction (NWP) models [17]. The AMI SCAs had a global ocean coverage within 3 days

on average. Stoffelen and Anderson [22] described the estimation of a backscatter-wind relationship using the AMI measurements in more detail.

In August 1996, the NASA Scatterometer (NSCAT) was launched onboard the Japanese satellite ADEOS. The NSCAT had three antennas on each side. On the left side, swaths were at angles of 45°, 65°, and 135° relative to the flight direction, and on the right side, the swaths were at angles of 45°, 115°, and 135°. As a result of this scanning pattern, the NSCAT could determine the OSW speed and direction of the global ocean surface in 1.5 days. The main advantage of having a set of antennas on each side of the satellite was that the NSCAT could observe two swaths simultaneously, allowing for better spatial coverage. The NSCAT was operational until June 1997 [23].

Following the loss of NSCAT, NASA developed the Sea-Winds SCA, which was launched onboard the QuickSCAT and ADEOS-2 satellites in 1999 and 2002, respectively. The SeaWinds was designed to measure OSW close to the ocean's surface with high precision and unprecedented spatial resolution. Its design differed from previous SCAs by having two spot beams on a rotating 1-m reflector dish antenna, allowing for data collection in a circular pattern. The ADEOS-2 satellite was operational for a short time, and the main achievements of the SeaWinds SCA were accomplished onboard the QuickSCAT satellite. The QuickSCAT had the ability to collect data in all weather conditions except extreme conditions, such as very heavy rains, and was able to cover the global ocean every day with an accuracy of 2 m/s. The QuickSCAT was operational until 2009 [24].

The Advanced SCAs (ASCAT-A, -B, -C) were onboard the three satellites launched in 2006, 2012, and 2018, respectively, as part of the Meteorological Operational Satellite Program (METOP), a joint program between ESA and the European Organization for the Exploitation of Meteorological Satellites (EUMETSAT). The METOP satellites are equipped with the same SCA, ASCAT. The ASCAT has a total of six antennas, three looking to the left-hand side of the satellite and three looking to the right. The antennas of each side are directed at 45°, 90°, and 135° angles relative to the flight direction. This design with sets of three antennas reduces the directional ambiguity challenge. The ASCAT simultaneously measures over two swaths of 550 km and, thus, can cover the global ocean within two days [25]. For example, Fig. 1 illustrates seasonal offshore OSW speed maps over the Ireland's offshore environment derived from ASCAT [26]. The authors reported that the accuracies of these maps were considerably high when compared to *in situ* data (Pearson coefficient = 0.95).

The Indian Space Research Organisation (ISRO) launched OceanSat-2 with Oceansat Scatterometer (OSCAT) onboard in September 2009. The OSCAT measures the OSW vectors with comparable quality to QuikSCAT [27]. The OSCAT scans the ocean surface with circular patterns, similar to the QuikSCAT. However, it was improved by using a rotating antenna with two beams to provide four views of each spot from different angles (i.e., incidence angles of 42.66° and 49.33°). The OSCAT provides global coverage every day with a swath size of 1800 km in a day and outperforms side-looking SCAs [28].
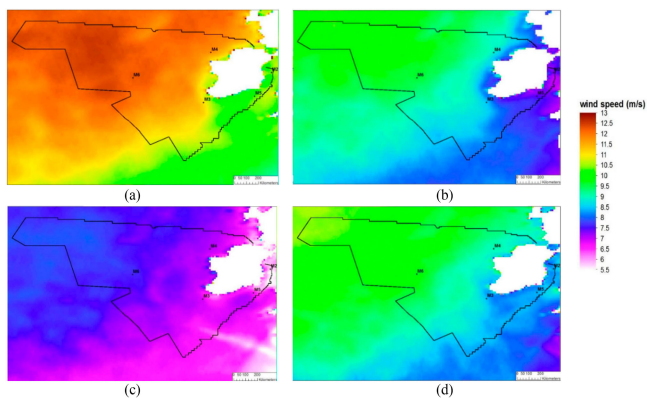
Fig. 1. Seasonal offshore OSW speed maps $(\mathrm{m.s}^{-1})$ over the Ireland's offshore area retrieved between January 2012 and May 2017.

The HSCAT was launched in 2011 onboard the Haiyang (HY-2A) satellite by the Chinese National Space Administration (CNSA). HY-2A is a follow-up to the HY-1, the first series of ocean dynamics observation satellites by China, with the capability of operating in all weather conditions and 24 h a day, similar to other SCAs. The HY-2A is designed similarly to the QuickSCAT and the Indian OceanSat-2 with a 1-m rotating antenna with two beams, achieving four looks for each observed spot. The HSCAT has daily near-global coverage. Although the HSCAT is generally considered accurate as of the SeaWinds and ASCAT, it has several limitations, which are described in [29]. The HSCAT on HY-2A became inactive in November 2020. However, HSCAT was launched onboard HY-2B, HY-2C and HY-2D satellites in 2019, 2020, and 2021, respectively. The HSCAT is expected to be operational on HY-2B, HY-2C, and HY-2D until 2023, 2025, and 2026, respectively.

In 2014, the RapidScat SCA was mounted on the International Space Station (ISS) for a two-year mission. The main goal of the ISS-RapidScat was to mitigate the loss of QuikSCAT, which failed after almost a decade. The RapidScat covered oceans within the latitude of +/- 56° in 2 days with comparable measurement accuracy to the SeaWinds. This instrument's hardware consisted of the QuikSCAT's engineering model hardware except for its antenna diameter, which was reduced to 0.75 m. The most distinguishing feature of the RapidScat compared to all other space-borne SCAs was its capability of daily and semidaily measurements over seasonal time scales [30]. The RapidScat was operational until August 2016.

In 2018, the Chinese-French Oceanography Satellite (CFOSAT) was launched as the joint mission of Chinese and French space agencies carrying a wind SCA called CSCAT. The CSCAT is the first rotating fan-beam SCA with a dual antenna system. This concept enables the instrument to scan with a larger range of incidence angles (i.e., 26° to 46°) and also produce larger swaths with overlaps, resulting in diversity in observation geometry and an improvement in the quality of the ocean backscattering measurement [31]. The CSCAT can cover the global ocean surface within one week with the OSW speed accuracy of 2 m/s. The OSW direction accuracy is also ±20° within the 360° OSW direction range [32].

The Feng-Yun 3-E meteorological satellite was launched in July 2021, carrying the Wind Radar SCA (WindRad). Similar to CSCAT, WindRad is also utilizing a rotating fan-beam design but with different characteristics. However, in contrast to CSCAT, which uses two fan-beams operating in Ku-band, WindRad has four fan-beams with the HH and VV polarizations, two of them operate in C-band and the other two work in Ku-band. Since C-band is less affected by the atmospheric liquid water (e.g., rain and cloud effects) than the Ku-band and is more sensitive to ionospheric perturbation, using it in combination with the Ku-band observations yields more accurate results rectification of the ionospheric delay. Moreover, using the potential of dual frequency WindRad SCA leads to more accurate OSW measurements and results in more robust rain data. Additionally, WindRad can provide near-real-time OSW vector measurements with better spatial resolutions (i.e., 10 km in Ku-band and 30 km in C-band). Finally, it should be noted that since WindRad is a new SCA class, it needs more advanced calibration/cross-calibration [33], [34].

In 2021, the launch of a new series of satellites is expected to begin as a part of the ESA and EUMETSAT program METOP. For example, the METOP-SG-B is planned to be launched in 2022 with the SCA onboard. The SCA has six fixed fan-beam antennas similar to the previous METOP SCA (i.e., ASCAT). Three antennas operate on each side at 45°, 90°, and 135°, related to the flight direction. Compared to the predecessor ASCAT, the SCA has improved coverage, achieved partly by a lower minimum incident angle (20° compared to 25° for ASCAT). The lower incident angle results in a reduced data gap at nadir, which cannot be avoided with the fixed fan-beam design. The SCA has reduced the data gap by approximately 150 km [35]. This allows for the SCA to achieve near global coverage every 1.5 days, an improvement from ASCAT (97%). Besides coverage, the SCA also improves the current spatial resolution and radiometric stability and provides additional polarizations.

B. Applications

SCAs have been used for a variety of oceanographic applications. In this section, the main two oceanographic applications of SCAs (i.e., OSW and SI) are discussed.

1) Ocean Surface Wind: The main application of SCAs has been in determining OSW speed/direction. Some specific examples of using OSW derived by SCAs are the prediction of tropical cyclones [36], [37], identifying cold pools over the oceans [38], selecting the optimal locations for OSW energy infrastructures [26], improving NWP models [39], and deriving numerical models of ocean circulation [40], [41]. For example, Valkonen *et al.* [39] used the ASCAT data to study the capability of SCA data in improving weather forecast at high latitudes (e.g., Northern Europe). *In situ* observations of coastal stations were used for validation, suggesting improvements in OSW speed and mean sea-level pressure determination for a short-term forecast. Moreover, Garg *et al.* [38] developed a new technique based on the ASCAT data for cold pools identification over oceans. Validation of the results of the ASCAT-identified cold pools with buoy measurements showed a low false alarm rate

($<10\%$), high critical success index ($>85\%$), and a low bias (~1). Additionally, Remmers *et al.* [26] utilized the ASCAT data to select the optimal locations of offshore renewable energy infrastructures in Ireland. The obtained results using the ASCAT 12.5 km OSW speed data proved the capability of the ASCAT OSW products in selecting optimal offshore wind farms. Furthermore, Jaiswal *et al.* [42] developed a new method using the OSCAT OSW to predict the tropical cyclones genesis over the North Indian Ocean, where they achieved 100% probability of detection and 2% of the false alarm rate. Additionally, Xu *et al.* [43] developed a new method to retrieve OSW speed in typhoon conditions by combining HSCAT and microwave radiometer data from the HY-2A satellite. Comparing with global/regional assimilation and prediction system data, they could obtain the improved OSW speed values. Finally, Ebuchi [44] assessed the quality of OSW products measured by the RapidScat, and compared them with those collected by buoys. Their results proved that the OSW products of the RapidScat had comparable quality as the previous SCAs (e.g., QuikScat), and no significant systematic error was being produced by the RapidScat.

2) Sea Ice: One of the important applications of SCAs is to study the characteristics and age of SI. SCA data make it possible to measure the size, thickness, and flow of SI, as well as to track its movement. The received backscatter signals depend on the volume of SI, which leads to distinct properties of polarization, intensity, and directional scattering that allow their efficient separation [45]. Continuous monitoring of SI in polar regions using scatterometry has been done using C-band SCAs of ERS and ASCAT and Ku-band QuikSCAT. [46]. For example, Yackel *et al.* [45] developed a methodological framework for estimating relative snow thickness on first-year SI based on the data acquired by ASCAT and QuikSCAT. They investigated the capability of C- and Ku-band for this objective. The results showed that the approach could provide a relative measure of snow thickness in both bands.

III. ALTIMETER

Altimeters are active RS systems that measure ocean surface topography at vertical incidence [47], [48]. To this end, they measure the time elapsed between transmitting and receiving a pulse of electromagnetic energy between the satellite antenna and the ocean's surface [49]. This pulse can be visible/infrared (laser altimeters) or microwave (radar altimeters) [50]. Each of these two systems has its benefits in terms of measurement accuracy, resolution, coverage, and lifespan [51]. The main limitation of the laser altimeter is the fact that it cannot measure through thick clouds [51]. The laser altimeter, which is basically a spaceborne LiDAR, is comprehensively explained in Section VI. Therefore, in this section, the microwave radar altimeters that have been mostly used for oceanographic applications are discussed.

The spaceborne radar altimeters are active microwave systems that were initially designed to measure the topography of sea surface and open ocean level by combining radar and positioning techniques [52]. To this end, a short microwave pulse is transmitted by the radar antenna into the ocean surface and measure the elapsed between emitted and backscattered pulse, enabling range computation between the sensor and the ocean [53]. Simultaneously, an independent tracking system records the three-dimensional (3-D) position of the radar antenna [54], [55]. The output of the radar altimetry measurements is sea surface height (SSH) which is derived by subtracting the measured altimeter range from satellite altitude (i.e., relative to a reference ellipsoid). SSH contains information about ocean wave height (OWH), tides, currents, and the loading of atmospheric pressure [56].

The payload of each altimeter contains two main geometric measuring instruments: 1) a nadir-looking radar altimeter, either mono-frequency or dual-frequency; and 2) an instrument based on Global Positioning System (GPS) constellation for precise orbit determination of the altimeter [57]. Fig. 2 shows a schematic summary of a hypothetical altimeter measurement.

In Fig. 2, H is the satellite orbit altitude relative to a reference ellipsoid measured using GPS instruments and precise observations. Furthermore, R is the distance between the radar antenna and the ocean surface estimated using the two-way travel time of microwave radiation pulse computations. SSH (i.e., h in Fig. 2) can be extracted by subtracting the altimeter range measurement R from H [55]. This information has been used to measure various ocean surface-related characteristics, including geoid and dynamic topography.

The geoid is defined as the equal gravity potential surface of the Earth. It is also considered the vertical datum origin with zero elevation and is commonly defined by spherical harmonics terms. Since geoid is not explicitly identified with high precision, the mean sea level (MSL) is considered a close approximation of the geoid. The ocean surface takes the shape of the geopotential field and the geoid in the absence of disturbing forces, such as OSW, ocean surface current (OSC), and ocean tide (OT). By this, the measurements of altimeters can be used as an essential data for predicting the marine geoid [58]. On the other hand, dynamic ocean topography (DOT) is the difference between the SSH retrieved from altimetry measurements and independent accurate geoid models [59]. Generally, the geoid and DOT are not exactly coincident and have a vertical difference of approximately 1 m [55], [60].

Several different microwave bands, such as Ku-band (13.6 GHz), C-band (5.3 GHz), S-band (3.2 GHz), and Ka-band (35 GHz), have been so far used for ocean studies [61]–[63]. Regulations, technical feasibilities, and mission goals are dominant factors of each project, which should be considered for band frequency determination of altimeters. For example, dual-frequency altimeters were designed to estimate the content of ionospheric electrons and to correct their impact (i.e., delay) on the altimeter measurements [64]. Generally, Ku- and C-bands are the most commonly used frequencies. Ku-band is one of the most optimal bands in terms of technology capabilities, bandwidth availabilities, atmospheric perturbations, and ionospheric electrons perturbation [61]. On the other hand, C-band is more sensitive to ionospheric disturbances and has lower sensitivity to atmospheric liquid water [65]. It is worth noting that a microwave radiometer carried by the same platform, measures atmospheric water content (i.e., both liquid and water vapor)
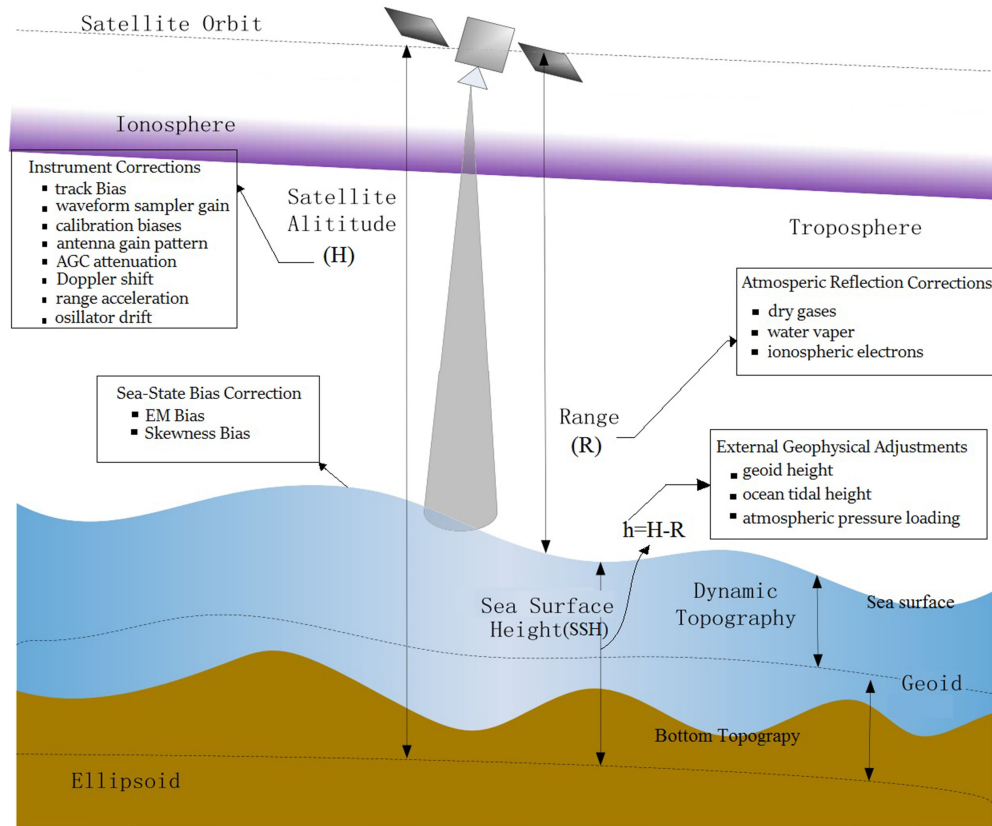
Fig. 2.   Schematic diagram of space-based radar altimeter system.

in the altimeter field of view to compute the propagation delay [66], [67].

Although various oceanographic parameters were extensively studied by altimeters, several challenges remain that limit their applicability. The main limitation of radar altimeters is their coarse-scale spatial resolution (typically 2 km to 18 km) due to their measurement geometry (i.e., nadir direction measurements). To address this issue, scholars have proposed various interferometry-based solutions, such as wide-swath ocean altimeter (WSOA) for global ocean mapping with centimetric accuracy [68]. More information on WSOA can be found in [69] and [70]. Another challenge of radar altimetry is its inability to maintain track over regions of large surface slope [51]. It means that the existence of a high difference between the known field elevation and the altitude retrieved from the altimeter will result in a significant error in altimetric measurements. For example, a case study over Antarctica and Greenland showed that at a surface slopes of 0.7° to 0.8°, the measurements made by different radar altimeters differ by about 26 m [51].Therefore, the accuracy of the altimetry measurement decreases when high frequency energetic barotropic motions exist in oceans. This issue should be addressed using an appropriately rated repair station for evaluation and possible corrections [71]. Finally, there are also multiple challenges when using radar altimetry for OT studies. Given that space-based altimeters are usually sun-synchronous, they observe semidiurnal OT constituents as stationary. These types of sensors always see tidal constituents at

the same point in their cycle and, thus, cannot accurately model the tidal cycles [58].

A. Systems

In response to the critical importance of global ocean topography and the lack of comprehensive data, the international community has established high-priority radar altimeter satellite missions designed to acquire and produce high-quality global ocean topography data. Table V summarizes several main spaceborne radar altimeters along with their main characteristics for ocean studies. It should be noted that all of the altimetry missions provided in Table V are equipped with some other instruments (e.g., GPS) to measure various oceanographic and atmospheric parameters. Moreover, as is clear from this Table, each of these instruments has systematic differences in the adopted radiometer instruments (e.g., band, resolution, and radiometric uncertainty), measurement accuracy, and the observation recording strategies. However, in the third column of Table V, the microwave channel employed in radar altimetry instruments is only provided.

Launched in 1992, TOPEX/Poseidon was an international cooperative mission between NASA and the Centre National d'Etudes Spatiales (CNES). Although SeaSat and GEOSAT mission started 1992, TOPEX/Poseidon can be considered as the first major oceanographic altimeter [72]. This mission had various objectives, some of which are 1) providing continuous measurements of sea-level and ocean topography with an error

lower than 5 cm, 2) monitoring the OSC impact on climate change, 3) producing the initial global OSC seasonal changes, 4) generating precise OT maps, 5) mapping interannual alteration of stored heat in the upper ocean, 6) monitoring ocean attributes, and 7) improving the knowledge of earth's gravity field [73].

The Satellite with Argos and Altika/Ka-band Altimeter (SARAL/Altika) was launched on February 25, 2013 as the first altimeter to carry onboard a Ka-band sensor [73], [74]. SARAL/AltiKa was developed under a joint program between CNES and the ISRO to fill the gap between Envisat and Sentinel-3A (launched in February 2016) [73]. To this end, SARAL flew in the same orbit as ERS-1/2 and Envisat. SARAL/AltiKa was equipped with a solid-state mono-frequency (35.75 GHz, 0.8 cm wavelength) altimeter to provide accurate range measurements (about 1 cm over oceans) [75].

Jason is the second international cooperative mission launched by the National Oceanic and Atmospheric Administration (NOAA) and CNES. Jason satellites have been designed for various applications, including monitoring oceans circulation, learning ocean-atmosphere interactions, enhancing global climate forecasting, and mapping ocean phenomena, such as ocean eddies [76], [77].

Haiyang (HY) is a Chinese series of RS satellites focused on the dynamic marine environment. HY was developed and operated by the CNSA since 2002 [78]. So far, six satellites were launched and two more are planned. HY-2 satellites, including HY-2A (2011), HY-2B (2018), HY 2C (2020), and HY 2D (2021), are the second generations of HY satellites and are equipped with a radar altimeter in Ku- and C-bands. The primary mission of HY-2 is to measure OSW, SSH, and SST.

ERS was the first multidisciplinary satellite program of the ESA, which contains two satellites. ERS-1 was launched in mid-1991 to mainly provide frequent observations of land-surface and ocean-surface processes. The radar altimeter of ERS-1 was a mono-frequency (Ku-band: 13.8 GHz) sensor that provided accurate measurement of the travel time of the microwave pulse from ocean and SI surfaces. The data extracted from ERS-1 have been wiedly employed for accurate ocean topography measurements, OWH, OSW, and SI [79]. ERS-2 was launched in April 1995. Although ERS-2 was very similar to ERS-1, there were several systematic differences. For example, ERS-2 was additionally equipped with the Global Ozone Monitoring Experiment (GOME) sensor to provide observations about atmosphere chemical composition [80]. The ERS-1 and ERS-2 missions ended on March 10, 2000 and September 5, 2011, respectively.

Environmental Satellite (Envisat) was launched in 2002. This satellite became the largest earth-watching satellite for civilian use [81]. The Radar Altimeter 2 (RA-2) was a dual-frequency radar altimeter operating in both Ku- and S-bands, capable of estimating the ionospheric delays errors for elevation refinements [82]. Due to carrying different instruments, Envisat data have been used in broad applications, especially meteorology, hydrology, ocean, and SI studies [83], [84]. After ten years of service, Envisat's mission was ended in 2012.

Cryosat-2 was launched on April 8, 2010, with a nominal lifetime of 3 years (Elapsed: more than 10 years) [85], [86]. Cryosat-2 has the SAR/Interferometric Radar Altimeter

(SIRAL-2), which is a single-frequency Ku-band altimeter [87]. The Cryosat-2 has a repeat cycle of 369 days and a drifting ground track pattern, making different sampling pattern from the previous operating altimeters [88], [89]. Cryosat-2 has a high potential for hydrologic research and climate studies. This is mainly due to a total of 85 modifications that were considered in the design of CryoSat-2, a full backup SIRAL system considered in the SIRAL-2 design, and a special algorithm, which was used to convert data collected by the CryoSat-2 satellite to create more accurate ice maps. Additionally, SIRAL's narrow data acquisition characteristic provides a new opportunity for mesoscale observations as well as lakes and rivers monitoring [88]. It also provides more accurate measurements through multilook observations.

ESA developed Sentinel-3 as a cooperative program with the European Commission initiative Global Monitoring for Environment and Security (GMES) [90]. Its main objectives in ocean-related studies were to extend the time-series measurements of ocean attributes including topography, sea level, OSW speed, sea surface temperature (SST) and ocean color, ice topography, and ocean/sea water properties [91]–[93]. The mission's primary instrument is a dual-frequency synthetic aperture radar altimeter (SRAL). SRAL is a nadir-looking sensor operating in C- and Ku-bands. It provides altimetric data relative to a precise reference frame with an overall accuracy better than 3 cm [94]. The first and second Sentinel-3 satellites (Sentinel-3A and -3B) were launched in 2016 and 2018, respectively. Their orbits are similar to that of ENVISAT, with a height of 814.5 km, an inclination of 98.6, and a 27-day revisit time [90]. Two more altimeter satellites of this series, Sentinel-3C and -3D, are planned to be launched after 2021.

B. Applications

Frequent observations of the ocean topography and its variations make altimeters effective RS systems for monitoring various oceanographic parameters, such as marine geoid, ocean bottom structure, OSCs, OWH, and OSW speed. The most common scientific applications of radar altimetry over the ocean, along with the precision and accuracy requirements are explained in the following sections.

1) Marine Geoid: One of the main applications of altimeters is retrieving marine geoid. The underlying concept is the fact that the spatial alterations in the earth's gravity have a much higher impact on the sea surface topography than the sea level variations due to OTs and OSCs [55]. It means that the ocean topography almost follows the geoid, which can be considered to be constant in time for most applications [95]. If the effects of OT and OSCs in the ocean and atmosphere are eliminated from the DOT, the remaining shape for sea level is called the marine geoid [96]. Therefore, it is possible to monitor and map the sea surface topography with exceptional precision using long-term altimeter datasets [97]. Moreover, it is feasible to produce 3-D data cubes of the marine geoid by coexploring the space-based surface gravity measurements, earth's crust models, and marine depth collected by other data sources [57]. Although marine geoids extracted from spaceborne altimetry data are demanding for

scientific and commercial applications, such as numerical ocean modelling, fisheries, and locating obstructions/constrictions to the major OSCs, it must be noted that these geoids are not accurate enough for navigational hazards validation [58]. According to earlier studies, an accurate geoid estimation of around 7 cm (in terms of the standard deviation) was reasonable using altimetry data. Moreover, combining altimetry and gravity data enhances marine geoid determination by approximately 4–5 cm.

Many studies have so far investigated the applications of altimeters for marine geoid estimation. For instance, Sandwell *et al.* [98] constructed an accurate global marine gravity model using a combination of space-borne radar altimeter measurements and field gravity measurements. After reporting the direct dependency of the accuracy of the altimetry-derived gravity model, they applied the data of CryoSat-2 and Jason-1 with a higher track density instead of predecessor altimeter data. Their results revealed the higher accuracy of their derived marine gravity model than former models. Moreover, Zhang and Sandwell [99] examined the precision of the marine gravity field derived from the AltiKa data. AltiKa altimeter onboard the SARAL spacecraft has a dense track spacing and provides range measurements with twice the height resolution in comparison with all earlier altimeters. After various investigations, they found that AltiKa measurements could considerably increase the accuracy of the global marine gravity field with approximately 1–3 years of observations with track spacing of lower than six kilometers.

2) Ocean Circulation: As mentioned earlier, the changes in ocean water density, temperature, and salinity, along with diverse influential forces, including OSW, the Coriolis Effect, and breaking waves, cause a difference between the SSH and the geoid (e.g., 1 m difference) [55]. The deviations of the sea level from the geoid, known as dynamic topography, can be employed to estimate the ocean circulation [100]. Generally, there are two main types of ocean circulation 1) wind-driven circulation, which is the most dynamic circulation and 2) slow and deep circulation, which is mainly driven by water density [101]. Large-scale ocean circulations, transporting and altering mass, heat, salt, and other ocean constituents, have a major impact on the abyssal properties where wind-driven circulation has no effect. As a fact, the large-scale OSCs flow along the lines of equal topography and are focused around the ocean bottom valleys and hills [102].

Current developments in satellite altimetry, in conjunction with the accurate geoid models, offer a great opportunity to estimate large-scale ocean circulations and lead to a better knowledge of general ocean circulation patterns [103], [104]. Satellite altimetry data collected over the last three decades can be effectively applied to provide detailed information about ocean circulation patterns and variations and their effects on the global water and energy cycles. It must be noted that due to the coarse-scale spatial/temporal resolutions of the altimeter products (e.g., around 100 km and 10 days, respectively), only the largest ocean circulations can be resolved. Obviously, the mentioned resolutions are insufficient to capture the wide range of circulations occurring at the ocean's surface, which span geographical and temporal scales ranging from a few meters

to hours. However, the resolution of the altimeter-derived currents can be developed using several techniques, along-track altimeter measurements, and auxiliary *in situ* measured currents. Moreover, the accuracy of the detailed retrospective picture of ocean circulation patterns retrieved from altimeters is directly influenced by the quality of the geoid modeling [67].

Frajka-Williams [105] attempted to approximate the interannual variations of trans basin ocean transports using the combination of SSH altimetry data and with surface Ekman transport and cable measurements. In this regard, Frajka-Williams [105] employed altimetric data of the Archived, Validating, and Interpretation of Satellite Oceanographic data (AVISO) to map sea level anomalies between 1993 and 2014. The author also used Rapid Climate Change/Meridional Overturning Circulation and Heatflux Array data (RAPID), which delivers the depth-resolved approximations of the heat transports across the North Atlantic. Finally, the author constructed a multitemporal meridional overturning circulation at multiple latitudes between 1993 and 2014. The results confirmed that satellite-based estimation of the meridional overturning circulation recovers over 90% of the interannual variations.

3) Ocean Tide: Ocean level always rises and falls due to several factors, such as the gravitational forces, wind stress, and variations in salinity and temperature [52]–[55]. General patterns of ocean flow are called OSCs [106]. Among all different OSCs, the OT has the most regular rise and fall of the sea surface and the largest signal amplitude in mid-ocean [107]. OT variations in the open ocean typically have standard deviation values between 10 and 60 cm with larger values near coastal regions and marginal seas, exceeding 10 m in some regions [108]. Prior to the development of satellite radar altimeters, hydrodynamical models, determined from ¬*in situ* observations of global monitoring networks of tide and bottom pressure gauges, were employed for global OTs studies. Modeling the global tide pattern, which was initially started from the launch of the TOPEX/Poseidon mission and then continued using other altimeters data, is probably one of the most notable achievement of the satellite altimetry missions [109]–[111]. Thanks to the long time-series altimetry observations with worldwide coverage, it is now possible to increase the accuracy of global OT estimations to nearly 2–3 cm [112]. Due to the OT variations in the open ocean (between 10 cm to the 10 m), almost all of the altimeters can make standardized measurements of the fluctuations of sea level.

Ray and Cartwright [113] integrated climatological hydrographic data and temporally coherent internal tide signals of the altimetric observations to identify the energy fluxes of internal OT in the central North Pacific Ocean. To this end, they used the TOPEX/Poseidon satellite altimeter data to deduct the OT movements, pressures, and currents at the ocean depth, which give power transmission rates. Their results confirmed that satellite altimetry observations allow direct mapping of internal-tide sources, sinks, and power transmission paths throughout the ocean.

4) Fronts or Eddies: The ocean currents that separate sections and create circular currents of water are called fronts or eddies [114]. Theoretically, an ordinary individual front or eddy,

when flattened in time, is seen as a curved dark or a bright current line feature without slicks occurrence [115]. In this way, both sides of the fronts have the same backscatter level [112]. Ocean eddies have a pivotal role in ocean circulations, climate change, heat transport, and biogeochemical cycles [114]. Eddies mapping and monitoring have many scientific and commercial applications in navigation, offshore operations, fisheries, and hurricane and climate forecasting [52]. However, due to the difficulty, high cost, and time-consuming of conducting field measurements, this turbulence was mostly ignored [58], [116]. For this application, altimetry needs a combination of datasets from at least two satellites to provide a proper level of accuracy. The integration between the TOPEX/Poseidon and ERS or Jason and Envisat are good instances in this regard [112].

Zinchenko *et al.* [117] identified and tracked mesoscale eddies in the Lofoten Basin through an automatic workflow using satellite altimetry observations between 1993 and 2017, alongside the locations of their generation and dissipation. The results showed that there were two principal systems of mesoscale eddy formation in the Lofoten Basin: 1) the direct generation of eddies, and 2) the separation of eddies from the Norwegian current during its meandering. They also argued that the mesoscale eddies generated in three separate centers in the Norwegian current frontal zone and then move to the west and north-west, forming three main trajectories.

5) El Nino-Southern Oscillation (ENSO): ENSO is the warming phase of the sea temperature convoyed by high air surface pressure in the tropical western Pacific [118]. On the other hand, La Niño is the cooling phase of the ocean surface, or below-average SST. ENSO event is one of the most important climate phenomena on earth that cause drought, flooding, and hurricanes worldwide. Therefore, SST fluctuations can be employed as warm currents proxies recognized as the energy source of hurricanes [58], [119].

After arguing that the positive or negative interannual global mean sea level (GMSL) anomalies during El Nino or La Nina events are highly correlated, Cazenave *et al.* [120] investigated the respective contributions of three oceans, including the Atlantic, Indian, and Pacific, to the ENSO-related GMSL variations between 1993 and 2010. To this end, Cazenave *et al.* [120] applied delayed time mean sea level anomaly (DT-MSLA) series products provided by the combination of seven satellite altimetry data. To estimate the ocean mass component, the steric contribution of each oceanic region was computed and then removed from the DT-MSLA records. As a result of this article, they comprehensively interpreted the mass changes of the tropical Pacific Ocean and its relation to the GMSL anomaly and the ocean-atmosphere water balance of the oceans.

6) Cryosphere: Cryospheric applications include studying global SI extent, SI thickness, snow cover, SI motion, SI types, OSW pattern, etc. [86]. Of all the above, space-based altimeters have a unique capability in mapping and monitoring SI. Generally, SI is frozen water that originates, expands, and melts in the ocean. SI covers 15% of the world's oceans during the part of the year. Along with certain SI regions that remain year-round, the edge sections expand during winter months and melt during summer months. Therefore, SI, which exists primarily in the

Polar Regions, affects the global climate and ocean level [121]. This is mainly due to SI's role as a huge store of fresh water and its effects in reflecting solar radiation [83]. While the extent and age of SI are retrievable from radar and multiband sensors, altimetry is the only space-based sensor measuring SI thickness and glacier topography [86], [122]. Recent advances in satellite radar altimetry systems create an unprecedented opportunity to monitor the SI sheet mass balance and the SI thickness changes [62], [123], [124].

Altimeters are also employed to measure different SI characteristics, such as SI topography, SI grain size, as well as snow pack properties [112]. For example, CRYOSAT-2 was the first ESA's ice mission designed to monitor the most dynamic sections of Earth's cryosphere (see Section II). Since 1992, the satellites of ERS missions provide a continuous altimetric measurement of the Antarctic SI sheet. Other satellite altimeters, such as Geosat, GFO, and Envisat have been also used for cryospheric applications.

Since Arctic SI has a critical role in global climate, there has been considerable focuses on Arctic Ocean observation using altimetry data in recent years. Peacock and Laxon [125] extracted SSH in SI-covered regions of the Arctic Ocean for the first time. In this article, a mean SSH was constructed by employing ten years of altimetry data collected by ERS-1 and -2. They also estimated the first SSH anomaly map of the Arctic Ocean using altimetric observations. Since then, several studies such as [126]–[129] have attempted to observe the Arctic Ocean SI level and monitor its changes over time.

7) Meteorology: Given the ocean's heat capacity, which is approximately one thousand times larger than the atmosphere's heat capacity, the ocean plays a pivotal role in climate change [130]. The relationship between the ocean and the climate is reciprocal, meaning that the ocean's currents affect the weather condition on different scales, and climate changes alter several properties of oceans [131]. The significant influences of climate change on ocean waters are 1) water temperature rise, 2) coral bleaching, 3) hypoxic zones, 4) coastal erosion and inundation, 5) loss of marine fauna, and 6) changes in precipitation amounts [132]. In this regard, SSH is one of the ocean characteristics that is influenced by climate change. Generally, as global temperature increases, the mean level of the world's oceans rises [133]. However, ocean MSL variations happen over a more extended period in comparison to the atmosphere, wherein storms are formed and dissipated within a day. Therefore, since altimeters are able to continuously measure MSL, they can provide a powerful tool for determining and modeling global climate change [134]. Global sea-level variations and the rise in global MSL can be modeled and monitored with a high-level accuracy due to the availability of altimetry data for over 25 years.

Altimetry can also help to study OWH, OSW velocity, and rogue waves. This is because the characteristics of the reflected radar pulse (i.e., intensity and shape) are influenced by the ocean state, meaning that wind-generated waves and tilted waves on the ocean have a large spectral density in comparison to the calm sea [135]. Therefore, altimetry is a valuable technique to obtain information about OWH and OSW speed statistics,

mean and maximum heights of waves, seasonal and inter-annual variations, trends, and climatology [136]–[139].

Alongside climate change, which significantly affects the MSL, altimetry is also a valuable data source for forecasting models of ocean-atmosphere coupled events including seasonal climate, monsoons, and decadal oscillations, cyclones, hurricanes, and typhoons [112].

Employing 25 years of time-series sea level data retrieved from four various radar altimeters, Nerem *et al.* [134] assessed the climate-change–driven acceleration of the GMSL from 1993 to 2017. Their results identified a rate of about 3 ± 0.4 mm/y for sea level rise, which is accelerating at 0.084 ± 0.025 mm/y2. Using a simple extrapolation, they predicted a sea level rise of 65 ± 12 cm by 2100 relative to 2005. As the evaluation step, Nerem *et al.* [134] used the measurements and models of the intergovernmental panel on climate change (IPCC) fifth assessment report (AR5) projections. The results showed roughly agreement between proposed model predictions and climate model projections.

IV. GRAVIMETER

In recent years, advances in space science technology have significantly increased the awareness of scientists about the Earth's gravitational field, leading to produce various precise geopotential models [140], [141]. For example, launching different gravimetric satellites made it possible to determine the wavelengths of the earth's gravitational field, which was not previously available from satellite observations [142]–[144]. In ocean environments, the time variations of the earth's gravity field, caused by mass redistribution, can be precisely determined using gravimetric satellite observations [145]. The gravimetric satellites can determine the coefficients of the earth's gravity field based on their altitude [146]. For instance, Wolff [147], for the first time, showed that the signals between the satellites moving on the same orbit and with a low distance apart could model the earth's gravity field. The quality of the determined wavelength of the gravity field is dependent on the accurate measurements between the satellites.

In comparison with *in situ* gravimetric observations that are hugely under-sampled in the world's oceans, GRACE has advantages in ocean applications. Indeed, *in situ* gravimetric observations are sparse over the ocean and only concentrate on a few ship routes [148]. Furthermore, maintenance of the instruments that measure long-term gravimetric parameters over oceans is difficult and expensive [149]. However, GRACE observations cover the global oceans with appropriate revisit times. Additionally, although direct and point-to-point height observations from the ocean floor are not feasible using current methods, GRACE satellites provide new insight into progressing climate change due to sea-level change and OSCs [150].

Although gravimetric satellites have many advantages for oceanographic applications, there are also several limitations [151]. For example, regional sea-level change analysis is limited due to the low spatial resolution of gravimetric data [152]. Moreover, spherical harmonic coefficients derived by gravimetric satellites cannot accurately present the gravity field of
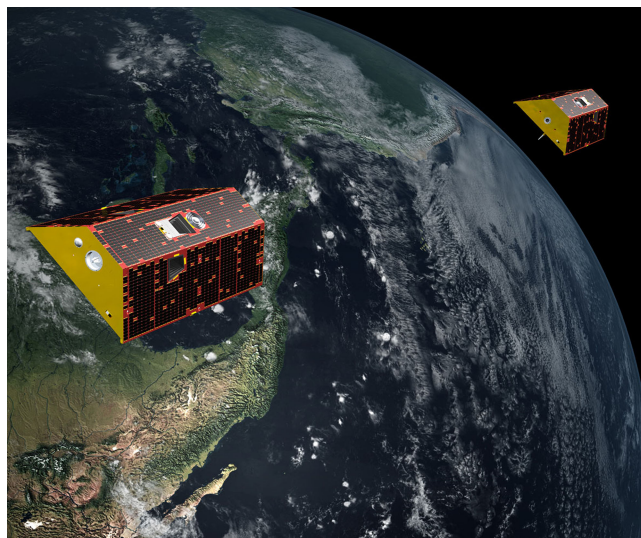

Fig. 3.   GRACE satellites (https://gracefo.jpl.nasa.gov).

TABLE II
CHARACTERISTICS OF GRACE AND GRACE-FO

Satellite	Temporal resolution	Spatial resolution	Period	Mission type
GRACE	Monthly	About 300 km	March 2002-June 2017	gravimetric
GRACE-FO	Monthly	About 300 km	June 2018-present	gravimetric

the earth in coastal areas and, thus, yields sharp boundaries extending beyond the ocean and land area [153]. This can be considered a limitation for gravimetric observations of mass redistributions, called signal leakage between ocean and land. Therefore, an underestimation happens in mass changes on land or ocean [154]. Thus, leakage correction is necessary for the coastal regions to avoid underestimating mass changes [155]. Another limitation of the gravimetric observations is presenting postglacial rebound signals in special places with the highest alterations in the ocean's baroclinic structure, such as the North Atlantic and Southern Oceans. This effect leads to mass load change and errors in GRACE observations [156].

A. Systems

Four gravimetric satellites have been so far launched: Challenging Minisatellite Payload (CHAMP, 2000–2010), Gravity Field and Steady-State Ocean Circulation Explorer (GOCE, 2009–2013), Gravity Recovery and Climate Experiment (GRACE, 2002–2017), and GRACE Follow-On (GRACE-FO, 2018-present). In this article, the GRACE satellites (the last two), the data of which have been widely utilized, will be mainly discussed. Fig. 3 shows a pair of GRACE satellites, and Table II summarizes the characteristics of these satellites.

GRACE, a joint project between the US and Germany, consists of similar twin satellites in a polar orbit (inclination of about 89 degrees, the eccentricity of lower than 0.005, and the period of about 94.5 min). The altitude of this pair of satellites was 500 km at the beginning of the mission and was reduced to
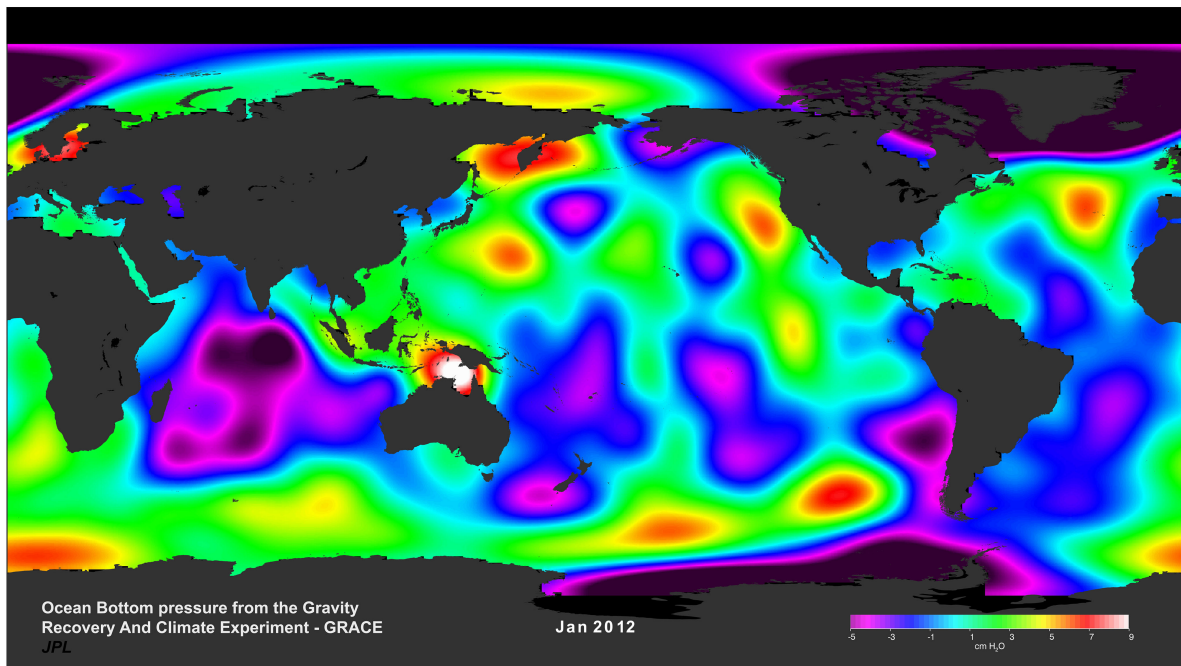
Fig. 4. OBP generated from the GRACE data (https://svs.gsfc.nasa.gov/30503).

300 km at the ending of its mission. The distance between these satellites was about 220 km; however, by changing the gravity at the point where the satellites pass, the distance between the two satellites was changed. Therefore, this distance and its variations were measured accurately [157].

Three JPL, GFZ, and UTCSR centers are responsible for processing, analyzing, and releasing the data, respectively. In recent years, other centers release other versions of the GRACE data. Generally, there are four categories of GRACE data, including Level-0, Level-1A, Level-1B, and Level-2 [158]. The process is started with Level-0, which is raw data received from the satellite including K-Bands data, GPS data, accelerometers data, and star camera data. After implementing corrections on Level-0, binary data are transformed into engineering and meaningful units after about two months, forming the Level-1A data. In Level-1B, the data is evenly timed, and observations are reduced. Final GRACE data are divided into two sections on Level-2: 1) spherical harmonic coefficients of the mean gravity field of the earth for several months or years (static part of the gravity field), and 2) monthly spherical harmonic coefficients (dynamic part of the gravity field). The Level-2 data are available for both lands and oceans. The latest version of Level-2 data is RL06, available from about two years ago [159], [160]. Moreover, in recent years, another form of the gravity field by GRACE has been released, which is spatially monthly gridded mass data, named Mass concentration blocks (Mascons) [161]. In these Mascons, postprocessing filtering is more rigorous rather than coefficients by implementing geophysical constraints [162].

After termination of the GRACE mission in 2017, GRACE Follow-On (GRACE-FO, Table II) continued its predecessor mission in May 2018 [163]. The design and orbit properties of these satellites are similar to those of GRACE (eccentricity of 0.00179, the inclination of 89o, the period of 94.5 min, and an altitude of about 500 km). This satellite was designed to provide continuous measurements of the time-variable Earth's gravity field [164].

B. Applications

Gravimetric satellites gave applications in different domains, including oceanography, hydrology, glaciology, and geology [165]–[170]. Wahr *et al.* [165], for the first time, showed different applications of time-variable gravity field derived by GRACE in different sciences, including hydrology, oceanography, and atmosphere. In the following sections, the main oceanographic applications of gravimetric satellites are discussed.

1) Ocean Bottom Pressure: The column water mass on the combined ocean and atmosphere is called the ocean bottom pressure (OBP) [171]. OBP variability is due to three important factors [172]: 1) variations in wind stress, curl, and circulation (this is called internal ocean mass redistribution), 2) water mass entering and leaving the ocean (this is considered as part of the global water cycle), and 3) atmospheric mass exchange between the ocean and land. Although direct measurement of OBP is difficult, GRACE can effectively measure global OBP (see Fig. 4 for an example). Furthermore, Chambers *et al.* [173] determined seasonal global ocean mass change derived by GRACE and compared it with the mass change obtained from altimetry, which was corrected from the steric component between 2002 and 2004. GRACE and steric-corrected altimetry results were similar in terms of the annual amplitude of global ocean mass variations (8.4 mm and 8.5 mm, respectively).

2) Deep Ocean Current: Tracking OBP changes are beneficial in understanding variability in deep ocean currents and

ocean circulations [148], [174]. Vertically integrating the gradient of OBP in a profile from south to north reflects fluctuations of bottom currents, which is the key point for transport variability [175]. Zlotnicki *et al.* [176] also studied Southern ocean current change by GRACE for a period of 3 years (2003–2005) and compared their results with estimates from the data-assimilative model calculations. They obtained a transport variability by a drop from ± 4 cm$_{H20}$ to ± 5 cm$_{H20}$, which was in agreement with the oceanic model.

3) Sea Level: Global OBP variations can be expressed in terms of the equivalent barotropic global SSH change [177]. The sea-level change is due to both steric and bars static (nonsteric) components [152]. The steric component is the volumetric variations, including temperature and extent salinity changes. The barystatic component is known as the OBP component. Therefore, GRACE measures global sea-level changes associated with ocean mass change [178].

The combination of GRACE with satellite altimetry observations provides steric sea-level changes and ocean surface topography (dynamic ocean topography) [179]. Satellite altimetry provides information on the total of both steric and barystatic components. Therefore, differences between GRACE and altimetry give the steric sea level variability [180]. GRACE and altimetry can be comparable when the steric component adds back to GRACE observations [181].

There are different oceanic models and observations (e.g., world ocean atlas or Argo observations), which provide the information of different oceanic parameters, such as temperature and salinity up to a high depth of the oceans (about 5500 m) [182]. By combining this model and GRACE observations, measuring total global sea-level change is possible. This was a revolution in oceanographic science.

Combining GRACE and Jason-1 altimetry observations, Lombard *et al.* [183] computed seasonal steric sea-level change and compared it with the results obtained from the world ocean atlas for four consecutive years (mid-2002 and mid-2006). The sea-level change of about -12 mm to 12 mm with a positive trend of 1.2 mm/year was observed. The comparison between ocean mass changes derived by GRACE and the oceanic model showed a mean root mean square error (RMSE) of 2–3 cm of sea level. Moreover, the lowest and biggest RMSE values were observed in the Southern Hemisphere and the western tropical Pacific, respectively. Additionally, Feng and Zhong [184] computed total global sea-level changes between 2005 and 2014 by combining GRACE and Argo float data. They obtained an annual amplitude of 5.6 mm and a 2.8 mm/year trend, which was fairly in agreement with altimetry results (trend of 3.1 mm/year), particularly in the Southern Hemisphere Ocean. They also observed a drop of 1 cm in the global mean sea level from 2010 to 2011. The authors argued that this was due to the strong La Niña event in that period. Recently, Amin *et al.* [185] calculated global barystatic sea-level change by GRACE data between 2005 and 2016, and compared the results with the altimetry and Argo observations. They showed almost a similar trend of nonsteric sea-level change for both RL05 and RL06 versions of GRACE data (2.19 mm/year and 2.25 mm/year, respectively). The altimetry results showed a trend of 3.9 mm/year for GMSL rise, in which the proportions of steric and non-steric components were 35% and 65% (1.29 mm/year and 2 mm/year, respectively), respectively. The results also showed the similarity of GRACE and barystatic component of altimetry.

4) Ocean Heat: Another combination of GRACE and altimetry can result in the estimation of time-variable ocean heat capacity. This combination is performed by the thermal expansion of seawater [186]. In this expansion, the ocean's surface height derived by altimetry and OBP derived from GRACE is combined to estimate the ocean's heat storage. Scientists can predict hurricane strength and climate change by knowing the changes in ocean heat storage obtained from GRACE observations. Jayne *et al.* [186] used thermal expansion to present ocean heat storage by the combination of OBP of GRACE and steric SSH altimetric observations. They compared their results with a circulation model and found a large ocean heat variation in Equatorial Pacific, the North Atlantic, and the North Pacific. The comparison of observations and model showed an error of $280 \times 10^6 j/m^2$ in ocean heat content. However, consistency in the high latitudes with large barotropic motions and high-frequency barotropic variability was observed.

V. Synthetic Aperture Radar

There are currently different SAR systems with various channels (e.g., X-, C-, and L-band), making them useful for a variety of oceanographic applications. Among the operational microwave radar systems, SAR has gained more attention for oceanographic applications due to several advantages, especially higher spatial resolutions.

SAR is an active imaging system that sends microwave pulses towards the ocean surface using a transmitter. The signal is scattered back and is received by a microwave receiver. Finally, the returned signal is formed as a radar image. The image may be formed through either monostatic or bistatic SAR mechanisms, which are defined as different structures to receive and transmit microwave signals [2].

SAR images have two spatial resolutions: 1) along-track or azimuth resolution, which is in the direction parallel to the system motion, and 2) across-track or range resolution, which is orthogonal to its direction [187]. In contrast to passive microwave systems that provide low spatial resolution data over the ocean, SAR active systems acquire higher spatial resolution images (e.g., Sentinel-1 with 10 m resolution).

Another feature of the SAR imaging system is polarization, which means how the signals propagate and scatter back to the platform [188]. Mathematically, it is defined as the locus of the electric field vector in the perpendicular plane to the propagation path. Generally, polarization can be linear or circular. The circular polarization, such as compact polarimetry, is according to transmitting signals through a combination of equally-weighted vertical and horizontal polarizations [189]. The combination is included at $45°$ or shifted in phase by $90°$ to a circular polarization [189]. On the other hand, linear polarization is more common and includes four types of receiving and transmitting signals: HH for horizontal reception and horizontal transmission, VV, HV, and HV, which can be defined

based on the same terminology of the HH polarization [190]. Therefore, SAR systems can collect data at one, two, or four linear polarization combinations: polarized (HH or VV or vice versa), dual-polarized [(HH, HV), (VV, VH), or (HH, VV)], and fully polarimetric (HH, VV, HV, and VH) [191].

A. Systems

Table VI provides the specifications of various SAR systems that have been frequently used for oceanographic applications. The specifications of some of these systems are discussed below.

Sentinel-1 is the European SAR system and is the first novel space member of the GMES satellite family [192]. Currently, the Sentinel-1 mission includes two satellites, Sentinel-1A and -1B, with identical orbits. The mission delivers constant SAR mapping of the earth with improved temporal resolution and coverage, timeliness, and reliability for current operational services and oceanographic applications [192].

RADARSAT-1 is the Canadian satellite that scans the earth's natural resources and the environment. This mission was part of a collaborative project between the Canadian government, a private third party, and NASA [193]. The SAR data acquired by this satellite has been used in different applications, including oceanography, coastal monitoring, SI studies, hydrology, cartography, agriculture, forestry, and disaster management.

RADARSAT-2 is a cooperative satellite mission of Mac-Donald Dettwiler Associates Limited (MDA), Canadian Space Agency (CSA), and Public and Private Partnerships in a profitable scheme. The main objectives of this mission are monitoring the environment, managing natural resources, and observing the ocean and coastal areas [194].

Advanced Land Observation Satellite-2 (ALOS-2) was the second generation of the ALOS satellite launched by the Japan Aerospace Exploration Agency (JAXA). This satellite captures L-band SAR data, and its primary objective is to offer data to monitor ocean, land, forest, and disasters [195]. It also includes a secondary objective to continue the ALOS (nicknamed Daichi) data use.

The constellation of Small Satellites for Mediterranean basin Observation (COSMO-SkyMed) is a constellation of four platforms, developed by the Agenzia Spaziale Italiana (ASI), and funded and managed by the Italian Ministry of Research (MUR) and the Italian Ministry of Defense (MoD). All four SAR systems can operate in real-time and provide high-resolution SAR data. The primary objectives of the mission are to globally observe the Earth and provide the required data for military and civil communities. For example, civil communities use SAR data to study disasters, coastal environments, and forest ecosystems. Moreover, the four X-band SAR platforms provide data for the meteorological community, particularly monitoring of SI and OWH patterns [196], [197].

B. Applications

SAR has many valuable applications over the oceans, such as OSW speed/direction estimation, OWH mapping, OSC estimation, SI mapping and monitoring, ocean oil spill (OOS) detection, ship detection, and ocean floor mapping. In this section, eight important applications of SAR systems over the oceans are explained.

1) Ocean Surface Wind: OSW creates waves and is a significant source of power for local and global ocean movements. An accurate estimation of OSW supports investigating marine environments and climate change [198]. Deriving OSW from SAR data has been the focus of many studies [199]. SAR-based OSW data perform better than the data derived from traditional OSW measuring techniques, particularly in coastal areas [200]. Moreover, OSW direction and speed can be specified at the same time using SAR data [201]. In [202], the efficacy of Geophysical Model Functions (GMFs) in retrieving OSW through the VV-polarized Sentinel-1A SAR data over the Caspian sea was studied [202]. Additionally, an HH-polarized GMF based on RADARSAT-2 and Sentinel-1A modes for OSW retrieval was developed by Lu *et al.* [203]. In this article, the input data were exploited to evaluate the GFM efficiency. It was also observed that the GFM-based OSW was consistent with buoy measurements [203].

2) Ocean Wave Height: Ocean surface waves are regularly created due to turbulence and wind in the atmospheric layer [204]. Ocean waves can also result from geologic impacts, such as vulcanicity and earthquakes, which may travel a long distance before hitting a land [205]. Their size varies from ripples or capillary to devastative tsunamis [206]. Therefore, the knowledge of ocean wave properties, including height, length, and propagation direction, improves the understanding of the atmosphere layer affecting the ocean surface [206].

A unique imaging mode of SAR, which is called the wave mode (WM), has been developed for ocean wave studies [207]. The nearly 30 years of WM data over global oceans have been captured through the ESA's SAR platforms, including ERS-2, ENVISAT, Sentinel-1A/1B, and the Chinese GaoFen-3 SAR [207]. In this regard, a novel nonlinear transformation algorithm has been developed by [208] to map a 2-D ocean wave spectrum from the C-band polarized RADARSAT-2 SAR images. The result has been validated with *in situ* measurements (e.g., from buoy) and the European Centre for Medium-Range Weather Forecasts (ECMWF) ocean wave model [208]. Moreover, Liu *et al.* [209] retrieved the 2-D ocean wave spectrum using SAR data. They derived the spectrum using an iterative algorithm from Envisat Advanced Synthetic Aperture Radar (ASAR) WM single look complex (SLC) data [209].

Solitary waves are specific kinds of internal waves [210]. They are a category of nonlinear, nonsinusoidal, and isolated waves that happen regularly within the ocean water environments [211]. Their velocity field produces a convergence region, coarsening the ocean surface by raising surface waves [212]. Additionally, they may be considered as density fluctuations propagating sideways the ocean stratification, and they are currently recognized as the influencer of a series of ocean phenomena [213]. Solitary waves are greatly significant in counting and also recognizing ocean mixing and energetics [214]. Moreover, it has been argued that organic carbon fluxes are connected with large internal waves [215]. To study internal waves, SAR systems provide valuable datasets. Therefore, in

[216], the application of full-polarimetric ALOS PALSAR images was investigated to identify ocean Internal Solitary Waves (ISWs) [216]. This article was developed to construct compact polarimetry SAR images and to derive different CP features. The ISWs-sea surface variation for the various polarization features has also been investigated in this article. The results showed the improvement of the k-means clustering algorithm based on CP features to detect ISWs [216]. Moreover, Ning *et al.* [217] evaluated the spatial scattering properties of internal solitary waves using Sentinel-1 and GF-3 SAR images. It was observed that the velocity and the amplitude of ISWs were associated with the underwater topography [217].

3) Ocean Surface Current: OSC is a vital element in balancing the overall climate and contributes to moving salt, heat, and mass on the ocean [218]. Among different radar platforms, the Interferometric SAR (InSAR) technique allows researchers to study OSCs [219]. For example, in a comprehensive research work, Kozlov and Plotnikov [220] applied Sentinel-1 data to measure horizontal OSC velocity and eddies signatures in the Fram Strait marginal SI zone between Spitsbergen and Greenland [220]. Moreover, Liu *et al.* [221] proposed a method called intrapulse beam switching (IPBS) based on a phased array antenna. It integrated the Doppler Centroid Anomaly (DCA) method to quantity fully OSC vectors [213]. Finally, Seenipandi *et al.* [222] computed the wave energy and littoral OSC velocity through the OWH of level-4 radar data [214]. They used a combination of the Sentinel-3A/3B, Jason-3, Saral (AltiKa), CFOSAT, and Cryosat-2 datasets to calculate the OWH feature [222].

4) Sea Ice: SI cover is important for the Arctic environment and plays a pivotal role in the world's climate systems. Moreover, it has significant effects on maritime activities and navigation in the glacial areas [223]. Therefore, monitoring the SI through classification and charting grabbed decision-makers' attention to guarantee safety and economic activities without any possible damage to the environment. For example, the SI charting is according to precisely locating the edge between open water and SI [224]. SI navigation in the Arctic depends on the SI properties, particularly thickness [225]. Currently, SI charting is based on a variety of datasets. Recently, many studies have been contributed to acquiring data for deriving SI parameters from SAR systems. For instance, in [226], a technique was proposed to distinguish open water from SI through fully polarization RADARSAT-2 SAR imagery. This method was developed according to the ocean surface roughness properties and the polarization ratio from the SAR data [226]. In another effort, Blix *et al.* [227] developed a novel technique to combine the Gaussian process regression (GPR) and neural network (NN) using quad-polarization Radarsat-2 and dual-pol Sentinel-1 data for estimating different physical SI parameters [227].

5) Ocean Oil Spill: The number of marine vessels has significantly increased over time [228]. Consequently, the number of oil releases in the ocean has considerably increased, imposing danger to marine life [228]–[231]. Thus, early OOS detection is essential to assess the possible oil release from various sources to the ocean. In this regard, first responders can consider the OOS

map to perform early effective measures to reduce the danger to the marine ecosystem. For example, prohibited oil releases killed many seabirds in several oceans [232]–[235]. SAR data have been widely applied for OOS mapping and monitoring For instance, the article conducted by Marzialetti and Laneve [236] confirmed that X-band radar outperformed L- and C-band radar to recognize OOSs [236]. In another study, Zeng and Wang [237] proposed a deep oil spill convolutional network (OSCNet) through multisource SAR datasets over the Bohai Bay of China. The experiments showed that OSCNet classification performance significantly outperformed traditional Machine Learning (ML) algorithms [237].

6) Ship Detection: Nowadays, maritime surveillance has grabbed considerable attention [238]. In this regard, ship velocity and heading assessment are important to monitor vessel traffic [239]. Therefore, high-resolution SAR data have been widely applied for ship detection. A ship can be identified through three SAR methods, including intense radar signal return back from the ship, wake forms, and OOS associated with ships [240]. For example, Karakus and Achim [241] detected ship wake using a Radon transform-based inverse model with a sparse nonconvex generalized minimax concave (GMC) regularization. The proposed method was established using TerraSAR-X data collected for five ships with their visible ship wakes [241]. Moreover, a wake detection approach was introduced by Graziano *et al.* [242] using TerraSAR-X Stripmap and COSMO/SkyMed SAR images over the Gulf of Naples. After the wake detection, the ship heading was assessed according to the turbulent wake direction and ship velocity [242].

7) Bathymetry: Knowledge of seafloor topography is important for several areas of applications, such as marine biology, marine physical oceanography, and geophysics [243]. Ocean bottom topography changes the ocean dynamics by steering water flows and makes barriers to avoid deep waters from mixing [244]. In this regard, the SAR system can observe the water surface roughness and, thus, can recognize topographic features of the ocean floor. The roughness is made through variations in the current flowing upon underwater topographies. This method only works when the OSCs are as much strength as to discern, and also when there are tiny wind waves on the ocean surface [245].

There are three steps to study the bottom topography using SAR imaging systems: 1) finding the connection between the OSC and underwater topographic features; 2) accurate hydrodynamic modulation of the ocean surface variations through the OSC; and 3) creating a relationship between the microwave signal and the sea surface [246]. In [247], the gridded bathymetry information was automatically derived from SAR data. They used sea state alterations in TerraSAR-X images to extract the bathymetry in shelf areas through the shoaling effect. In similar research work, four Sentinel-1A SAR images were employed to identify depths of shallow water using swell patterns. It tried to measure the bathymetry results sensitivity through initial water depth, wavelength, and swell period. The experiments showed that there was a high sensitivity between water depth and the swell period, and finally, they assessed the results derived from several multisource SAR data [248].

VI. Lidar

LiDAR systems, with the ability to transmit a laser pulse and measure the backscattered energy, can retrieve the particulate backscattering coefficient in ocean subsurface layers [249]. The pulse interacting with marine particles either scatters the transmitted photons or generates photons with different frequencies [250]. Theoretically, after emitting a short laser pulse of light, with a certain duration (e.g., 12 ns), the pulse interacts with atmosphere layers, ocean surface, and layers of the water column, respectively. At each time interval, related to the laser sampling rate, the backscattered energy (from water molecules, phytoplankton, particulate matter, and schools of fish) is sensed by the receiver at the specified wavelength. This backscattered energy is utilized to extract information from ocean layers [250].

Two quantities of attenuation and backscattering coefficient are usually required to be calculated using inversion techniques to utilize LiDAR technology for ocean studies [251]. Jamet *et al.* [250] presented the basics of these inversion methods. Other variables, such as depolarization ratio [252] and [253], absorption coefficient [253], and ocean color [254], are other products that can be estimated from LiDAR measurements.

LiDAR instruments are among the airborne/spaceborne active RS systems that can obtain depth-resolved information of ocean layers [255]. Satellite LiDAR systems can operate under thin clouds, between holes in broken clouds, and in polar regions to provide global ocean coverage [252]. The corresponding LiDAR pulses can also penetrate tens of meters of water during day or night [256]. In contrast to shipborne LiDAR instruments, spaceborne or airborne LiDAR measurements are also faster in data acquisition, cover more area, and have no disturbance for plankton layers when detected [257]. Moreover, if the ocean and atmospheric LiDAR instruments are combined (such as the CALIOP), the potential to provide information about the ocean-atmosphere is exchanged and interactions for climate studies is increased [258].

Compared to passive RS systems, the performance of LiDAR systems are lower in rapidly monitoring changing properties of the ocean [259]. For example, the 22.5 m vertical binning resolution of CALIOP is not enough for ocean layers study, and the instrument itself is not able to separate backscatter and attenuation coefficients and, thus, requires calibrations and further processing [260]. Moreover, in the case of bathymetric studies using airborne LiDAR systems (or specific case of ICESat-2 satellite measurements), floating algae, fish swarms, seabed vegetation, and water turbidity can decrease the accuracy of measured point clouds [261]. However, LiDAR bathymetry is more cost- and time-efficient than traditional shipborne surveying methods.

A. Systems

Subsurface ocean measurements have been traditionally conducted using shipborne or airborne instruments [258], [262]–[264]. A specifically designed satellite for oceanographic missions and water column profile data detection has not been launched into space yet, and currently, shipborne and airborne

LiDAR systems are employed for ocean studies [255]. Table VII summarizes the specifications of spaceborne LiDA missions.

The Cloud-Aerosol LiDAR with Orthogonal Polarization (CALIOP) system, which was designed for atmospheric studies onboard the Cloud-Aerosol LiDAR and Infrared Pathfinder Satellite Observations (CALIPSO) platform to measure global ocean carbon stocks, was among the first spaceborne LiDAR systems. CALIOP was a proof-of-concept for spaceborne oceanographic LiDAR. Its mission's lifetime was extended for three more years (2018–2020) to use its capabilities in studying ocean subsurface layers [252]. Hostetler *et al.* [265] described the abilities and gaps in benefiting from this spaceborne LiDAR system. Dionisi *et al.* [252] was the first work that evaluated the applicability of CALIOP data for mid-latitude ocean studies using the depolarization ratio parameter. Moreover, Vonk [266] approximated the theoretical backscattering of CLIOP data from the ocean surface by establishing an empirical relationship between OSW speed and ocean surface backscatter.

Field evaluation of CALIOP measurements has never been performed due to the scarcity of *in situ* data. Lacour *et al.* [249] used ARGO float measurements to evaluate CALIOP observations in North Atlantic. Moreover, Chen *et al.* [267] deployed scattering values of bio-optical models for oceans to calibrate the oceanic LiDAR signals. They also proposed the optimal wavelengths for coastal water and open ocean studies. Inversely, Churnside and Marchbanks [268] used satellite measurements of optical backscattering coefficient for airborne LiDAR calibration. They compared multiple regression models for this calibration task.

ICESat-2, which is another spaceborne LiDAR system, is not designed for oceanographic purposes. Although ICESat-2 is mainly designed to study polar ice, clouds, and land elevation, it has the power to penetrate clean ocean waters in coastal regions for up to a few tens of meters. Thus, it can be used for bathymetric applications as auxiliary data.

B. Applications

LiDAR applications in oceanographic studies cover a wide range of disciplines. Measuring optical properties of water, estimating backscatter coefficient, detecting bubbles, internal waves, planktons, and schools of fish are other applications that have been studied by all types of LiDAR instruments [251], [255], [257], [269]. However, Bathymetric and 3-D mapping applications are mainly limited to airborne LiDAR instruments [261], [270], [271]. Recently, the ICESat-2 spaceborne LiDAR has also attracted attention in such applications [272].

Other LiDAR applications are related to 3-D mapping of the seabed and coastal/river regions, such as bathymetry, coral reef mapping, tidal creek extraction, and underwater archaeology. These applications are usually restricted to airborne LiDAR surveys or underwater mapping techniques, which utilize LiDAR instruments to study geomorphological changes [270].

LiDAR has also been utilized to study ocean subsurface parameters (other than bathymetry). These studies are often limited to the latest publications in this field and have focused

on using spaceborne LiDAR measurements, but some studies using ship-/air-borne instruments are also included.

1) Bathymetry: Generally, bathymetry refers to determining the depth of water bodies, including rivers, lakes, coastal regions, ocean, and sea. Accurate bathymetric maps are essential for seabed topography determination, underwater ecosystem studies, offshore industries, shipping, sediment process analysis, and cable routing [33], [271]. Deep bathymetric measurements are usually performed by SONAR systems [34]. On the other hand, LiDAR-based bathymetric mapping is usually used for mapping shallow water regions with up to ∼50 m depth. While airborne LiDAR systems are often used for marine and coastal water bathymetry, spaceborne methods relying on either satellite LiDAR systems or image-based techniques are attracting more attention [34], [261], [270].

Yang *et al.* [261] evaluated the performance of a bidirectional cloth simulation filtering method for airborne bathymetric mapping. Ma *et al.* [272] also combined Sentinel-2 and ICESat-2 data based on an empirical model to produce bathymetric maps. ICESat-2 data were also used as *in situ* measurements for training the models. Moreover, Launeau *et al.* [270] utilized full-waveform LiDAR in 532 nm and 1064 nm wavelengths for bathymetry and surface water height determination. To explore the influence of typical wave patterns on sensor configurations, Westfeld *et al.* [271] simulated the bathymetry process and analyzed the accuracy of 3-D coordinates of the bottom of the water.

2) Aquatic Vegetation: Aquatic vegetation and coral reefs are valuable marine ecosystems that can protect coastlines from erosion, are a habitat for marine life, and are important for the underwater environment [273]. Airborne LiDAR systems provide valuable data for mapping the spatial extent and changes of these vegetation environments through time and enable detection and physical measurement of individual coral reef colonies, which is important for coastal management [274]. As an example, Su *et al.* [273] detected coral reefs by combining airborne bathymetric variables, such as slope, curvature, and bottom waveform attributes, such as peak amplitude, pulse width, skewness, kurtosis, and backscatter cross section. Moreover, Amani *et al.* [275] used bathymetric LiDAR data to map different aquatic vegetation in Newfoundland, Canada's offshore are. To this end, they have used a combination of unsupervised classification algorithm and object-based image analysis. The results showed the reasonable accuracy of LiDAR data for aquatic vegetation mapping. They also suggested using high quality LiDAR data and very high resolution optical satellite images could improve the accuracy.

3) Ocean Tide: Tidal flats are regions in coastal areas where are affected by OT, and sediments are deposited there. They are essential for human recreational activities, coastal natural environment, and marine habitat. Furthermore, through time, tidal creeks evolve tidal flats, making them an important subject for studies. Determining their geometric information is essential for such studies [276]. One of the applications of airborne LiDAR systems is in observing and measuring tidal flats and their geometric features in order to better understand tidal creek behaviors.

Branch *et al.* [276] used LiDAR measurements to examine temporal and spatial variations of SSH at the mouth of the Colombia River. Since tidal creeks affect the life of coastal living people, Kim *et al.* [277] tried to derive a suitable method for their extraction using LiDAR data. They showed that cloth simulation filtering could better extract various tidal creeks.

VII. SONAR

Considering the limited applications of electromagnetic-based imaging systems (e.g., optical and LiDAR) in the underwater environment, the SONAR system has been the preferred solution to study bathymetry, morphology, and structure of ocean floor [278]–[282]. SONAR systems are mainly designed to detect and/or transmit the acoustic propagation between a target and a receiver for underwater applications. The main reasons for using SONAR systems for underwater applications are as follows.

1) The speed of sound through water is almost fixed for a given temperature, salinity, and depth [283], [284].
2) Speed and travel distance of acoustic propagation through water are considerably greater than those through the air [285].
3) The acoustic propagation is fairly unconstrained by the water properties.

In the past, utilizing SONAR systems for ocean applications was expensive and was limited by logistical and technical issues such as accessibility, ship and equipment availability, changing weather conditions, and underwater flow conditions [286]. However, recent advances in the fields of underwater and robotics technologies have resulted in the development of various underwater vehicles, which are compatible with high-resolution SONAR systems and capable of swimming close to the seabed. These technologies have allowed cost-efficient and rapid access to the ocean environment and have facilitated SONAR applications [281], [286], [287].

A. Systems

Generally, there are two types of SONAR systems: passive and active. Passive SONAR systems collect the echoes generated by different objects in the ocean (e.g., vessels and mammals) using one or an array of hydrophones (i.e., underwater microphone). These systems are basically acoustic receivers that detect signals from background noise produced from the ambient noise of the sea or the SONAR platform itself [288]. In fact, passive SONAR systems use the frequency and variation of the received echoes over time to detect a target. On the other hand, active SONAR systems emit the acoustic wave using a transmitter and, then, measures the echoes bounced back from objects in oceans [278], [285]. This article only considers the active SONAR systems because they have been the mostly systems used in oceans [278], [282], [289]–[292].

The active SONAR systems can be divided into four main categories of single-beam, side-scan, multibeam, and synthetic aperture SONAR. The selection of the optimal SONAR system for an ocean application depends on various factors, such as

spatial resolution, the required time for the survey, and cost. A brief description of each system is provided in the following sections.

Single-beam SONAR systems (also known as echo-sounders) employ a narrow acoustic beam at a relatively low frequency, mostly emitted from a near-surface vessel. Single-beam systems use a specific sound speed through the water column to determine the along-track water depth. Most of the available bathymetry data have been so far collected with the aid of different types of single-beam SONAR systems [285]. Although single-beam SONAR systems provide acceptable spatial resolution for underwater applications, their coverage is limited [278].

Side-scan SONAR systems have almost similar concepts with the single-beam sensor, except for the viewing geometry that is changed to horizontal from vertical viewing geometry. Moreover, side-scan SONAR systems use two parallel transducers to transfer a wide-angle pulse of sound frequencies to map relatively large areas compared to the single-beam SONAR systems. A typical side-scan SONAR system consists of a projector for emitting signals, a hydrophone for receiving signals usually within a towfish, a tow cable, and an electric recording device [293]. These systems provide 2-D (azimuth and range) images from underwater. The collected images are more difficult to interpret than the downward-oriented systems since they require a sophisticated knowledge of sensor geometry. Although side-scan SONARs, as 2-D imaging systems, acquire visual images with both high spatial resolution and broad coverage, they cannot directly generate the 3-D information from the underwater environment [294].

The development of side-scan SONAR systems and the availability of advanced digital image processing methods have led to producing multibeam SONAR systems [285]. Multibeam SONARs, as vertically downward-oriented sensors, employ several single transmitted and received beams over an extensive range of transmitted angles. The main advantage of multibeam SONAR systems over single-beam SONARs is producing approximately a full coverage of the ocean floor within the sensor field of view. Nowadays, the multibeam SONAR systems are also of more interest for underwater applications due to their improved data consistency compared to the conventional SONAR systems (e.g., single-beam) as well as their ability to provide accurate and aerial-like images [285], [295], [296].

Synthetic aperture SONAR systems combine successive acoustic impulses as they move along a defined survey line to provide an improved azimuth resolution compared to the side scan SONAR systems. Since the prerequisite for accurate processing of the synthetic aperture SONAR data is precise information about the movement and position of the SONAR instrument [297], [298], the synthetic array is formed by the impulses that have the image position within the beam-width. Although complex data are collected by the synthetic aperture SONAR systems, the main processing step is usually reducing the original complex image into a pure intensity image [299]. Synthetic aperture SONAR systems are capable of capturing SONAR images with the resolution of several centimeters over a range of up to several hundred meters [278]. This makes synthetic aperture SONAR systems efficient tools for various

underwater applications, such as small object search, wreckage imaging, pipeline inspection, and underwater archaeology.

The pre-processing and postprocessing of SONAR data, especially those collected by synthetic aperture SONAR systems, is sometimes a rigorous procedure and depends on different site-specific factors, including seabed properties and textures [287]. In fact, all processing algorithms for the interpretation of SONAR data should be accurately applied to obtain reasonable results [278].

B. Applications

Nowadays, the preferred method of collecting information from the underwater ocean environment is by sound waves [278], [282]. Therefore, SONAR systems have been successfully used in different ocean applications, such as characterization of the ocean floor [280], [291], monitoring seafloor hydrothermal flow [289], geomorphological characterization of the ocean floor [295], [300], seagrass detection and monitoring [301], benthic habitats mapping [292], and target detection [278]. The following three subsections are provided to discuss three of the most versatile applications of the SONAR data, along with several case studies.

1) Bathymetry: Bathymetry mapping of oceans plays a significant role in various disciplines such as oceanography and sustainable ocean management [279], [302]. Accordingly, mapping and monitoring of the ocean floor have long been of interest in different studies [270]. In recent decades, the utilization of SONAR data has become a common practice for ocean bathymetry [279], [280]. For example, Arndt *et al.* [303] provided a new digital bathymetric map with 500×500 spatial resolution for the seafloor of the circum-Antarctic by compiling single-beam and multi-beam SONAR datasets and multiple supplementary data (e.g., digitized and predicated bathymetry data and regional bathymetric compilations). Since this study used different bathymetric datasets with different characteristics, several processing steps were applied to ensure the consistency of the final bathymetry map. An *et al.* [290] presented a novel 3-D inversion approach for bathymetry mapping in northwest Greenland using airborne gravity data combined with multibeam SONAR data. The cost-efficiency of the proposed methodology was demonstrated by a thorough accuracy assessment procedure in two study sites.

2) Aquatic Vegetation: Aquatic vegetation, as a critical component of the ocean ecosystems, provides habitat for many aquatic organisms, indicates the water quality, stabilizes the seafloor, and regulates water cycle and water flow [304], [305]. Accordingly, to detect and monitor potential ecosystem changes in ocean environments, it is of paramount importance to spatially characterize the abundance, distribution, and diversity of aquatic vegetation [306]. With the technological progress of the SONAR systems in recent decades, SONAR data were successfully employed for aquatic vegetation mapping in different studies [307]. For instance, Sabol *et al.* [308] comprehensively evaluated single-beam SONAR data for mapping three seagrass species (i.e., T. testudinum, H. wrightii, and S. filiforme). The comparison of the resulted outputs with in-situ data showed

promising performance of the proposed method using SONAR data. The authors also found that different factors, such as depth, OSW, and photosynthetic activity, substantially influenced the performance of the proposed method. Barrell *et al.* [309] evaluated the complementarity of single-beam SONAR data and QuickBird satellite image for seagrass mapping in two different study sites with shallow water depth (<10 m). The results showed that although the agreement between satellite image and SONAR data was limited, the integration of SONAR data with satellite image substantially improved the accuracy of seagrass mapping in comparison to either dataset alone. The authors also discussed the impact of site-specific factors (e.g., patchiness of seagrass) on under- or overestimation of seagrass abundance by single-beam SONAR and satellite data.

3) Target Detection: Underwater target detection is a major component of many ocean-related applications such as archaeology and pipeline monitoring [278], [310]. Among the available pool of different data sources, the SONAR systems have been successfully used for a variety of different target detection proposes in underwater ocean environments [278], [311], [312], mostly because of their applicability in both shallow and deep waters. For example, Mukherjee *et al.* [311] proposed a computationally efficient data-driven method based on the symbolic dynamic and automata theory for underwater mine detection with a side-scan SONAR image. The authors evaluated the performance of the proposed method using 60 different SONAR images. Based on the results, the proposed method, when employed on side-scan SONAR images, correctly detected 90% of the available mines. Williams [310] implemented an unsupervised algorithm called Mondrian detector for target detection in synthetic aperture SONAR images. In this article, the author provided a general-purpose target detection algorithm that is applicable in the detection of different objects of different sizes, such as unexploded ordnance, pipelines, and shipwrecks. The effectiveness of the proposed methodology was demonstrated in six different synthetic aperture SONAR images acquired from different areas with diverse seafloor characteristics.

VIII. HF RADAR

Although different instruments, such as buoys, pressure sensors, current meters, and anemometers, are employed for the measurement of the surface ocean, they are not able to map an extensive region of the ocean and can only provide measurements for the point at which they are installed. Moreover, the cost of maintenance of these instruments and gathering data to cover a large area of the ocean using the aforementioned methods are high. Therefore, the RS systems, such as HF and X-band radars [313], [314], have been considered to overcome these limitations in the past few decades using the electromagnetic scattering theories to consider wave propagation effects [315]–[319]. It is worth mentioning that only surface gravity waves can be detected using HF radar and other types of sea waves, particularly capillary waves, require different instruments, such as X-band radar, to be detected [314]. HF radar has become an important technique in the monitoring of the sea surface due to the availability of Doppler processing. The high conductivity

of ocean water in groundwave propagation contributes to low attenuation and long-range over the horizon detection [320]. Crombie *et al.* [321] argued that Doppler-shifted echoes could be detected from radially approaching and receding ocean waves using an HF radar located in a coastal region. This argumentation resulted in using HF radar systems for extracting OSC, sea state, and OSW [322].

The scattering process by which an echo is transmitted from an HF radar system and returned to its origin is a selective procedure known as Bragg scattering contributing to the dominant backscattering from sea waves with the length of half of a radio wavelength [320]. The echo-Doppler spectrum obtaining from the sea surface consists of two discreet lines since the decametric waves selected by the Bragg mechanism travel radially toward and away from the HF radar sensor at a specific velocity identified by the wavelength. Traveling waves toward the radar produce positive Doppler shifts while sea waves with opposite directions produce a negative Doppler shift in the frequency domain. It should be noted that HF radars can also be utilized for ship and low-altitude aircraft tracking applications [323]. In this case, target echoes are identified by a disconnected line in the Doppler spectrum corresponding to the radial target speed and do not coincide with the radial wave speed associated with the Bragg scattering mechanism. Although the first-order scattering can be used for extracting OSW direction and OSW speed, for sea state sensing, the weaker second-order scattering, which is typically 20 dB lower than the Bragg scattering resonant amplitude, is employed [324]. The second-order scattering is associated with either the harmonies of nonsinusoidal ocean waves or single wave corresponding to the nonlinear hydrodynamic interaction of two crossing ocean waves, while the Bragg scattering mechanism includes scattering from single wave elements. Furthermore, the ocean surface is considered as a nondeterministic surface in which different waves, such as capillary, sound, gravity, and planetary waves, may combine at the same time in the observed region [325]. Consequently, due to the random behavior of the ocean surface, a stochastic approach should be employed in the study of the ocean surface, and the prediction of wave parameters can only be acquired by stochastic analysis of sea data. In the study of oceanography, the energy spectrum of the referred random variable is used, which is called the ocean wave spectrum. Kitaigorodskii *et al.* [326] derived a formulation for the spectral density using the fetch length X and friction velocity u_* as $F(\omega, g, u_*, X)$. However, the friction velocity is not a directly measured variable in this formulation. Subsequently, Pierson and Moskowitz [327] employed OSW speed U_h, which is the OSW speed at height h, and proposed a new formulation for the spectral density function as $F(\omega, g, U_h X)$. According to these two derivations, two of the most important wave models were proposed. The JONSWAP wave model illustrates local wind-generated seas with limited fetch, and it depends on the fetch length.

In order to extract surface ocean parameters, the HF radar backscatter along with the ocean wave spectrum is used. Fig. 5(a) presents the range-Doppler-spectrum (RDS) of a high-frequency surface wave (HFSW) radar sensor at the Argentia radar site, Canada in 2015, while the radar operated at 13.385 MHz [328].
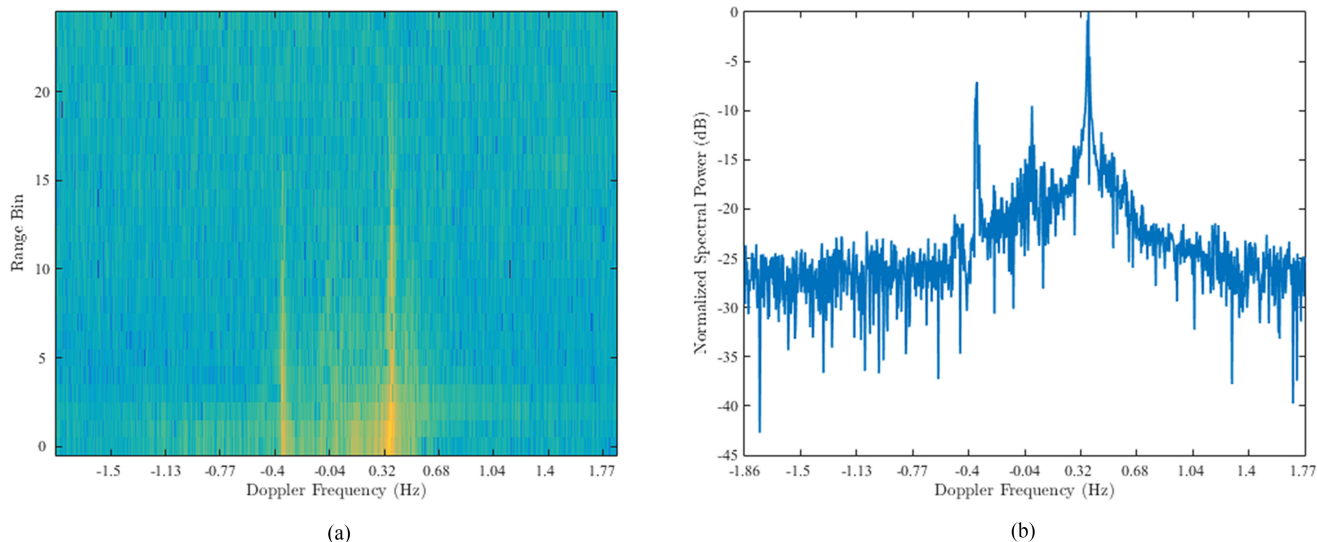
Fig. 5.   Spectral power of the radar backscatter (a) at various range bins (b) in the fourth range bin.

By considering the 3 km range bin resolution for this radar, the effective range is around 75 km. By extracting the radar backscatter in each range bin, the surface information can be extracted, as shown in Fig. 5(b). As is clear from this figure, the OSW blows toward the radar since the positive first-order radar backscatter has a higher amplitude in comparison with the negative first-order backscatter, and by acquiring the ratio between them, the exact OSW direction is calculated. It is worth mentioning that the Doppler shift of the first order is related to the radar backscatter with

$$\omega_b = \sqrt{2gk_0 \tanh\left(2k_0 d\right)} \tag{1}$$

in which d denotes the water depth, k_0 is the wavenumber of the radar system, and ω_b represents the angular frequency of the first-order radar backscatter. By assuming deepwater scattering $(2k_0 d \gg 1)$, $\omega_b \approx \sqrt{2gk_0}$. In other words, by knowing the radar frequency, the location of the first-order peak in the Doppler domain can be calculated and vice versa.

A. Applications

HF radar has several applications in target detection and radio oceanography to remotely measure the ocean parameters, such as OSW speed, OSW direction, OWH, and OSC. In this part, some of the aforementioned applications are discussed in detail.

1) Target Detection: Due to the surveillance importance of coastal waters, especially for economic exclusion zone (EEZ) applications, the use of HF surface wave radar (HFSWR) for target (e.g., surface vessels and low-altitude aircraft) detection has been increased. The range of detection is double the surface wave detection range, which is commonly in the order of hundreds of kilometers [329]. To detect ship targets, the backscattered electric fields should reflect from a large aperture area to reduce the illuminated clutter patch. Therefore, a wide aperture array on the receiver along with a digital beamforming technique is employed to provide the required directivity and resolution [329]. On the other hand, the HF band is in demand for broadcast communication making interference and influence on the detection performance of the radar [313]. In other words, an ideal signal processing tool should extract oceanographic and target information and suppress radio frequency interference (RFI) as well as external noise to improve the signal-to-noise ratio (SNR). Turley *et al.* [330] applied multiple CFAR techniques to HF radar data to acquire a high probability of detection for a given probability of false alarm and obtain the tracking stage of radar processing with constant and low false alarm rate. Other related techniques have also been applied to the radar signals to detect vessels, such as the adaptive detection technique [331], morphological component analysis [332], curvilinear regression analysis [333], and range-Doppler spectrum enhancement [334]. For instance, Khan and Power [323] investigated low altitude aircraft detection using an HF radar system. In this article, the ocean clutter was compared with the returned signal in each range cell to discriminate the low-altitude aircraft from the ocean clutter, and a signal processing along with a matched filter was applied to extract the aircraft backscatter signal. They performed an experiment on September 1, 1993, using the HF radar at Cape Race, Newfoundland, Canada. Fig. 6 shows the target range with respect to the time for both the GPS data and the radar-derived directions. As is clear, the radar extracted directions had a good agreement with the GPS data at various times.

To show the accuracy of the proposed approach in [323] for the detection of the low altitude aircraft, the target bearing was compared with the aircraft bearing recorded by the GPS system (see Fig. 7). The results showed that the signal processing allows the extraction of the azimuthal resolution better than 3°.

2) Ocean Wave Height: Significant OWH is an important parameter of the statistical distribution of ocean waves and is defined as the mean OWH of the highest third of the waves ($H_{1/3}$) [325]. This parameter can be measured using HF radar. Generally, OWH is associated with the integral of the second-order radar backscattered, and the beamforming should also be used to acquire the wave information at different positions (i.e., ranges and azimuth) [335]. A narrow-beam sensor with a large
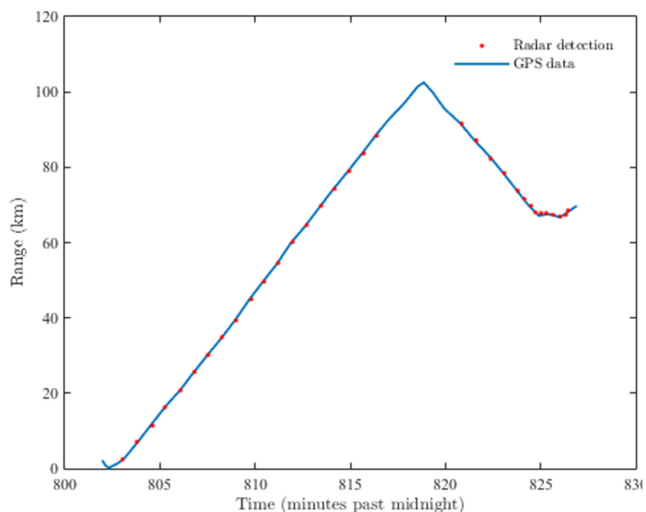
Fig. 6.   Range detection using HF radar and its comparison with GPS data [323].
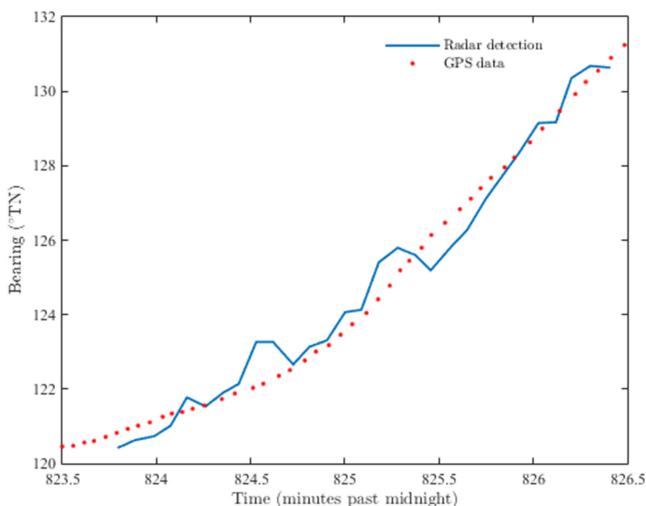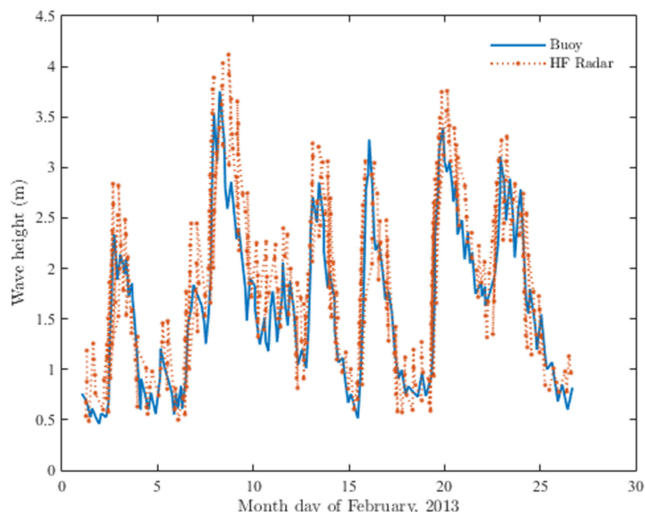

Fig. 8.   Comparison between the buoy and obtained results using the second-order radar cross section [335].

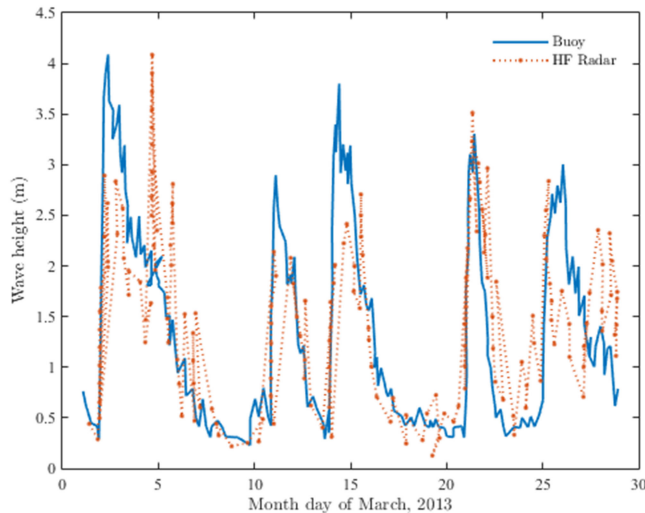Fig. 7.   Comparison between the GPS data and the HF radar for the aircraft bearing detection [323].

Fig. 9.   Estimation of significant OWH from the first-order Bragg peaks and its comparison with the buoy [336].

aperture is also essential for remotely OWH measurement to retrieve a wave map [335]. On the other hand, the second-order spectra covering a broad Doppler range are susceptible to the variation of the background noise floor, the external clutter, and radio interferences. For instance, Tian *et al.* [335] presented a new wave-height mapping approach based on the second-order harmonic peak (SHP) of radar Doppler spectra. This method was based on the ratio of SHP power and Bragg peak power. To evaluate this approach, a nearly 30-day field experiment was accomplished on the coast of Fujian, China, from February 1 to February 28, 2013, using a broad-beam radar system operating at 13 MHz with a range resolution of 2.5 km.

Fig. 8 shows the OWH comparison between the proposed method and buoy data. The results using HF radar followed the buoy data on different days. It should be noted that the second-order spectra analysis for extracting OWH is often susceptible to external noise, and first-order Bragg peaks can be used for

extracting OWH since the first-order Bragg peak power is more than the power of the second-order scattering. For example, Zhou *et al.* [336] proposed a method for extracting OWH from the first-order Bragg peaks, which is applicable for low or moderate sea states (see Fig. 9). As is obvious, the results using HF radar followed the buoy data on different days.

3) Ocean Surface Current: Accurate estimation of OSC is important for coastal management. Measuring this parameter has several important applications, such as tracking of drifting vessels during search and rescue, prediction of dispersion rates in OOS events, and fishery investigations [337]. Nonetheless, collecting OSC velocity using conventional systems is a difficult task, and the collected data are not quite accurate because the measurement devices are usually maintained at a depth exceeding 15 m. Additionally, many devices are required to map extensive regions of the ocean. An alternative to the in-situ technique is HF radar. For example, Hickey *et al.* [337] proposed
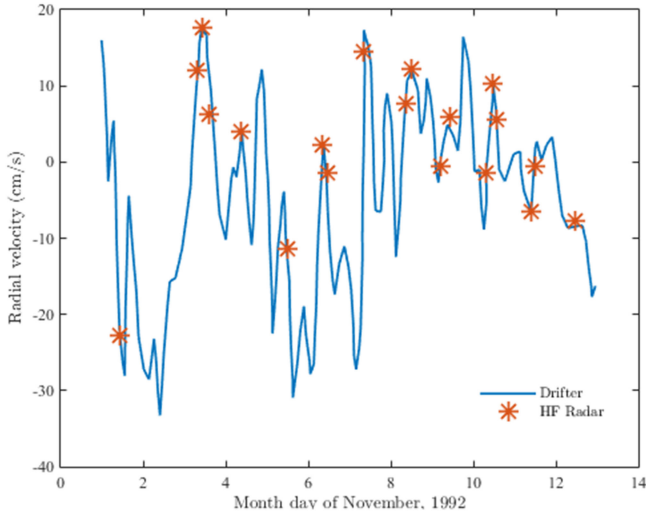
Fig. 10.   Radial velocity obtained by a drifter and its comparison with extracted values using HF radar [337].

Fig. 11.   OSW speed with respect to the second-order peak position [324].

a technique for extracting radial OSC using spectral analysis applied to the Cape Race system located in Newfoundland, Canada, during the period of October 20 to November 21, 1992. Fig. 10 shows the time series of the radial velocity obtained using buoy and HF radar. It should be noted that these values have been obtained over a wide range of oceanographic conditions and do not depend on the sea state.

4) Ocean Surface Wind: The first and second-order radar cross section along with the ocean wave spectral model should be considered to extract surface OSW speed. For surface OSW extraction, the second-order radar cross section can be used, which is as follows according to the Barrick derivations [317], [318]:

$$\sigma_{2p}(\omega_d) \approx 2^6 \pi^2 k_0^4 \sum_{m_1 = \pm 1} \sum_{m_2 \pm 2} \int_{-\pi}^{\pi} \int_0^{\infty} S\left(m_1 \overrightarrow{K_1}\right) S\left(m_2 \overrightarrow{K_2}\right)$$

$$|\Gamma_H|^2 \delta \left(\omega_d + m_1 \sqrt{gK_1} + m_2 \sqrt{gK_2}\right) K_1 \, dK_1 \, d\theta_{K_1} \qquad (2)$$

where $\overrightarrow{K_1}$ and $\overrightarrow{K_2}$ are the ocean wavenumber components with the direction of θ_{K_1} and θ_{K_2}. Additionally, ω_d denotes the Doppler frequency, $S(.)$ represents the ocean wave spectrum, $\delta(.)$ is the Dirac delta function, Γ denotes the coupling coefficient, and parameters m_1 and m_2 can be ± 1 delineating four different Doppler regions of the cross section. OSW speed can be estimated by applying the derivative with respect to ω_d and considering the delta constraint in (2) [324], [338]. Fig. 11 depicts OSW speed at various Doppler frequencies of the second-order peak. As can be seen, the inversion result obtained from the modeled second order had a good agreement with the observed second-order peak locations for the radar cross section generated for different OSW speeds. It should be noted that the corresponding HF radar was operating at 15 MHz, and Pierson–Moskowitz wave model has been employed.

IX. CONCLUSION

Oceans are invaluable resources that play a pivotal role in many natural processes of the earth and provide many benefits to humans. Therefore, establishing reliable and consistent proxies to monitor and study oceans is of notable importance. In this regard, RS systems with diverse characteristics are recognized as an efficient data source for ocean-related studies. This article reviewed seven active RS systems for ocean studies.

SCAs were the first active RS system, collecting information in the microwave domain of the electromagnetic spectrum. Satellite scatterometry was started from the SASS launch, which confirmed the feasibility of using SCAs for OSW studies. Subsequently, other SCAs with advanced technologies, such as AS-CAT series, CFOSAT, and HY-2A, were launched. Currently, the accurate OSW properties derived from SCAs are broadly used for location-allocation of offshore renewable energy structure, cold pools delineation in the ocean, and cyclone and typhoon studies. Additionally, these active systems were employed in SI studies to quantify SI age, size, and thickness.

Altimeters are another active RS system operating in different microwave bands (i.e., C-, S-, Ka-, Ku-bands) to measure the SSH by measuring the travel time of the transmitted pulse. Satellite altimetry started with the TOPEX/Poseidon and continued by the Jason series, and more recently, Sentinel-3 SRAL systems. Given the importance of SSH for many applications, altimeters are considered a unique source of RS data. In particular, the up-to-date and historical altimetry data allow measuring accurate SSH for diverse applications including marine geoid, ocean circulation, OT, fronts and eddies, ENSO, and meteorology.

Gravimeters are among active RS systems, which have the lowest number of launched sensors into space. In particular, until recently, only four satellite constellations, including CHAMP, GOCE, GRACE, and GRACE-FO, were launched. These systems use the satellite-to-satellite tracking technique to measure the Earth's gravity field. Consequently, their data enable the production of precise geopotential models and estimation of Earth's gravity field coefficients. Additionally, the collected

gravimetry data were employed for other applications, such as OBP, deep ocean current, sea level, and ocean heat studies, based on the mass redistribution concept. However, these systems suffer from coarse spatial resolution, limiting their use for local and small-scale studies.

SAR is one of the mostly-used active RS systems for ocean studies due to providing several advantages, especially higher spatial resolution. These systems acquire surface information in various microwave bands and with different polarizations. Sentinel-1, ALOS-2, COSMO-SkyMed, and RADARSAT are among SAR sensors that have been widely used for ocean studies. The possibility of acquiring data with different configurations permits SAR data in a variety of applications, including OSW, OWH, OSC, SI, OOS, ship detection, and bathymetry.

Collecting surface information using laser pulse in the visible and infrared regions of the electromagnetic spectrum makes LiDAR data another active RS system for oceanographic applications. Currently, there are not many spaceborne LiDAR system for oceanographic studies and airborne and shipborne LiDAR systems are mostly in use. However, several attempts were made to employ CALIOP and ICESat-2, which have been originally designed for other disciplines, for oceanographic applications. Available LiDAR data were broadly employed for bathymetry, aquatic vegetation mapping and monitoring, underwater archaeology, and OT studies. Despite the interested application, two quantities of attenuation and backscattering coefficient should be precisely calculated using inversion approaches for further investigations.

The possibility of working in the underwater environment with high reliability discriminates SONAR sensors from other active RS systems. Active SONAR systems work under the fundamentals of sound propagation in water and are basically divided into four categories of single-beam, side-scan, multi-beam, and synthetic aperture SONAR. Unique data collected by SONAR systems were applied to different ocean studies for bathymetry and geomorphology, aquatic vegetation mapping, and ship detection.

In this article, the last active RS system reviewed was HF radar. The HF radar systems are mainly utilized to observe the ocean surface from coastal areas. In this regard, their data were extensively used for target detection (e.g., surface vessel), OWH, OSC, and OSW.

In this part, seven active RS systems were comprehensively reviewed, each of which possesses specific characteristics and provides ocean-related observations from different perspectives. Despite the main applications of each system, several oceanographic applications are common between these systems. Consequently, their integration can provide complementary data for several tasks, enhancing the expected results. Therefore, having sufficient knowledge about different RS systems for ocean studies, which is provided through this review article, can help researchers to properly use RS data either separately or in conjunction to obtain satisfactory results.

APPENDIX

See Table III–VII.

TABLE III
ACRONYMS AND CORRESPONDING DESCRIPTIONS

Acronym	Description
ALOS-2	Advanced Land Observation Satellite-2
AMI	Advanced Microwave Instrument
ASCAT	Advanced Scatterometer
ASAR	Advanced Synthetic Aperture Radar
ASI	Agenzia Spaziale Italiana
AVISO	Archiving, Validating, and Interpretation of Satellite Oceanographic Data
AR5	Assessment Report 5
CSA	Canadian Space Agency
CNES	Centre National d'Edudes Spatiales
CHAMP	Challenging Minisatellite Payload
CNSA	China National Space Administration
CFOSAT	Chinese-French Oceanography Satellite
CALIPSO	Cloud-Aerosol LiDAR and Infrared Pathfinder Satellite Observations
CALIOP	Cloud-Aerosol LiDAR with Orthogonal Polarization
COSMO-SkyMed	Constellation of Small Satellites for Mediterranean basin Observation
DOSCN	Deep Oil Spill Convolutional Network
DT-MSLA	Delayed Time Mean Sea Level Anomaly
DCA	Doppler Centroid Anomaly
DOT	Dynamic Ocean Topography
EEZ	Economic Exclusion Zone
ENSO	El Nino-Southern Oscillation
Envisat	Environmental Satellite
ECMWF	European Centre for Medium-Range Weather Forecasts
EUMETSAT	European Organization for the Exploitation of Meteorological Satellites
ERS-1	European Remote-Sensing Satellite-1
ESA	European Space Agency
GPR	Gaussian Process Regression
GMC	Generalized Minimax Concave
GMF	Geophysical Model Function
GMSL	Global Mean Sea Level
GMES	Global Monitoring for Environment and Security
GOME	Global Ozone Monitoring Experiment
GPS	Global Positioning System
GRACE-FO	GRACE Follow-On
GOCE	Gravity Field and Steady-State Ocean Circulation Explorer
GRACE	Gravity Recovery and Climate Experiment
HY	Haiyang
HFSWR	HF surface wave radar
HF	High Frequency
HFSW	high-frequency surface wave
InSAR	Interferometric SAR
ISRO	Indian Space Research Organization
IPCC	Intergovernmental Panel on Climate Change
ISW	Internal Solitary Waves
ISS	International Space Station
IPBS	intra-pulse beam switching
MoD	Italian Ministry of Defense
MUR	Italian Ministry of Research
JAXA	Japan Aerospace Exploration Agency
LiDAR	Light Detection and Ranging
LB	Lofoten Basin
MDA	MacDonald Dettwiler Associates Limited
ML	Machine Learning
Mascons	Mass Concentration Blocks
MSL	Mean Sea Level
METOP	Meteorological Operational Satellite Program
NSCAT	NASA Scatterometer
NASA	National Aeronautics and Space Administration
NOAA	National Oceanic and Atmospheric Administration
NN	Neural Network
NWP	Numerical Weather Prediction
OBP	Ocean Bottom Pressure
OOS	Ocean Oil Spill
OSC	Ocean Surface Current
OSW	Ocean Surface Wind
OT	Ocean Tide
OWH	Ocean Wave Height
OSCAT	OceanSat Scatterometer
POD	Precise Orbit Determination
RFI	Radio Frequency Interference
RD	Range-Doppler
RDS	Range-Doppler-Spectrum
RAPID	Rapid Climate Change/Meridional Overturning Circulation and Heatflux Array Observational Program
RS	Remote Sensing
SIRAL	SAR/Interferometric Radar Altimeter
SI	Sea Ice
SSH	Sea Surface Height
SST	sea surface temperatures
SASS	SeaSat-A/Scatterometer System
SHP	Second-Order Harmonic Peak
SNR	Signal-to-Noise Ratio
SLC	Single Look Complex
SONAR	Sound Navigation and Ranging
SAR	Synthetic Aperture Radar
SRAL	Synthetic Aperture Radar Altimeter
WM	Wave Mode
WSOA	Wide-Swath Ocean Altimeter
WindRad	Wind Radar scatterometer

TABLE IV
SCATTEROMETERS FOR OCEAN STUDIES

Satellite	Sensor	Temporal resolution (day)	Spatial resolution (km)	Channels (frequency)	Time Period Available
SeaSat-A	SASS	1.5	50	Ku-band (14.599 GHz)	1978-1978
ERS-1/2	AMI	3	50	C-band (5.3 GHz)	1991 – 2011
ADEOS	NSCAT	1.5	50	Ku-band (13.995 GHz),	1996-1997
QuikSCAT/ADEOS-2	SeaWinds	1	50	Ku-band (13.4 GHz)	1999- 2003
METOP-A,B,C	ASCAT-A	1.5	50	C-band (5.255 GHz)	2006 - ongoing
Oceansat-2	OSCAT	1	50	Ku-band (13.515 GHz)	2009 - ongoing
HY2-A, B, C, D	HSCAT	1	50	Ku-band (13.25 GHz)	2012 - ongoing
ISS-RapidScat	RapidScat	2	50	Ku-band (13.4 GHz)	2014 - 2016
CFOSAT	SCAT	7	50	Ku-band (13.256 GHz)	2018-ongoing
Feng-Yun – 3E	Wind Rad	1	C-band: 25 Ku-band: 10	C-band (5.3 GHz) and Ku-band (13.265 GHz)	2021-ongoing
METOP-SG-B	SCA	1.5	Nominal: 25 High-resolution mode: 15-20	C-band (5.355 GHz)	2022

TABLE V
ALTIMETERS FOR OCEAN STUDIES

Satellite	Sensor	Temporal resolution (day)	Measurement accuracy (m)	Channels (frequency(GHz)	Time Period
TOPEX	SLR,LRA,DORIS, experimental GPS receiver	10	0.042	13.752 and 5.3	1992- 2006
SeaSat	ALT	17	-	13.5	1978-1978
HY-2A/B/C	-	14	0.03	13.58 and 5.25	2011-ongoing
SARAL/Altika	Doppler Orbitography, LRA, DORIS, ARGOS-3	35	0.02-0.03	35.75	2013-ongoing
ENVISAT	RA-2	35	0.025-0.03	13.58 and 3.2	2002-2012
CRYOSAT-2	SIRAL,LRR	30	0.05	13.58	2010-ongoing
GEOSAT	RA single-frequency radar altimeter	17	0.1	13.5	1985-1990
GFO	TRANET, LRA, GPS dual-frequency receivers	17	-	13.5	1998-2008
Sentinel-3A/B	SLSTR,OLCI,DORIS,MWR	27	0.03	13.575 and 5.3	2016-ongoing
Sentinel-6	Michael Freilich	10	-	18.7,23.8, 34	2020-ongoing
GPS, GLONASS, GALILEO, Beidou/COMPASS	GNSS altimetry	Near-real-time	-	-	1994-ongoing
Jason-1/2/3	JMR,LRA,TRSR, AMR, DORIS, TRSR-2, AMR-2, GPSP, DORIS	~10	0.03-0.04	13.752 and 5.3	2001-ongoing
ERS-1/2	RA	35	0.05	13.8	1991-2011
ICESAT-1/2	GLAS, ATLAS	91	20	-	2003-ongoing
SWOT	Ka-band Radar Instrument (KaRIn)	21	-	-	2022

TABLE VI
SPACEBORNE LIDAR SYSTEMS FOR OCEAN STUDIES

Satellite	Sensor	Temporal resolution (Days)	Spatial resolution (m)	Frequency (GHz)	Time period
Envisat	ASAR	35	30/150	C (5.25)	2002–2012
ERS-1/2	AMI/VV	35	25/50000	C (5.25)	1991–2011
CryoSat-2	SIRAL	30	250-15000	Ku (13.5)	2005-present
RCM	-	4	5– 50	-	2019-ongoing
KOMPSAT-5	COSI	28	1-20	X (9.66)	2013-ongoing
Sentinel-1 A/B	SAR-C	6	5/40	C (5.405)	2014-ongoing
Seasat-A	SAR	24	25	L (1.25)	1978–1978
Radarsat-1/2	SAR-C	24	10/100-30/100	C (5.3)	1995–ongoing
HJ-1 C	SAR-S	31	20	S (3.13)	2012-ongoing
ALOS-2	PALSAR	14	10/ 100	L (1.2)	2014-ongoing
COSMO-SkyMed	SAR 2000	16	3	X (9.6)	2007–ongoing
JERS-1	SAR	44	18	L (1.275)	1992-1998
TerraSAR-X/ TanDEM-X	SAR-X	11	1, 3, 16	X(9.65)	2007-ongoing

TABLE VII
SAR SYSTEMS FOR OCEAN STUDIES

Satellite	Sensor	Temporal resolution	Spatial resolution (m)	Wavelength	Time period
ICESat	GLAS	91 days	150	532, 1064	2003-2006
CALIPSO	CALIOP	98.5 minutes	333	532, 1064	2006-ongoing
ISS	CATS	~ a few minutes	7000	355, 532, 1064	2014-ongoing
ISS	GEDI	60 minutes	60	1064	2018-ongoing
ADM-Aeolus	ALADIN	12 hours	500-2000	355	2018-ongoing
ICESat-2	ATLAS	91 days	0.7	1064	2018-ongoing

AUTHOR CONTRIBUTION

REFERENCES

[1] M. Amani *et al.*, "Remote sensing systems for ocean: A review (Part 1: Passive systems)," *IEEE J. Sel. Topics Appl. Earth Obs. Remote Sens.*, vol. 15, pp. 210–234, Dec. 2021, doi: 10.1109/JSTARS.2021.3130789.

[2] W. M. Brown and L. J. Porcello, "An introduction to synthetic-aperture radar," *IEEE Spectr.*, vol. 6, no. 9, pp. 52–62, Sep. 1969, doi: 10.1109/MSPEC.1969.5213674.

[3] L. Zhu, J. Suomalainen, J. Liu, J. Hyyppä, H. Kaartinen, and H. Haggren, "A review: Remote sensing sensors," *Multi-Purposeful Appl. Geospatial Data*, pp. 19–42, 2018.

[4] C. Toth and G. Jóźków, "Remote sensing platforms and sensors: A survey," *ISPRS J. Photogramm. Remote Sens.*, vol. 115, pp. 22–36, 2016.

[5] P. S. Roy, M. D. Behera, and S. K. Srivastav, *Satellite Remote Sensing: Sensors, Applications and Techniques*. Berlin, Germany: Springer, 2017.

[6] A. K. Ulaby, F. T. Moore, and R. K. Fung, *Microwave Remote Sensing: Active and Passive, Volume II: Radar Remote Sensing and Surface Scattering and Emission Theory*. Boston, MA, USA: Addison-Wesley, 1982.

[7] Q. Vanhellemont, G. Neukermans, and K. Ruddick, "Synergy between polar-orbiting and geostationary sensors: Remote sensing of the ocean at high spatial and high temporal resolution," *Remote Sens. Environ.*, vol. 146, pp. 49–62, 2014.

[8] M. E. Hodgson and B. Kar, "Modeling the potential swath coverage of nadir and off-nadir pointable remote sensing satellite-sensor systems," *Cartography Geographic Inf. Sci.*, vol. 35, no. 3, pp. 147–156, 2008.

[9] C. K. Toth, K. Jezek, F. Meyer, B. Osmanoglu, S. A. Morain, and A. M. Budge, "Sensors and platforms," in *Manual of Remote Sensing*, 4th ed., vol. 121. Bethesda, MD, USA: Amer. Soc. Photogrammetry and Remote Sens., 2019, pp. 121–210.

[10] S. Guillaso, A. Reigber, L. Ferro-Famil, and E. Pottier, "Range resolution improvement of airborne SAR images," *IEEE Geosci. Remote Sens. Lett.*, vol. 3, no. 1, pp. 135–139, Jan. 2006.

[11] C. Oliver and S. Quegan, *Understanding Synthetic Aperture Radar Images*. Tambaram, India: SciTech, 2004.

[12] R. O. Dubayah and J. B. Drake, "Lidar remote sensing for forestry," *J. Forestry*, vol. 98, no. 6, pp. 44–46, 2000.

[13] F. T. Ulaby, R. K. Moore, and A. K. Fung, *Microwave Remote Sensing: Active and Passive. Volume 1-Microwave Remote Sensing Fundamentals and Radiometry*. Boston, MA, USA: Addison-Wesley, 1981.

[14] J. J. Van Zyl, *Synthetic Aperture Radar Polarimetry*, vol. 2. Hoboken, NJ, USA: Wiley, 2011.

[15] J. Vogelzang and A. Stoffelen, "Scatterometer wind vector products for application in meteorology and oceanography," *J. Sea Res.*, vol. 74, no. 2012, pp. 16–25, 2012, doi: 10.1016/j.seares.2012.05.002.

[16] H. Hersbach, "Comparison of C-Band scatterometer CMOD5.N equivalent neutral winds with ECMWF," *J. Atmos. Ocean. Technol.*, vol. 27, no. 4, pp. 721–736, Apr. 2010, doi: 10.1175/2009JTECHO698.1.

[17] S. Martin, *An Introduction to Ocean Remote Sensing*. Cambridge, U.K.: Cambridge Univ. Press, 2014.

[18] W. T. Liu, "Progress in scatterometer application," *J. Oceanogr.*, vol. 58, no. 1, pp. 121–136, 2002, doi: 10.1023/A:1015832919110.

[19] J.W. Pierson and Jr. , "Highlights of the Seasat-SASS program: A review," in *Proc. Satell. Microw. Remote Sens.*, 1983, pp. 69–86.

[20] S. Peteherych, M. G. Wurtele, P. M. Woiceshyn, D. H. Boggs, and R. Atlas, "First global analysis of SEASAT scatterometer winds and potential for meteorological research," in *Proc. NASA Conf. Publ. CP2303*, 1984, pp. 575–585.

[21] A. C. M. Stoffelen and G. J. Cats, "The impact of Seasat-A scatterometer data on high-resolution analyses and forecasts: The development of the QE II storm," *Monthly Weather Rev.*, vol. 119, no. 12, pp. 2794–2802, Dec. 1991, doi: 10.1175/1520-0493(1991)119<2794:TIOASD>2.0.CO;2.

[22] A. Stoffelen and D. Anderson, "Scatterometer data interpretation: Estimation and validation of the transfer function CMOD4," *J. Geophys. Res. Ocean.*, vol. 102, no. C3, pp. 5767–5780, Mar. 1997, doi: 10.1029/96JC02860.

[23] F. M. Naderi, M. H. Freilich, and D. G. Long, "Spaceborne radar measurement of wind velocity over the ocean-an overview of the NSCAT scatterometer system," *Proc. IEEE*, vol. 79, no. 6, pp. 850–866, Jun. 1991, doi: 10.1109/5.90163.

[24] S. M. L. Ross and N. Hoffman, "An introduction to the near – real – time QuikSCAT data," *Weather Forecasting*, vol. 20, pp. 476–493, 2005, [Online]. Available: https://doi.org/10.1175/WAF841.1

[25] J. Figa-Saldaña, J. J. W. Wilson, E. Attema, R. Gelsthorpe, M. R. Drinkwater, and A. Stoffelen, "The advanced scatterometer (ASCAT) on the meteorological operational (MetOp) platform: A follow on for European wind scatterometers," *Can. J. Remote Sens.*, vol. 28, no. 3, pp. 404–412, Jan. 2002, doi: 10.5589/m02-035.

[26] T. Remmers, F. Cawkwell, C. Desmond, J. Murphy, and E. Politi, "The potential of advanced scatterometer (ASCAT) 12.5 km coastal observations for offshore wind farm site selection in Irish waters," *Energies*, vol. 12, no. 2, Jan. 2019, Art. no. 206, doi: 10.3390/en12020206.

[27] A. Verhoef, J. Vogelzang, and A. Stoffelen, "Oceansat-2 L2 winds data record validation report," Tech. Rep. SAF/OSI/CDOP3/KNMI/TEC/RP/298, Royal Netherlands Meteorological Institute (KNMI), De Bilt, The Netherlands, 2017.

[28] O&SI SAF Project Team, "Oceansat-2 wind product user manual," Tech. Rep. saf/OSI/CDOP/KNMI/TEC/MA/??, Royal Netherlands Meteorological Institute (KNMI), De Bilt, The Netherlands, 2013.

[29] J. Yang and J. Zhang, "Accuracy assessment of HY-2A scatterometer wind measurements during 2011–2017 by comparison with buoys, ASCAT, and ERA-Interim data," *IEEE Geosci. Remote Sens. Lett.*, vol. 16, no. 5, pp. 727–731, May 2019, doi: 10.1109/LGRS.2018.2879909.

[30] O&SI SAF Project Team, "RapidScat wind product user manual," Tech. Rep. SAF/OSI/CDOP2/KNMI/TEC/MA/227, Royal Netherlands Meteorological Institute (KNMI), De Bilt, The Netherlands, 2016.

[31] EoPortal, "CFOSAT (Chinese–French oceanography satellite)," in *Proc. CFOSAT*, 2013.

[32] W. Lili, D. Zhenyu, Z. Lei, and Y. A. N. Cheng, "CFOSAT-1 realizes first joint observation of sea wind and waves," *Aerosp. China*, vol. 20, no. 1, pp. 20–27, 2019.

[33] S. A. F. Osi, C. Knmi, T. E. C. Tn, Z. Li, A. Stoffelen, and A. Verhoef, "CFOSAT and windrad rotating Fan-beam SCATterometer simulation and wind retrieval performance evaluation," SAF/OSI/CDOP3/KNMI/TEC/TN/348NWPSAF-KN-TR-029, Royal Netherlands Meteorological Institute (KNMI), De Bilt, The Netherlands, 2019.

[34] Z. Li, A. Stoffelen, and A. Verhoef, "A generalized simulation capability for rotating- beam scatterometers," *Atmos. Meas. Tech.*, vol. 12, no. 7, pp. 3573–3594, Jul. 2019, doi: 10.5194/amt-12-3573-2019.

[35] C. C. Lin, M. Betto, M. Belmonte Rivas, A. Stoffelen, and J. De Kloe, "EPS-SG windscatterometer concept tradeoffs and wind retrieval performance assessment," *IEEE Trans. Geosci. Remote Sens.*, vol. 50, no. 7 PART1, pp. 2458–2472, 2012, doi: 10.1109/TGRS.2011.2180393.

[36] A. Isaksen and Stoffelen L, "ERS-scatterometer wind data impact on ECMWF's tropical cyclone forecasts," *IEEE Trans. Geosci. Remote Sens.*, vol. 38, no. 4, pp. 1885–1892, Jul. 2000, doi: 10.21957/i5a9w9a1.

[37] A. Stoffelen and P. van Beukering, "The impact of improved scatterometer winds on HIRLAM analyses and forecasts," *BCRS Study Contract*, vol. 1, 1997.

[38] P. Garg *et al.*, "Identifying and characterizing tropical oceanic mesoscale cold pools using spaceborne scatterometer winds," *J. Geophys. Res. Atmos.*, vol. 125, no. 5, Mar. 2020, Art. no. e2019JD031812, doi: 10.1029/2019JD031812.

[39] T. Valkonen, H. Schyberg, and J. Figa-Saldana, "Assimilating advanced scatterometer winds in a high-resolution limited area model over northern Europe," *IEEE J. Sel. Topics Appl. Earth Obs. Remote Sens.*, vol. 10, no. 5, pp. 2394–2405, May 2017, doi: 10.1109/JSTARS.2016.2602889.

[40] C. M. Risien and D. B. Chelton, "A global climatology of surface wind and wind stress fields from eight years of QuikSCAT scatterometer data," *J. Phys. Oceanogr.*, vol. 38, no. 11, pp. 2379–2413, Nov. 2008, doi: 10.1175/2008JPO3881.1.

[41] W. T. Liu, X. Xie, and W. Tang, "Scatterometer's unique capability in measuring ocean surface stress," in *Oceanography From Space*. Dordrecht, The Netherlands: Springer, 2010, pp. 93–111.

[42] N. Jaiswal, C. M. Kishtawal, and P. K. Pal, "Prediction of tropical cyclogenesis in North Indian ocean using oceansat-2 scatterometer (OSCAT) winds," *Meteorol. Atmos. Phys.*, vol. 119, no. 3/4, pp. 137–149, Feb. 2013, doi: 10.1007/s00703-012-0230-8.

[43] X. Xu, X. Dong, L. Zhang, D. Zhu, and S. Lang, "Wind speed retrieving for combined observations of scatterometer and radiometer onboard HY-2A for typhoons using neural network," in *Proc. IEEE Int. Geosci. Remote Sens. Symp.*, Jul. 2017, pp. 2164–2166, doi: 10.1109/IGARSS.2017.8127415.

[44] N. Ebuchi, "Evaluation of marine vector winds observed by rapidscat on the international space station using statistical distribution," in *Proc. IEEE Int. Geosci. Remote Sens. Symp.*, Jul. 2015, pp. 4901–4904, doi: 10.1109/IGARSS.2015.7326930.

[45] J. Yackel *et al.*, "Snow thickness estimation on first-year sea ice from late winter spaceborne scatterometer backscatter variance," *Remote Sens.*, vol. 11, no. 4, Feb. 2019, Art. no. 417, doi: 10.3390/rs11040417.

[46] M. Belmonte Rivas, I. Otosaka, A. Stoffelen, and A. Verhoef, "A scatterometer record of sea ice extents and backscatter: 1992–2016," *Cryosphere*, vol. 12, no. 9, pp. 2941–2953, Sep. 2018, doi: 10.5194/tc-12-2941-2018.

[47] A. Tarpanelli and J. Benveniste, "On the potential of altimetry and optical sensors for monitoring and forecasting river discharge and extreme flood events," in *Extreme Hydroclimatic Events and Multivariate Hazards in a Changing Environment*. Amsterdam, The Netherlands: Elsevier, 2019, pp. 267–287.

[48] X. Sui, R. Zhang, F. Wu, Y. Li, and X. Wan, "Sea surface height measuring using InSAR altimeter," *Geodesy Geodynamics*, vol. 8, no. 4, pp. 278–284, 2017.

[49] P. L. Vu *et al.*, "Multi-satellite altimeter validation along the French Atlantic coast in the southern Bay of Biscay from ERS-2 to SARAL," *Remote Sens.*, vol. 10, no. 1, 2018, Art. no. 93.

[50] C. J. Leuschen *et al.*, "Combination of laser and radar altimeter height measurements to estimate snow depth during the 2004 Antarctic AMSR-E Sea ice field campaign," *J. Geophys. Res. Ocean.*, vol. 113, 2008, Art. no. C4.

[51] A. C. Brenner, J. P. DiMarzio, and H. J. Zwally, "Precision and accuracy of satellite radar and laser altimeter data over the continental ice sheets," *IEEE Trans. Geosci. Remote Sens.*, vol. 45, no. 2, pp. 321–331, Feb. 2007.

[52] L.-L. Fu and A. Cazenave, *Satellite Altimetry and Earth Sciences: A Handbook of Techniques and Applications*. Amsterdam, The Netherlands: Elsevier, 2000.

[53] L.-L. Fu, D. B. Chelton, and V. Zlotnicki, "Satellite altimetry: Observing ocean variability from space," *Oceanography*, vol. 1, no. 2, pp. 4–58, 1988.

[54] C. C. Kilgus and J. L. MacArthur, "The navy Geosat mission radar altimeter satellite program," *RSFR*, vol. 2, pp. 787–790, 1984.

[55] D. B. Chelton, J. C. Ries, B. J. Haines, L.-L. Fu, and P. S. Callahan, "Satellite altimetry," in *International Geophysics*, vol. 69. Amsterdam, The Netherlands: Elsevier, 2001.

[56] D. Ciani, M.-H. Rio, B. B. Nardelli, H. Etienne, and R. Santoleri, "Improving the altimeter-derived surface currents using sea surface temperature (SST) data: A sensitivity study to SST products," *Remote Sens.*, vol. 12, no. 10, 2020, Art. no. 1601.

[57] C. C. Kilgus, J. L. MacARTHUR, and P. V. K. Brown, "Remote sensing by radar altimetry," *Johns Hopkins APL Tech. Dig.*, vol. 5, no. 4, pp. 341–345, 1984.

[58] J. Benveniste, "Radar altimetry: Past, present and future," in *Coastal Altimetry*. Berlin, Germany: Springer, 2011, pp. 1–17.

[59] F. L. Müller, C. Wekerle, D. Dettmering, M. Passaro, W. Bosch, and F. Seitz, "Dynamic ocean topography of the northern Nordic Seas: A comparison between satellite altimetry and ocean modeling," *Cryosphere*, vol. 13, pp. 611–626, 2019.

[60] C. Lithgow-Bertelloni and P. G. Silver, "Dynamic topography, plate driving forces and the African superswell," *Nature*, vol. 395, no. 6699, pp. 269–272, 1998.

[61] E. B. L. Mackay, C. H. Retzler, P. G. Challenor, and C. P. Gommenginger, "A parametric model for ocean wave period from Ku band altimeter data," *J. Geophys. Res. Ocean.*, vol. 113, no. C3, 2008, Art. no. C03029.

[62] E. A. Zakharova *et al.*, "Sea ice leads detection using SARAL/AltiKa altimeter," *Mar. Geodesy*, vol. 38, pp. 522–533, 2015.

[63] G. S. E. Lagerloef, G. T. Mitchum, R. B. Lukas, and P. P. Niiler, "Tropical pacific near-surface currents estimated from altimeter, wind, and drifter data," *J. Geophys. Res. Ocean.*, vol. 104, no. C10, pp. 23313–23326, 1999.

[64] F. Papa, B. Legrésy, and F. Rémy, "Use of the topex–poseidon dual-frequency radar altimeter over land surfaces," *Remote Sens. Environ.*, vol. 87, no. 2/3, pp. 136–147, 2003.

[65] F. Frappart *et al.*, "Radar altimetry backscattering signatures at ka, ku, c, and s bands over West Africa," *Phys. Chem. Earth, Parts A/B/C*, vol. 83, pp. 96–110, 2015.

[66] H. Guo, M. F. Goodchild, and A. Annoni, *Manual of Digital Earth*. Berlin, Germany: Springer, 2020.

[67] J. Acker *et al.*, *Remote Sensing From Satellites*. Berlin, Germany: Springer, 2014.

[68] V. Enjolras, P. Vincent, J.-C. Souyris, E. Rodriguez, L. Phalippou, and A. Cazenave, "Performances study of interferometric radar altimeters: From the instrument to the global mission definition," *Sensors*, vol. 6, no. 3, pp. 164–192, 2006.

[69] B. D. Pollard *et al.*, "The wide swath ocean altimeter: Radar interferometry for global ocean mapping with centimetric accuracy," in *Proc., IEEE Aerosp. Conf.*, 2002, Art. no. 2.

[70] E. Rodriguez and B. Pollard, "Centimetric sea surface height accuracy using the wide-swath ocean altimeter," in *Proc. IEEE Int. Geosci. Remote Sens. Symp.*, 2003, vol. 5, pp. 3011–3013.

[71] H. J. Zwally and A. C. Brenner, "Ice sheet dynamics and mass balance," in *International Geophysics*, vol. 69. Amsterdam, The Netherlands: Elsevier, 2001, pp. 351–xxvi.

[72] W. Munk, "The evolution of physical oceanography in the last hundred years," *Oceanogr. DC-Oceanogr. Soc.*, vol. 15, no. 1, pp. 135–142, 2002.

[73] P. Bonnefond *et al.*, "The benefits of the Ka-band as evidenced from the SARAL/AltiKa altimetric mission: Quality assessment and unique characteristics of Altika data," *Remote Sens.*, vol. 10, no. 1, 2018, Art. no. 83.

[74] J. Verron *et al.*, "The SARAL/AltiKa altimetry satellite mission," *Mar. Geodesy*, vol. 38, pp. 2–21, 2015.

[75] L. Fu *et al.*, "TOPEX/POSEIDON mission overview," *J. Geophys. Res. Ocean.*, vol. 99, no. C12, pp. 24369–24381, 1994.

[76] P. Escudier *et al.*, "JASON system overview and status," *Avis Newsl.*, vol. 7, 2000.

[77] T. Lafon and F. Parisot, "The Jason-1 satellite design and development status," 1998.

[78] Y.-Q. Jin, N. Lu, and M. Lin, "Advancement of Chinese meteorological feng-yun (FY) and oceanic Hai-Yang (HY) satellite remote sensing," *Proc. IEEE*, vol. 98, no. 5, pp. 844–861, May 2010.

[79] J. K. Ridley, W. Cudlip, and S. W. Laxon, "Identification of subglacial lakes using ERS-1 radar altimeter," *J. Glaciol.*, vol. 39, no. 133, pp. 625–634, 1993.

[80] C. R. Francis *et al.*, "The ERS-2 spacecraft and its payload," *ESABu*, vol. 83, pp. 13–31, 1995.

[81] E.-A. S. Européenne, *ENVISAT RA2/MWR Product Handbook. RA2/MWR Products User Guide*, 2007.

[82] B. Legresy, F. Papa, F. Remy, G. Vinay, M. Van den Bosch, and O.-Z. Zanife, "ENVISAT radar altimeter measurements over continental surfaces and ice caps using the ICE-2 retracking algorithm," *Remote Sens. Environ.*, vol. 95, no. 2, pp. 150–163, 2005.

[83] J. Benveniste *et al.*, "The radar altimetry mission: RA-2, MWR, DORIS and LRR," *ESA Bull.*, vol. 106, pp. 25101–25108, 2001.

[84] J. Louet and G. Levrini, "Envisat- Europe's Earth-observation mission for the new millennium," *Earth Obs. Quart.*, no. 60, pp. 1–41, 1998.

[85] L. S. Sørensen, S. B. Simonsen, R. Forsberg, K. Khvorostovsky, R. Meister, and M. E. Engdahl, "25 years of elevation changes of the Greenland Ice sheet from ERS, envisat, and cryosat-2 radar altimetry," *Earth Planet. Sci. Lett.*, vol. 495, pp. 234–241, 2018.

[86] W. Emery and A. Camps, *Introduction to Satellite Remote Sensing: Atmosphere, Ocean, Land and Cryosphere Applications*. Amsterdam, The Netherlands: Elsevier, 2017.

[87] F. Boy, J.-D. Desjonqueres, N. Picot, T. Moreau, and M. Raynal, "CryoSat-2 SAR-mode over oceans: Processing methods, global assessment, and benefits," *IEEE Trans. Geosci. Remote Sens.*, vol. 55, no. 1, pp. 148–158, Jan. 2016.

[88] L. Jiang, R. Schneider, O. B. Andersen, and P. Bauer-Gottwein, "CryoSat-2 altimetry applications over rivers and lakes," *Water*, vol. 9, no. 3, 2017, Art. no. 211.

[89] G. Dibarboure, C. Renaudie, M.-I. Pujol, S. Labroue, and N. Picot, "A demonstration of the potential of Cryosat-2 to contribute to mesoscale observation," *Adv. Space Res.*, vol. 50, no. 8, pp. 1046–1061, 2012.

[90] J. Fernández, C. Fernández, P. Féménias, and H. Peter, "The copernicus Sentinel-3 mission," in *Proc. ILRS Workshop*, 2016, pp. 1–4.

[91] L. A. Brown, J. Dash, A. L. Lidón, E. Lopez-Baeza, and S. Dransfeld, "Synergetic exploitation of the Sentinel-2 missions for validating the sentinel-3 ocean and land color instrument terrestrial chlorophyll index over a vineyard dominated mediterranean environment," *IEEE J. Sel. Topics Appl. Earth Obs. Remote Sens.*, vol. 12, no. 7, pp. 2244–2251, Jul. 2019.

[92] M. L. Hammond, S. A. Henson, N. Lamquin, S. Clerc, and C. Donlon, "Assessing the effect of tandem phase sentinel-3 OLCI sensor uncertainty on the estimation of potential ocean Chlorophyll-a trends," *Remote Sens.*, vol. 12, no. 16, 2020, Art. no. 2522.

[93] A. A. Kokhanovsky, M. Lamare, and V. Rozanov, "Retrieval of the total ozone over Antarctica using sentinel-3 ocean and land colour instrument," *J. Quantitative Spectrosc. Radiative Transfer*, vol. 251, 2020, Art. no. 107045.

[94] M. J. Wooster, W. Xu, and T. Nightingale, "Sentinel-3 SLSTR active fire detection and FRP product: Pre-launch algorithm development and performance evaluation using MODIS and ASTER datasets," *Remote Sens. Environ.*, vol. 120, pp. 236–254, 2012.

[95] T. H. Dixon, M. Naraghi, M. K. McNutt, and S. M. Smith, "Bathymetric prediction from seasat altimeter data," *J. Geophys. Res. Ocean.*, vol. 88, no. C3, pp. 1563–1571, 1983.

[96] W. H. F. Smith, "The marine geoid and satellite altimetry," in *Oceanography From Space*. Berlin, Germany: Springer, 2010, pp. 181–193.

[97] Z. Wang, N. Chao, and D. Chao, "Using satellite altimetry leveling to assess the marine geoid," *Geodesy Geodynamics*, vol. 11, no. 2, pp. 106–111, 2020.

[98] D. T. Sandwell, R. D. Müller, W. H. F. Smith, E. Garcia, and R. Francis, "New global marine gravity model from Cryosat-2 and Jason-1 reveals buried tectonic structure," *Sci. (80-.)*, vol. 346, no. 6205, pp. 65–67, 2014.

[99] S. Zhang and D. T. Sandwell, "Retracking of SARAL/AltiKa radar altimetry waveforms for optimal gravity field recovery," *Geodesy Geodynamics*, vol. 40, no. 1, pp. 40–56, 2017.

[100] L.-L. Fu and R. D. Smith, "Global ocean circulation from satellite altimetry and high-resolution computer simulation," *Bull. Amer. Meteorol. Soc.*, vol. 77, no. 11, pp. 2625–2636, 1996.

[101] R. X. Huang, *Ocean Circulation: Wind-Driven and Thermohaline Processes*. Cambridge, U.K.: Cambridge Univ. Press, 2010.

[102] G. Wang, R. X. Huang, J. Su, and D. Chen, "The effects of thermohaline circulation on wind-driven circulation in the South China Sea," *J. Phys. Oceanogr.*, vol. 42, no. 12, pp. 2283–2296, 2012.

[103] L. Fu and R. E. Cheney, "Application of satellite altimetry to ocean circulation studies: 1987–1994," *Rev. Geophys.*, vol. 33, no. S1, pp. 213–223, 1995.

[104] Y. Xu, J. Li, and S. Dong, "Ocean circulation from altimetry: Progresses and challenges," in *Ocean Circulation and El Nino: New Research*. Hauppauge, NY, USA: Nova Sci. Publishers, 2009.

[105] E. Frajka-Williams, "Estimating the Atlantic overturning at 26 n using satellite altimetry and cable measurements," *Geophys. Res. Lett.*, vol. 42, no. 9, pp. 3458–3464, 2015.

[106] S. Fossette, N. F. Putman, K. J. Lohmann, R. Marsh, and G. C. Hays, "A biologist's guide to assessing ocean currents: A review," *Mar. Ecol. Prog. Ser.*, vol. 457, pp. 285–301, 2012.

[107] C. Le Provost, "Ocean tides," in *International Geophysics*, vol. 69. Amsterdam, The Netherlands: Elsevier, 2001, pp. 267–303.

[108] A. W. Archer, "World's highest tides: Hypertidal coastal systems in North America, South America and Europe," *Sedimentary Geol.*, vol. 284, pp. 1–25, 2013.

[109] G. D. Egbert and R. D. Ray, "Significant dissipation of tidal energy in the deep ocean inferred from satellite altimeter data," *Nature*, vol. 405, no. 6788, pp. 775–778, Jun. 2000, doi: 10.1038/35015531.

[110] T. Mayer-Gürr, R. Savcenko, W. Bosch, I. Daras, F. Flechtner, and C. Dahle, "Ocean tides from satellite altimetry and GRACE," *J. Geodynamics*, vol. 59, pp. 28–38, 2012.

[111] K. Matsumoto, T. Takanezawa, and M. Ooe, "Ocean tide models developed by assimilating TOPEX/POSEIDON altimeter data into hydrodynamical model: A global model and a regional model around Japan," *J. Oceanogr.*, vol. 56, no. 5, pp. 567–581, 2000.

[112] J. Benveniste and N. Picot, "Radar altimetry tutorial," Feb. 2011.

[113] R. D. Ray and D. E. Cartwright, "Estimates of internal tide energy fluxes from topex/poseidon altimetry: Central North Pacific," *Geophys. Res. Lett.*, vol. 28, no. 7, pp. 1259–1262, 2001.

[114] R. W. Owen, "Fronts and eddies in the sea: Mechanisms, interactions and biological effects," *Anal. Mar. Ecosyst.*, pp. 197–233, 1981.

[115] S. Sandven, J. A. Johannessen, K. Kloster, T. Hamre, and H. J. Sætre, "Satellite studies of ocean fronts and eddies for deepwater development in the norwegian sea," in *Proc. 10th Int. Offshore Polar Eng. Conf.*, 2000, pp. 1–11.

[116] K. Dohan and N. Maximenko, "Monitoring ocean currents with satellite sensors," *Oceanography*, vol. 23, no. 4, pp. 94–103, 2010.

[117] V. A. Zinchenko, S. M. Gordeeva, Y. V Sobko, and T. V Belonenko, "Analysis of mesoscale eddies in the Lofoten basin based on satellite altimetry," *Atmospheric Sci.*, vol. 12, no. 3, pp. 46–54, 2019.

[118] C. P. Center, "Frequently asked questions about el niño and la niña," *Nat. Centers Environ. Predict.*, 2005.

[119] M. Ji, R. W. Reynolds, and D. W. Behringer, "Use of TOPEX/Poseidon sea level data for ocean analyses and ENSO prediction: Some early results," *J. Clim.*, vol. 13, no. 1, pp. 216–231, 2000.

[120] A. Cazenave *et al.*, "Estimating ENSO influence on the global mean sea level, 1993–2010," *Mar. Geod.*, vol. 35, pp. 82–97, 2012.

[121] N. Tran, F. Girard-Ardhuin, R. Ezraty, H. Feng, and P. Femenias, "Defining a sea ice flag for envisat altimetry mission," *IEEE Geosci. Remote Sens. Lett.*, vol. 6, no. 1, pp. 77–81, Jan. 2009.

[122] F. Rémy, "The new vision of the cryosphere thanks to 15 years of altimetry," in *Proc. 15 Years Prog. Radar Altimetry Symp.*, 2006, pp. 1–12.

[123] T. Parrinello *et al.*, "CryoSat: ESA's ice mission–eight years in space," *Adv. Space Res.*, vol. 62, no. 6, pp. 1178–1190, 2018.

[124] F. L. Müller, D. Dettmering, W. Bosch, and F. Seitz, "Monitoring the arctic seas: How satellite altimetry can be used to detect openwater in sea-ice regions," *Remote Sens.*, vol. 9, 2017, Art. no. 6, doi: 10.3390/rs9060551.

[125] N. R. Peacock and S. W. Laxon, "Sea surface height determination in the Arctic Ocean from ERS altimetry," *J. Geophys. Res. Ocean.*, vol. 109, 2004, Art. no. C7.

[126] P. Prandi, M. Ablain, A. Cazenave, and N. Picot, "A new estimation of mean sea level in the Arctic Ocean from satellite altimetry," *Mar. Geodesy*, vol. 35, pp. 61–81, 2012.

[127] Y. Cheng, O. Andersen, and P. Knudsen, "An improved 20-year Arctic Ocean Altimetric sea level data record," *Mar. Geodesy*, vol. 38, no. 2, pp. 146–162, 2015.

[128] O. B. Andersen and G. Piccioni, "Recent Arctic sea level variations from satellites," *Front. Mar. Sci.*, vol. 3, 2016, Art. no. 76.

[129] T. W. K. Armitage, S. Bacon, A. L. Ridout, S. F. Thomas, Y. Aksenov, and D. J. Wingham, "Arctic sea surface height variability and change from satellite radar altimetry and GRACE, 2003–2014," *J. Geophys. Res. Ocean.*, vol. 121, no. 6, pp. 4303–4322, 2016.

[130] S. Levitus, J. Antonov, and T. Boyer, "Warming of the world ocean, 1955–2003," *Geophys. Res. Lett.*, vol. 32, 2005, Art. no. 2.

[131] J. P. Abraham *et al.*, "A review of global ocean temperature observations: Implications for ocean heat content estimates and climate change," *Rev. Geophys.*, vol. 51, no. 3, pp. 450–483, 2013.

[132] S. C. Doney *et al.*, "Climate change impacts on marine ecosystems," *Ann. Rev. Mar. Sci.*, vol. 4, pp. 11–37, 2012.

[133] W. W. V. Sweet *et al.*, "Global and regional sea level rise scenarios for the United States," Tech. Rep. NOS CO-OPS 083, National Oceanic and Atmospheric Administration, Silver Spring, Maryland, 2017.

[134] R. S. Nerem, B. D. Beckley, J. T. Fasullo, B. D. Hamlington, D. Masters, and G. T. Mitchum, "Climate-change–driven accelerated sea-level rise detected in the altimeter era," *Proc. Nat. Acad. Sci., USA*, vol. 115, no. 9, pp. 2022–2025, 2018.

[135] A. A. Mouche, D. Hauser, and V. Kudryavtsev, "Radar scattering of the ocean surface and sea-roughness properties: A combined analysis from dual-polarizations airborne radar observations and models in C band," *J. Geophys. Res. Ocean.*, vol. 111, 2006, Art. no. C9.

[136] T. Lo, H. Leung, J. Litva, and S. Haykin, "Fractal characterisation of sea-scattered signals and detection of sea-surface targets," *IEE Proc. F (Radar Signal Process.)*, vol. 140, no. 4, pp. 243–250, Aug. 1993.

[137] Y. Jia, P. Chu, C. K. Shum, and J. Park, "Retrieval of wind speed measurements over the great lakes using satellite radar altimetry," *AGUFM*, vol. 2019, pp. H31N–H31N–1938, 2019.

[138] A. Ribal and I. R. Young, "33 years of globally calibrated wave height and wind speed data based on altimeter observations," *Sci. data*, vol. 6, no. 1, pp. 1–15, 2019.

[139] Z. Hao, Q. Tu, S. Zhang, J. Chen, and D. Pan, "Wind-Wave relationship model and analysis of typhoon wave fields in the south China sea from HY-2A Satellite observations," *IEEE J. Sel. Topics Appl. Earth Obs. Remote Sens.*, vol. 13, pp. 4008–4015, Jul. 2020.

[140] M. Eshagh, "A strategy towards an EGM08-based Fennoscandian geoid model," *J. Appl. Geophys.*, vol. 87, pp. 53–59, 2012, doi: 10.1016/j.jappgeo.2012.08.008.

[141] M. Eshagh, "Numerical aspects of EGM08-based geoid computations in Fennoscandia regarding the applied reference surface and error propagation," *J. Appl. Geophys.*, vol. 96, pp. 28–32, 2013, doi: 10.1016/j.jappgeo.2013.06.011.

[142] P. Visser, "Gravity field determination with GOCE and GRACE," *Adv. Sp. Res.*, vol. 23, no. 4, pp. 771–776, 1999.

[143] S.-C. Han, "Efficient determination of global gravity field from Satellite-to-satellite tracking mission," *Celestial Mech. Dyn. Astron.*, vol. 88, no. 1, pp. 69–102, 2004, doi: 10.1023/b:cele.0000009383.07092.1f.

[144] M. Unwin *et al.*, "GNSS enabling new capabilities in space on the techdemosat-1 satellite," in *Proc. 30th Int. Tech. Meeting Satell. Division Inst. Navigation*, 2017, pp. 4066–4079, doi: 10.33012/2017.15349.

[145] B. D. Hamlington *et al.*, "Origin of interannual variability in global mean sea level," *Proc. Nat. Acad. Sci., USA*, vol. 117, no. 25, pp. 13983–13990, 2020, doi: 10.1073/pnas.1922190117.

[146] B. D. Tapley, S. Bettadpur, J. C. Ries, P. F. Thompson, and M. M. Watkins, "GRACE measurements of mass variability in the Earth system," *Sci. (80-.)*, vol. 305, no. 5683, pp. 503–505, 2004.

[147] M. Wolff, "Direct measurements of the Earth's gravitational potential using a satellite pair," *J. Geophys. Res.*, vol. 74, no. 22, pp. 5295–5300, 1969, doi: 10.1029/jb074i022p05295.

[148] J. K. Makowski, D. P. Chambers, and J. A. Bonin, "Using ocean bottom pressure from the gravity recovery and climate experiment (GRACE) to estimate transport variability in the southern I ndian O cean," *J. Geophys. Res. Ocean.*, vol. 120, no. 6, pp. 4245–4259, 2015, doi: 10.1002/2014jc010575.

[149] P. E. Land *et al.*, "Salinity from space unlocks satellite-based assessment of ocean acidification," *Environ. Sci. Technol.*, vol. 49, no. 4, pp. 1987–1994, 2015, doi: 10.1021/es504849s.

[150] B. D. Tapley *et al.*, "Contributions of GRACE to understanding climate change," *Nat. Clim. Chang.*, vol. 9, no. 5, pp. 358–369, 2019, doi: 10.1038/s41558-019-0456-2.

[151] A. Blazquez, B. Meyssignac, J. M. Lemoine, E. Berthier, A. Ribes, and A. Cazenave, "Exploring the uncertainty in GRACE estimates of the mass redistributions at the Earth surface: Implications for the global water and sea level budgets," *Geophys. J. Int.*, vol. 215, no. 1, pp. 415–430, 2018, doi: 10.1093/gji/ggy293.

[152] T. Jeon, K.-W. Seo, K. Youm, J. Chen, and C. R. Wilson, "Global sea level change signatures observed by GRACE satellite gravimetry," *Sci. Rep.*, vol. 8, no. 1, pp. 1–10, 2018.

[153] D. Mu, H. Yan, W. Feng, and P. Peng, "GRACE leakage error correction with regularization technique: Case studies in Greenland and Antarctica," *Geophys. J. Int.*, vol. 208, pp. 1775–1786, 2017, doi: 10.1093/gji/ggw494.

[154] O. Baur, M. Kuhn, and W. E. Featherstone, "GRACE-derived ice-mass variations over Greenland by accounting for leakage effects," *J. Geophys. Res.*, vol. 114, 2009, Art. no. B6, doi: 10.1029/2008jb006239.

[155] S. Yi and K. Heki, "Heterogeneous oceanic mass distribution in GRACE observations and its leakage effect," *Geophys. J. Int.*, vol. 221, no. 1, pp. 603–616, 2020, doi: 10.1093/gji/ggaa022.

[156] K. J. Quinn and R. M. Ponte, "Uncertainty in ocean mass trends from GRACE," *Geophys. J. Int.*, vol. 181, pp. 762–768, 2010, doi: 10.1111/j.1365-246x.2010.04508.x.

[157] B. D. Tapley, S. Bettadpur, M. Watkins, and C. Reigber, "The gravity recovery and climate experiment: Mission overview and early results," *Geophys. Res. Lett.*, vol. 31, 2004, Art. no. 9, doi: 10.1029/2004gl019920.

[158] X. Wang and P. Li, "Extraction of earthquake-induced collapsed buildings using very high-resolution imagery and airborne lidar data," *Int. J. Remote Sens.*, vol. 36, no. 8, pp. 2163–2183, Apr. 2015, doi: 10.1080/01431161.2015.1034890.

[159] J.-C. Juang, Y.-F. Tsai, and C.-T. Lin, "FORMOSAT-7R mission for GNSS reflectometry," in *Proc. IEEE Int. Geosci. Remote Sens. Symp.*, 2019, pp. 5177–5180, doi: 10.1109/igarss.2019.8900130.

[160] E. Guascal, S. Rojas, E. Kirby, T. Toulkeridis, W. Fuertes, and M. Heredia, "Application of remote sensing techniques in the estimation of forest biomass of a recreation area by UAV and RADAR images in Ecuador," in *Proc. 7th Int. Conf. eDemocracy eGovernment*, Apr. 2020, pp. 183–190, doi: 10.1109/ICEDEG48599.2020.9096880.

[161] B. R. Scanlon *et al.*, "Global evaluation of new GRACE mascon products for hydrologic applications," *Water Resour. Res.*, vol. 52, no. 12, pp. 9412–9429, 2016, doi: 10.1002/2016wr019494.

[162] D. Mu, T. Xu, and G. Xu, "Detecting coastal ocean mass variations with GRACE mascons," *Geophys. J. Int.*, vol. 217, no. 3, pp. 2071–2080, 2019, doi: 10.1093/gji/ggz138.

[163] Z. Kang, S. Bettadpur, P. Nagel, H. Save, S. Poole, and N. Pie, "GRACE-FO precise orbit determination and gravity recovery," *J. Geod.*, vol. 94, 2020, Art. no. 9, doi: 10.1007/s00190-020-01414-3.

[164] F. W. Landerer *et al.*, "Extending the global mass change data record: GRACE follow-on instrument and science data performance," *Geophys. Res. Lett.*, vol. 47, no. 12, 2020, Art. no. e2020GL088306, doi: 10.1029/2020gl088306.

[165] J. Wahr, M. Molenaar, and F. Bryan, "Time variability of the Earth's gravity field: Hydrological and oceanic effects and their possible detection using GRACE," *J. Geophys. Res. Solid Earth*, vol. 103, no. B12, pp. 30205–30229, 1998, doi: 10.1029/98jb02844.

[166] D. Long *et al.*, "Have GRACE satellites overestimated groundwater depletion in the northwest India aquifer?," *Sci. Rep.*, vol. 6, no. 1, 2016, Art. no. 24398, doi: 10.1038/srep24398.

[167] X. Chen, D. Long, Y. Hong, C. Zeng, and D. Yan, "Improved modeling of snow and glacier melting by a progressive two-stage calibration strategy with GRACE and multisource data: How snow and glacier meltwater contributes to the runoff of the upper Brahmaputra river basin?," *Water Resour. Res.*, vol. 53, no. 3, pp. 2431–2466, 2017, doi: 10.1002/2016wr019656.

[168] Z. Sun, X. Zhu, Y. Pan, and J. Zhang, "Assessing terrestrial water storage and flood potential using GRACE data in the Yangtze river Basin, China," *Remote Sens,* vol. 9, no. 10, 2017, Art. no. 1011, doi: 10.3390/rs9101011.

[169] B. Li *et al.*, "Global GRACE data assimilation for groundwater and drought monitoring: Advances and challenges," *Water Resour. Res.*, vol. 55, no. 9, pp. 7564–7586, 2019.

[170] Z. Sun, D. Long, W. Yang, X. Li, and Y. Pan, "Reconstruction of GRACE data on changes in total water storage over the global land surface and 60 basins," *Water Resour. Res.*, vol. 56, no. 4, 2020, Art. no. e2019WR026250, doi: 10.1029/2019wr026250.

[171] C. Boening, T. Lee, and V. Zlotnicki, "A record-high ocean bottom pressure in the south pacific observed by GRACE," *Geophys. Res. Lett.*, vol. 38, no. 4, 2011, Art. no. 4, doi: 10.1029/2010gl046013.

[172] A. Androsov, O. Boebel, J. Schröter, S. Danilov, A. Macrander, and I. Ivanciu, "Ocean bottom pressure variability: Can it be reliably modeled?," *J. Geophys. Res. Ocean.*, vol. 125, no. 3, pp. 1–19, 2020, doi: 10.1029/2019jc015469.

[173] D. P. Chambers, J. Wahr, and R. S. Nerem, "Preliminary observations of global ocean mass variations with GRACE," *Geophys. Res. Lett.*, vol. 31, 2004, Art. no. 13, doi: 10.1029/2004gl020461.

[174] J. M. Wahr, S. R. Jayne, and F. O. Bryan, "A method of inferring changes in deep ocean currents from satellite measurements of time-variable gravity," *J. Geophys. Res. Ocean.*, vol. 107, no. C12, pp. 11–17, 2002, doi: 10.1029/2001jc001274.

[175] J.-R. Liau and B. F. Chao, "Variation of Antarctic circumpolar current and its intensification in relation to the southern annular mode detected in the time-variable gravity signals by GRACE satellite," *Earth, Planets Space*, vol. 69, no. 1, 2017, Art. no. 93, doi: 10.1186/s40623-017-0678-3.

[176] V. Zlotnicki, J. Wahr, I. Fukumori, and Y. T. Song, "Antarctic circumpolar current transport variability during 2003–05 from GRACE," *J. Phys. Oceanogr.*, vol. 37, no. 2, pp. 230–244, 2007, doi: 10.1175/jpo3009.1.

[177] S. Jin, "Satellite gravimetry: Mass transport and redistribution in the Earth system," *Geodetic Sci. - Observ., Model. Appl.*, vol. 10, pp. 402–415, 2013, doi: 10.5772/51698.

[178] C.-W. Hsu and I. Velicogna, "Detection of sea level fingerprints derived from GRACE gravity data," *Geophys. Res. Lett.*, vol. 44, no. 17, pp. 8953–8961, 2017, doi: 10.1002/2017gl074070.

[179] D. P. Chambers, "Observing seasonal steric sea level variations with GRACE and satellite altimetry," *J. Geophys. Res.*, vol. 111, 2006, Art. no. C3, doi: 10.1029/2005jc002914.

[180] D. García, G. Ramillien, A. Lombard, and A. Cazenave, "Steric Sea-level variations inferred from combined topex/poseidon altimetry and GRACE gravimetry," *Pure Appl. Geophys.*, vol. 164, no. 4, pp. 721–731, 2007, doi: 10.1007/s00024-007-0182-y.

[181] D. P. Chambers *et al.*, "Evaluation of the global mean sea level budget between 1993 and 2014," *Surv. Geophys.*, vol. 38, no. 1, pp. 309–327, 2016, doi: 10.1007/s10712-016-9381-3.

[182] F. Fatolazadeh, B. Voosoghi, and M. Raoofian Naeeni, "Correction of hydrological and oceanic effects from GRACE data by combination of the Steric sea level, altimetry data and GLDAS model," *Acta Geophys.*, vol. 64, no. 4, pp. 1193–1210, 2016, doi: 10.1515/acgeo-2016-0034.

[183] A. Lombard *et al.*, "Estimation of steric sea level variations from combined GRACE and Jason-1 data," *Earth Planet. Sci. Lett.*, vol. 254, no. 1/2, pp. 194–202, 2007, doi: 10.1016/j.epsl.2006.11.035.

[184] W. Feng and M. Zhong, "Global sea level variations from altimetry, GRACE and argo data over 2005–2014," *Geod. Geodyn.*, vol. 6, no. 4, pp. 274–279, 2015, doi: 10.1016/j.geog.2015.07.001.

[185] H. Amin, M. Bagherbandi, and L. E. Sjöberg, "Quantifying barystatic sea-level change from satellite altimetry, GRACE and Argo observations over 2005–2016," *Adv. Space Res.*, vol. 65, no. 8, pp. 1922–1940, 2020, doi: 10.1016/j.asr.2020.01.029.

[186] S. R. Jayne, J. M. Wahr, and F. O. Bryan, "Observing ocean heat content using satellite gravity and altimetry," *J. Geophys. Res. Ocean.*, vol. 108, 2003, Art. no. C2, doi: 10.1029/2002jc001619.

[187] M. E. Shokr, *Radar Remote Sensing Applications in Egypt*. Cham, Switzerland: Springer, 2020, pp. 127–166.

[188] R. Manavalan, "Review of synthetic aperture radar frequency, polarization, and incidence angle data for mapping the inundated regions," *J. Appl. Remote Sens.*, vol. 12, no. 2, May 2018, Art. no. 1, doi: 10.1117/1.jrs.12.021501.

[189] F. T. Charbonneau *et al.*, "Compact polarimetry overview and applications assessment," *Can. J. Remote Sens.*, vol. 36, pp. S298–S315, Jan. 2010, doi: 10.5589/m10-062.

[190] J. A. Richards, "The imaging radar system." *Remote Sens. with Imag. Radar*. Berlin, Heidelberg: Springer, pp. 1–10, 2009.

[191] Z. Perski, "Application of SAR imagery and SAR interferometry in digital geological cartography," in *The Current Role of Geological Mapping in Geosciences*. Berlin, Germany: Springer, 2006, pp. 225–244.

[192] R. Torres *et al.*, "GMES Sentinel-1 mission," *Remote Sens. Environ.*, vol. 120, pp. 9–24, May 2012, doi: 10.1016/j.rse.2011.05.028.

[193] C. H. Beisl, F. P. Miranda, and C. L. Silva, "Combined use of RADARSAT-1 and AVHRR data for the identification of mesoscale oceanic features in the Campos Basin, Brazil," in *Proc. 6th Int. Conf. Remote Sens. Mar. Coastal Environments*, 2000, pp. 1–3.

[194] H. Fang, W. Perrie, G. Fan, T. Xie, and J. Yang, "Ocean surface wind speed retrieval from C-band quad-polarized SAR measurements at optimal spatial resolution," *Remote Sens. Lett.*, vol. 12, no. 2, pp. 155–164, 2021, doi: 10.1080/2150704X.2020.1846220.

[195] O. Isoguchi and M. Shimada, "Extraction of ocean wave parameters by ALOS/PALSAR," in *Proc. 3rd Int. Asia-Pacific Conf. Synthetic Aperture Radar*, 2011, pp. 1–4.

[196] S. K. Palanisamy Vadivel, D. Kim, J. Jung, Y.-K. Cho, and K.-J. Han, "Monitoring the vertical land motion of tide gauges and its impact on relative sea level changes in Korean Peninsula using sequential SBAS-InSAR time-series analysis," *Remote Sens.*, vol. 13, no. 1, 2021, Art. no. 18.

[197] G. Anfuso, M. Postacchini, D. Di Luccio, and G. Benassai, "Coastal sensitivity/vulnerability characterization and adaptation strategies: A review," *J. Mar. Sci. Eng.*, vol. 9, no. 1, 2021, Art. no. 72.

[198] Y. Wan, X. Shi, Y. Dai, L. Li, X. Qu, and X. Zhang, "Research on wind speed inversion method for X-Band networked SAR satellite," *J. Mar. Sci. Eng.*, vol. 8, no. 9, 2020, Art. no. 626.

[199] K. B. Katsaros, P. W. Vachon, P. G. Black, P. P. Dodge, and E. W. Uhlhorn, "Wind fields from SAR: Could they improve our understanding of storm dynamics?," *Johns Hopkins APL Tech. Dig.*, vol. 21, no. 1, pp. 86–93, 2000.

[200] H. Lin, Q. Xu, and Q. Zheng, "Overview on SAR measurements of sea surface wind," *Prog. Natural Sci.*, vol. 18, no. 8, pp. 913–919, Aug. 2008, doi: 10.1016/j.pnsc.2008.03.008.

[201] A. Corazza, A. Khenchaf, and F. Comblet, "Assessment of wind direction estimation methods from SAR images," *Remote Sens,* vol. 12, no. 21, 2020, Art. no. 3631.

[202] N. Radkani and B. G. Zakeri, "Southern Caspian Sea wind speed retrieval from C-band Sentinel-1A SAR images," *Int. J. Remote Sens.*, vol. 41, no. 9, pp. 3511–3534, May 2020, doi: 10.1080/01431161.2019.1706201.

[203] Y. Lu, B. Zhang, W. Perrie, A. Mouche, and G. Zhang, "CMODH validation for C-Band synthetic aperture radar HH polarization wind retrieval over the ocean," *IEEE Geosci. Remote Sens. Lett.*, vol. 18, no. 1, pp. 102–106, Jan. 2021, doi: 10.1109/lgrs.2020.2967811.

[204] A. G. Marshall, M. A. Hemer, H. H. Hendon, and K. L. McInnes, "Southern annular mode impacts on global ocean surface waves," *Ocean Model.*, vol. 129, pp. 58–74, Sep. 2018, doi: 10.1016/j.ocemod.2018.07.007.

[205] G. Festa, "Interaction between surface waves and absorbing boundaries for wave propagation in geological basins: 2D numerical simulations," *Geophys. Res. Lett.*, vol. 32, no. 20, Oct. 2005, Art. no. L20306, doi: 10.1029/2005GL024091.

[206] J. B. Zirker, *The Science of Ocean Waves: Ripples, Tsunamis, and Stormy Seas*. Baltimore, ML, USA: JHU Press, 2013.

[207] B. Huang and X. -M. Li, "Spaceborne SAR wave mode data as big data for global ocean wave observation," *EUSAR 13th Euro. Conf. Synthetic Aperture Radar*, pp. 1–6, 2021.

[208] Y. Zhang, Y. Wang, and Q. Xu, "On the nonlinear mapping of an ocean wave spectrum into a new polarimetric SAR image spectrum," *J. Phys. Oceanogr.*, vol. 50, no. 11, pp. 3109–3122, Nov. 2020, doi: 10.1175/JPO-D-20-0045.1.

[209] X. Liu, Q. Yang, S. Wang, and Y. Zhou, "Retrieval of ocean wave parameters using envisat advanced synthetic aperture radar data and its verification analysis," *J. Phys., Conf. Ser.*, vol. 1631, no. 1, Sep. 2020, Art. no. 12129, doi: 10.1088/1742-6596/1631/1/012129.

[210] S. A. Phaniharam, V. Chintam, G. Baggu, and V. S. R. P. Koneru, "Study of internal wave characteristics off northwest Bay of Bengal using synthetic aperture radar," *Nat. Hazards*, vol. 104, pp. 2451–2460, Sep. 2020, doi: 10.1007/s11069-020-04280-6.

[211] C. Guo, V. Vlasenko, W. Alpers, N. Stashchuk, and X. Chen, "Evidence of short internal waves trailing strong internal solitary waves in the northern South China Sea from synthetic aperture radar observations," *Remote Sens. Environ.*, vol. 124, pp. 542–550, Sep. 2012, doi: 10.1016/j.rse.2012.06.001.

[212] X. Bai and C. Xu, "Internal solitary waves in the northeastern South China Sea," in *Regional Oceanography of the South China Sea*. Singapore: World Scientific, 2020, pp. 403–432.

[213] M. H. Alford *et al.*, "The formation and fate of internal waves in the South China Sea," *Nature*, vol. 521, no. 7550, pp. 65–69, May 2015, doi: 10.1038/nature14399.

[214] A. F. Waterhouse *et al.*, "Global patterns of diapycnal mixing from measurements of the turbulent dissipation rate," *J. Phys. Oceanogr.*, vol. 44, no. 7, pp. 1854–1872, Jul. 2014, doi: 10.1175/JPO-D-13-0104.1.

[215] D. Li *et al.*, "Elevated particulate organic carbon export flux induced by internal waves in the oligotrophic northern South China Sea," *Sci. Rep.*, vol. 8, no. 1, Dec. 2018, Art. no. 2042, doi: 10.1038/s41598-018-20184-9.

[216] H. Zhang, J. Meng, L. Sun, X. Zhang, and S. Shu, "Performance analysis of internal solitary wave detection and identification based on compact polarimetric SAR," *IEEE Access*, vol. 8, pp. 172839–172847, Sep. 2020, doi: 10.1109/access.2020.3025946.

[217] J. Ning, L. Sun, H. Cui, K. Lu, and J. Wang, "Study on characteristics of internal solitary waves in the Malacca Strait based on Sentinel-1 and GF-3 satellite SAR data," *Acta Oceanol. Sinica*, vol. 39, no. 5, pp. 151–156, May 2020, doi: 10.1007/s13131-020-1604-2.

[218] Y. Ji, J. Zhang, X. Chu, Y. Wang, and L. Yang, "Ocean surface current measurement with high-frequency hybrid sky–surface wave radar," *Remote Sens. Lett.*, vol. 8, no. 7, pp. 617–626, Jul. 2017, doi: 10.1080/2150704X.2017.1306138.

[219] M. Rani, M. Masroor, and P. Kumar, "Remote sensing of Ocean and coastal environment – overview," in *Remote Sensing of Ocean and Coastal Environments*. Amsterdam, The Netherlands: Elsevier, 2021, pp. 1–15.

[220] I. E. Kozlov and E. V Plotnikov, "Dynamics of eddies in the arctic ocean from quasi-synchronous Sentinel-1 SAR observations," *Sovremennye Problemy Distantsionnogo Zondirovaniya Zemli iz kosmosa*, vol. 17, no. 3, pp. 178–186, 2020, doi: 10.21046/2070-7401-2020-17-3-178-186.

[221] B. Liu, Y. He, and X. Li, "A new concept of full ocean current vector retrieval with spaceborne SAR based on intrapulse beam-switching technique," *IEEE Trans. Geosci. Remote Sens.*, vol. 58, no. 11, pp. 7682–7704, Nov. 2020, doi: 10.1109/tgrs.2020.2983178.

[222] K. Seenipandi, K. K. Ramachandran, and P. Kumar, "Ocean remote sensing for spatiotemporal variability of wave energy density and littoral current velocity in the Southern Indian offshore," in *Remote Sensing of Ocean and Coastal Environments*. Amsterdam, The Netherlands: Elsevier, 2021, pp. 47–63.

[223] M. DeGrandpre, W. Evans, M.-L. Timmermans, R. Krishfield, B. Williams, and M. Steele, "Changes in the arctic ocean carbon cycle with diminishing ice cover," *Geophys. Res. Lett.*, vol. 47, no. 12, 2020, Art. no. e2020GL088051.

[224] B. Scheuchl, D. Flett, R. Caves, and I. Cumming, "Potential of RADARSAT-2 data for operational sea ice monitoring," *Can. J. Remote Sens.*, vol. 30, no. 3, pp. 448–461, 2004, doi: 10.5589/m04-011.

[225] N. Zakhvatkina, V. Smirnov, and I. Bychkova, "Satellite SAR Data-based sea ice classification: An overview," *Geosciences*, vol. 9, no. 4, Mar. 2019, Art. no. 152, doi: 10.3390/geosciences9040152.

[226] T. Xie, W. Perrie, C. Wei, and L. Zhao, "Discrimination of open water from sea ice in the Labrador Sea using quad-polarized synthetic aperture radar," *Remote Sens. Environ.*, vol. 247, Sep. 2020, Art. no. 111948, doi: 10.1016/j.rse.2020.111948.

[227] K. Blix, M. M. Espeseth, and T. Eltoft, "Machine learning for Arctic sea ice physical properties estimation using dual-polarimetric SAR data," *IEEE Trans. Geosci. Remote Sens.*, vol. 59, no. 6, pp. 4618–4634, Jun. 2021, doi: 10.1109/tgrs.2020.3022461.

[228] J. C. Iacarella, L. Burke, I. C. Davidson, C. DiBacco, T. W. Therriault, and A. Dunham, "Unwanted networks: Vessel traffic heightens the risk of invasions in marine protected areas," *Biol. Conservation*, vol. 245, May 2020, Art. no. 108553, doi: 10.1016/j.biocon.2020.108553.

[229] M. Fingas and C. Brown, "A review of oil spill remote sensing," *Sensors*, vol. 18, no. 2, Dec. 2017, Art. no. 91, doi: 10.3390/s18010091.

[230] S. T. Seydi, M. Hasanlou, M. Amani, and W. Huang, "Oil spill detection based on multiscale multidimensional residual CNN for optical remote sensing imagery," *IEEE J. Sel. Topics Appl. Earth Obs. Remote Sens.*, vol. 14, pp. 10941–10952, Oct. 2021, doi: 10.1109/JS-TARS.2021.3123163.

[231] A. Bonnington, M. Amani, and H. Ebrahimy, "Oil spill detection using satellite imagery," *Adv. Environ. Eng. Res.*, vol. 2, no. 4, Aug. 2021, doi: 10.21926/aeer.2104024.

[232] J. F. Piatt and R. G. Ford, "How many seabirds were killed by the erron valdez oil spill?," in *Proc. Amer. Fisheries Soc. Symp.*, 1996, vol. 18, pp. 712–719.

[233] B. L. Chilvers, K. J. Morgan, and B. J. White, "Sources and reporting of oil spills and impacts on wildlife 1970–2018," *Environ. Sci. Pollut. Res.*, vol. 28, pp. 754–762, Aug. 2020, doi: 10.1007/s11356-020-10538-0.

[234] J. C. Haney, P. G. R. Jodice, W. A. Montevecchi, and D. C. Evers, "Challenges to oil spill assessment for seabirds in the deep ocean," *Arch. Environ. Contamination Toxicology*, vol. 73, no. 1, pp. 33–39, Jul. 2017, doi: 10.1007/s00244-016-0355-8.

[235] A. E. Burger and D. M. Fry, "Effects of oil pollution on seabirds in the northeast Pacific," in *Proc. Pacific Seabird Group*, 1993, pp. 254–263.

[236] P. Marzialetti and G. Laneve, "Oil spill monitoring on water surfaces by radar L, C and x band SAR imagery: A comparison of relevant characteristics," in *Proc. Int. Geosci. Remote Sens. Symp.*, Nov. 2016, vol. 2016-Novem, pp. 7715–7717, doi: 10.1109/IGARSS.2016.7731012.

[237] K. Zeng and Y. Wang, "A deep convolutional neural network for oil spill detection from Spaceborne SAR images," *Remote Sens.*, vol. 12, no. 6, 2020, Art. no. 1015.

[238] K.-A. Park and J.-J. Park, "Accuracy and error characteristics of SMOS Sea surface salinity in the Seas around Korea," *J. Korean Earth Sci. Soc.*, vol. 41, no. 4, pp. 356–366, Aug. 2020, doi: 10.5467/jkess.2020.41.4.356.

[239] R. Gens, "Oceanographic applications of SAR remote sensing," *GISci. Remote Sens.*, vol. 45, no. 3, pp. 275–305, Jul. 2008, doi: 10.2747/1548-1603.45.3.275.

[240] O. Karakuş, I. Rizaev, and A. Achim, "Ship wake detection in SAR images via sparse regularisation," in *IEEE Trans. Geosci. Remote Sens.*, vol. 58, no. 3, pp. 1665–1677, Mar. 2020, doi: 10.1109/TGRS.2019.2947360.

[241] O. Karakus and A. Achim, "Ship wake detection in X-band SAR images using sparse GMC regularization," in *Proc. IEEE Int. Conf. Acoust., Speech Signal Process.*, May 2019, pp. 2182–2186, doi: 10.1109/ICASSP.2019.8683489.

[242] M. D. Graziano, M. D'Errico, and G. Rufino, "Ship heading and velocity analysis by wake detection in SAR images," *Acta Astronaut.*, vol. 128, pp. 72–82, Nov. 2016, doi: 10.1016/j.actaastro.2016.07.001.

[243] S. Calmant, M. Berge-Nguyen, and A. Cazenave, "Global seafloor topography from a least-squares inversion of altimetry-based high-resolution mean sea surface and shipboard soundings," *Geophys. J. Int.*, vol. 151, no. 3, pp. 795–808, Dec. 2002, doi: 10.1046/j.1365-246X.2002.01802.x.

[244] S. Gille, J. Metzger, and R. Tokmakian, "Seafloor topography and ocean circulation," *Oceanography*, vol. 17, no. 1, pp. 47–54, Mar. 2004, doi: 10.5670/oceanog.2004.66.

[245] A. A. Kurekin, P. E. Land, and P. I. Miller, "Internal waves at the U.K. continental shelf: Automatic mapping using the ENVISAT ASAR sensor," *Remote Sens.*, vol. 12, no. 15, 2020, Art. no. 2476.

[246] W. Alpers, G. Campbell, H. Wensink, and Q. Zhang, "Underwater topography," in *Synthesis Aperture Radar Marine User's Manual*, 2004, pp. 245–262.

[247] S. Wiehle, A. Pleskachevsky, and C. Gebhardt, "Automatic bathymetry retrieval from SAR images," *CEAS Space J.*, vol. 11, no. 1, pp. 105–114, Mar. 2019, doi: 10.1007/s12567-018-0234-4.

[248] X. Bian, Y. Shao, C. Zhang, C. Xie, and W. Tian, "The feasibility of assessing swell-based bathymetry using SAR imagery from orbiting satellites," *ISPRS J. Photogrammetry Remote Sens.*, vol. 168, pp. 124–130, Oct. 2020, doi: 10.1016/j.isprsjprs.2020.08.006.

[249] L. Lacour, R. Larouche, and M. Babin, "In situ evaluation of spaceborne CALIOP lidar measurements of the upper-ocean particle backscattering coefficient," *Opt. Exp.*, vol. 28, no. 18, 2020, Art. no. 26989, doi: 10.1364/oe.397126.

[250] C. Jamet *et al.*, "Going beyond standard ocean color observations : Lidar and polarimetry," *Frontiers Marine Sci.*, vol. 6, p. 251, 2019.

[251] P. Chen and D. Pan, "Ocean optical profiling in South China Sea using airborne LiDAR," *Remote Sens.*, vol. 11, no. 15, 2019, Art. no. 1826, doi: 10.3390/rs11151826.

[252] D. Dionisi, V. E. Brando, G. Volpe, S. Colella, and R. Santoleri, "Seasonal distributions of ocean particulate optical properties from spaceborne lidar measurements in Mediterranean and Black sea," *Remote Sens. Environ.*, vol. 247, 2020, Art. no. 111889, doi: 10.1016/j.rse.2020.111889.

[253] B. L. Collister, R. C. Zimmerman, C. I. Sukenik, V. J. Hill, and W. M. Balch, "Remote sensing of optical characteristics and particle distributions of the upper ocean using shipboard lidar," *Remote Sens. Environ.*, vol. 215, pp. 85–96, 2018, doi: 10.1016/j.rse.2018.05.032.

[254] R. Barbini, F. Colao, R. Fantoni, L. Fiorani, N. V Kolodnikova, and A. Palucci, "Laser remote sensing calibration of ocean color satellite data," *Geophys*, vol. 49, pp. 35–43, 2006.

[255] S. Chen, C. Xue, T. Zhang, L. Hu, G. Chen, and J. Tang, "Analysis of the optimal wavelength for oceanographic lidar at the global scale based on the inherent optical properties ofwater," *Remote Sens.*, vol. 11, no. 22, 2019, doi: 10.3390/rs11222705.

[256] D. Liu *et al.*, "Lidar remote sensing of seawater optical properties: Experiment and Monte Carlo simulation," *IEEE Trans. Geosci. Remote Sens.*, vol. 57, no. 11, pp. 9489–9498, Nov. 2019, doi: 10.1109/TGRS.2019.2926891.

[257] H. Liu, P. Chen, Z. Mao, D. Pan, and Y. He, "Subsurface plankton layers observed from airborne lidar in Sanya Bay, South China Sea," *Opt. Exp.*, vol. 3, no. 22, 2018, Art. no. 29134, doi: 10.1364/oe.26.029134.

[258] J. Hair *et al.*, "Combined atmospheric and ocean profiling from an airborne high spectral resolution lidar," *EPJ Web Conf.*, vol. 119, pp. 1–4, 2016, doi: 10.1051/epjconf/201611922001.

[259] M. J. Behrenfeld *et al.*, "Space-based lidar measurements of global ocean carbon stocks," *Geophys. Res. Lett.*, vol. 40, no. 16, pp. 4355–4360, 2013, doi: 10.1002/grl.50816.

[260] J. A. Schulien, M. J. Behrenfeld, J. W. Hair, C. A. Hostetler, and M. S. Twardowski, "Vertically- resolved phytoplankton carbon and net primary production from a high spectral resolution lidar," *Opt. Exp.*, vol. 25, no. 12, 2017, Art. no. 13577, doi: 10.1364/oe.25.013577.

[261] A. Yang *et al.*, "Filtering of airborne LiDAR bathymetry based on bidirectional cloth simulation," *ISPRS J. Photogrammetry Remote Sens.*, vol. 163, pp. 49–61, 2020, doi: 10.1016/j.isprsjprs.2020.03.004.

[262] J. H. Churnside, "Review of profiling oceanographic lidar," *Opt. Eng.*, vol. 53, no. 5, Apr. 2014, doi: 10.1117/1.OE.53.5.051405.

[263] D. Liu *et al.*, "High-spectral-resolution lidar for ocean ecosystem studies," *Laser Radar Technol. Appl. XXI*, vol. 9832, 2016, Art. no. 983214, doi: 10.1117/12.2224488.

[264] J. H. Churnside, R. D. Marchbanks, C. Lembke, and J. Beckler, "Optical backscattering measured by airborne lidar and underwater glider," *Remote Sens.*, vol. 9, no. 4, pp. 1–12, 2017, doi: 10.3390/rs9040379.

[265] C. A. Hostetler, M. J. Behrenfeld, Y. Hu, J. W. Hair, and J. A. Schulien, "Spaceborne lidar in the study of marine systems," *Annu. Rev. Mar. Sci.*, vol. 10, pp. 121–147, 2018.

[266] J. E. Vonk, "Ocean subsurface studies with the CALIPSO spaceborne lidar," *J. Geophys. Res. Ocean.*, vol. 119, pp. 8410–8421, 2014, doi: 10.1002/2014JC009970.

[267] P. Chen, D. Pan, Z. Mao, and H. Liu, "A feasible calibration method for type 1 open ocean water LiDAR data based on bio-optical models," *Remote Sens.*, vol. 11, no. 2, pp. 1–11, 2019, doi: 10.3390/rs11020172.

[268] J. H. Churnside and R. D. Marchbanks, "Calibration of an airborne oceanographic lidar using ocean backscattering measurements from space," *Opt. Exp.*, vol. 27, no. 8, 2019, Art. no. A536, doi: 10.1364/oe.27.00a536.

[269] V. S. Shamanaev, "Detection of schools of marine fish using polarization laser sensing," *Atmos. Ocean. Opt.*, vol. 31, no. 4, pp. 358–364, 2018, doi: 10.1134/S1024856018040103.

[270] P. Launeau, M. Giraud, M. Robin, and A. Baltzer, "Full-waveform LiDAR fast analysis of a moderately turbid bay in western France," *Remote Sens.*, vol. 11, no. 2, 2019, Art. no. 117, doi: 10.3390/rs11020117.

[271] P. Westfeld, H.-G. Maas, K. Richter, and R. Weiß, "Analysis and correction of ocean wave pattern induced systematic coordinate errors in airborne LiDAR bathymetry," *ISPRS J. Photogrammetry Remote Sens.*, vol. 128, pp. 314–325, 2017.

[272] Y. Ma *et al.*, "Satellite-derived bathymetry using the ICESat-2 lidar and Sentinel-2 imagery datasets," *Remote Sens. Environ.*, vol. 250, 2020, Art. no. 112047.

[273] D. Su, F. Yang, Y. Ma, K. Zhang, J. Huang, and M. Wang, "Classification of coral reefs in the South China Sea by combining airborne LiDAR bathymetry bottom waveforms and bathymetric features," *IEEE Trans. Geosci. Remote Sens.*, vol. 57, no. 2, pp. 815–828, Feb. 2019, doi: 10.1109/TGRS.2018.2860931.

[274] E. White, F. Mohseni, and M. Amani, "Coral reef mapping using remote sensing techniques and a supervised classification algorithm," *Adv. Environ. Eng. Res.*, vol. 2, no. 4, Aug. 2021, Art. no. 12, doi: 10.21926/aeer.2104028.

[275] M. Amani, C. Macdonald, S. Mahdavi, M. Gullage, and J. So, "Aquatic vegetation mapping using machine learning algorithms and bathymetric lidar data: A case study from newfoundland, Canada," *J. Ocean Technol.*, vol. 16, 2021, Art. no. 3. [Online]. Available: https://www.thejot.net/article-preview/?show_article_preview=1278

[276] R. A. Branch *et al.*, "Airborne LiDAR measurements and model simulations of tides, waves, and surface slope at the mouth of the Columbia river," *IEEE Trans. Geosci. Remote Sens.*, vol. 56, no. 12, pp. 7038–7048, Dec. 2018, doi: 10.1109/TGRS.2018.2847561.

[277] H. Kim, Y. Kim, and J. Lee, "Tidal creek extraction from airborne LiDAR data using ground filtering techniques," *KSCE J. Civil Eng.*, vol. 24, no. 9, pp. 2767–2783, 2020, doi: 10.1007/s12205-020-2336-8.

[278] D. Eleftherakis and R. Vicen-Bueno, "Sensors to increase the security of underwater communication cables: A review of underwater monitoring sensors," *Sensors*, vol. 20, no. 3. 2020, Art. no. 737, doi: 10.3390/s20030737.

[279] L. Mayer *et al.*, "The Nippon Foundation—GEBCO seabed 2030 project: The quest to see the World's Oceans completely mapped by 2030," *Geosciences*, vol. 8, no. 2. 2018, Art. no. 63, doi: 10.3390/geosciences8020063.

[280] A. Purser *et al.*, "Ocean floor observation and bathymetry system (OFOBS): A new towed camera/sonar system for deep-sea habitat surveys," *IEEE J. Ocean. Eng.*, vol. 44, no. 1, pp. 87–99, Jan. 2018.

[281] Z. A. Wang *et al.*, "Advancing observation of ocean biogeochemistry, biology, and ecosystems with cost-effective in situ sensing technologies," *Front. Mar. Sci.*, vol. 6, 2019, Art. no. 519.

[282] A.-C. Wölfl *et al.*, "Seafloor mapping–the challenge of a truly global ocean bathymetry," *Front. Mar. Sci.*, vol. 6, 2019, Art. no. 283.

[283] J. P. Fish and H. A. Carr, *Sound Underwater Images: A Guide to the Generation and Interpretation of Side Scan Sonar Data*. Orleans, MA, USA: Lower Cape, 1990.

[284] J. K. Horne, "Acoustic approaches to remote species identification: A review," *Fisheries Oceanogr.*, vol. 9, no. 4, pp. 356–371, Dec. 2000, doi: 10.1046/j.1365-2419.2000.00143.x.

[285] G. A. Meadows, "A review of low cost underwater acoustic remote sensing for large freshwater systems," *J. Great Lakes Res.*, vol. 39, no. S1, pp. 173–182, 2013, doi: 10.1016/j.jglr.2013.02.003.

[286] M. J. Carron, P. Vogt, and W.-Y. Jung, "A proposed international Long-term project to systematically map the world's ocean floors from beach to trench: GOMaP (Global ocean mapping program)," *Int. Hydrogr. Rev.*, vol. 2, pp. 1–15, 2001.

[287] S. Reed, I. T. Ruiz, C. Capus, and Y. Petillot, "The fusion of large scale classified side-scan sonar image mosaics," *IEEE Trans. Image Process.*, vol. 15, no. 7, pp. 2049–2060, Jul. 2006, doi: 10.1109/TIP.2006.873448.

[288] A. D. Waite, *Sonar For Practising Engineers*. Hoboken, NJ, USA: Wiley, 2002.

[289] C. R. Barnes, M. M. R. Best, F. R. Johnson, L. Pautet, and B. Pirenne, "Challenges, benefits and opportunities in operating cabled ocean observatories: Perspectives from NEPTUNE Canada," in *Proc. IEEE Symp. Underwater Technol. Workshop Sci. Use Submarine Cables Related Technol.*, 2011, pp. 1–7.

[290] C. J. Brown, J. Beaudoin, M. Brissette, and V. Gazzola, "Multi-spectral multibeam echo sounder backscatter as a tool for improved seafloor characterization," *Geosciences*, vol. 9, no. 3. 2019, Art. no. 126, doi: 10.3390/geosciences9030126.

[291] M. Mitchley and M. Sears, "Searching for seafloor massive sulfides: A quantitative review of high-resolution methods in deep sea sonar bathymetry for mining applications," *Mar. Geophysical Res.*, vol. 35, no. 2, pp. 157–174, 2014, doi: 10.1007/s11001-014-9219-7.

[292] L. Reshitnyk, M. Costa, C. Robinson, and P. Dearden, "Evaluation of Worldview-2 and acoustic remote sensing for mapping benthic habitats in temperate coastal Pacific waters," *Remote Sens. Environ.*, vol. 153, pp. 7–23, 2014. [Online]. Available: https://doi.org/10.1016/j.rse.2014.07.016

[293] J. J. Schultz, C. A. Healy, K. Parker, and B. Lowers, "Detecting submerged objects: The application of side scan sonar to forensic contexts," *Forensic Sci. Int.*, vol. 231, no. 1, pp. 306–316, 2013. [Online]. Available: https://doi.org/10.1016/j.forsciint.2013.05.032

[294] X. B. Luo, D. M. Xu, J. J. Hu, and X. M. Hu, "Application research of 3D imaging sonar system in salvage process," *Appl. Mech. Mater.*, vol. 643, pp. 279–282, 2014. [Online]. Available: https://doi.org/10.4028/www.scientific.net/AMM.643.279

[295] C. J. Brown and P. Blondel, "Developments in the application of multibeam sonar backscatter for seafloor habitat mapping," *Appl. Acoust.*, vol. 70, no. 10, pp. 1242–1247, 2009. [Online]. Available: https://doi.org/10.1016/j.apacoust.2008.08.004

[296] J. E. Hughes Clarke, L. A. Mayer, and D. E. Wells, "Shallow-water imaging multibeam sonars: A new tool for investigating seafloor processes in the coastal zone and on the continental shelf," *Mar. Geophysical Res.*, vol. 18, no. 6, pp. 607–629, 1996, doi: 10.1007/BF00313877.

[297] A. Grządziel, "Results from developments in the use of a scanning sonar to support diving operations from a rescue ship," *Remote Sens.*, vol. 12, no. 4, 2020, Art. no. 693, doi: 10.3390/rs12040693.

[298] M. P. Hayes and P. T. Gough, "Synthetic aperture sonar: A review of current status," *IEEE J. Ocean. Eng.*, vol. 34, no. 3, pp. 207–224, Jul. 2009, doi: 10.1109/JOE.2009.2020853.

[299] A. P. Lyons and D. C. Brown, "The impact of the temporal variability of seafloor roughness on synthetic aperture sonar repeat–Pass interferometry," *IEEE J. Ocean. Eng.*, vol. 38, no. 1, pp. 91–97, Jan. 2013, doi: 10.1109/JOE.2012.2209231.

[300] P. Wille, *Sound Images of the Ocean: In Research and Monitoring*. Berlin, Germany: Springer, 2005.

[301] M. U. Gumusay, T. Bakirman, I. Tuney Kizilkaya, and N. O. Aykut, "A review of seagrass detection, mapping and monitoring applications using acoustic systems," *Eur. J. Remote Sens.*, vol. 52, no. 1, pp. 1–29, Jan. 2019, doi: 10.1080/22797254.2018.1544838.

[302] L. An, E. Rignot, R. Millan, K. Tinto, and J. Willis, "Bathymetry of Northwest Greenland using 'Ocean melting Greenland' (OMG) high-resolution airborne gravity and other data," *Remote Sens.*, vol. 11, no. 2, 2019, Art. no. 131, doi: 10.3390/rs11020131.

[303] J. E. Arndt *et al.*, "The international bathymetric chart of the Southern Ocean (IBCSO) version 1.0—A new bathymetric compilation covering circum-Antarctic waters," *Geophys. Res. Lett.*, vol. 40, no. 12, pp. 3111–3117, Jun. 2013, doi: 10.1002/grl.50413.

[304] M. Hamana and T. Komatsu, "Real-Time classification of seagrass meadows on flat bottom with bathymetric data measured by a narrow multibeam sonar system," *Remote Sens.*, vol. 8, no. 2, 2016, Art. no. 96, doi: 10.3390/rs8020096.

[305] C. L. y Royo *et al.*, "The seagrass posidonia oceanica as indicator of coastal water quality: Experimental intercalibration of classification systems," *Ecological Indicators*, vol. 11, no. 2, pp. 557–563, 2011.

[306] S. Collings, N. A. Campbell, and J. K. Keesing, "Quantifying the discriminatory power of remote sensing technologies for benthic habitat mapping," *Int. J. Remote Sens.*, vol. 40, no. 7, pp. 2717–2738, Apr. 2019, doi: 10.1080/01431161.2018.1531316.

[307] C. J. Brown, S. J. Smith, P. Lawton, and J. T. Anderson, "Benthic habitat mapping: A review of progress towards improved understanding of the spatial ecology of the seafloor using acoustic techniques," *Estuarine Coastal Shelf Sci.*, vol. 92, no. 3, pp. 502–520, 2011. [Online]. Available: https://doi.org/10.1016/j.ecss.2011.02.007

[308] B. M. Sabol, R. Eddie Melton, R. Chamberlain, P. Doering, and K. Haunert, "Evaluation of a digital echo sounder system for detection of submersed aquatic vegetation," *Estuaries*, vol. 25, no. 1, pp. 133–141, 2002, doi: 10.1007/BF02696057.

[309] J. Barrell, J. Grant, A. Hanson, and M. Mahoney, "Evaluating the complementarity of acoustic and satellite remote sensing for seagrass landscape mapping," *Int. J. Remote Sens.*, vol. 36, no. 16, pp. 4069–4094, Aug. 2015, doi: 10.1080/01431161.2015.1076208.

[310] D. P. Williams, "The mondrian detection algorithm for sonar imagery," *IEEE Trans. Geosci. Remote Sens.*, vol. 56, no. 2, pp. 1091–1102, Feb. 2018.

[311] K. Mukherjee, S. Gupta, A. Ray, and S. Phoha, "Symbolic analysis of sonar data for underwater target detection," *IEEE J. Ocean. Eng.*, vol. 36, no. 2, pp. 219–230, Apr. 2011.

[312] B. Zhu, X. Wang, Z. Chu, Y. Yang, and J. Shi, "Active learning for recognition of shipwreck target in side-scan sonar image," *Remote Sens.*, vol. 11, no. 3, 2019, doi: 10.3390/rs11030243.

[313] M. Eslami Nazari, W. Huang, and C. Zhao, "Radio frequency interference suppression for HF surface wave radar using CEMD and temporal windowing methods," *IEEE Geosci. Remote Sens. Lett.*, vol. 17, no. 2, pp. 212–216, Feb. 2020, doi: 10.1109/LGRS.2019.2920092.

[314] Y. Wang and W. Huang, "An algorithm for wind direction retrieval from X-band marine radar images," *IEEE Geosci. Remote Sens. Lett.*, vol. 13, no. 2, pp. 252–256, Feb. 2016.

[315] M. Eslami Nazari and W. Huang, "An analytical solution of the electric field excited by a vertical electric dipole above a lossy half-space: From radio to microwave frequencies," *IEEE Trans. Antennas Propag.*, vol. 68, no. 11, pp. 7517–7529, Nov. 2020, doi: 10.1109/TAP.2020.2996768.

[316] M. E. Nazari and W. Huang, "An analytical solution of electromagnetic radiation of a vertical dipole over a layered half-space," *IEEE Trans. Antennas Propag.*, vol. 68, no. 2, pp. 1181–1185, Feb. 2019.

[317] D. E. Barrick, "Theory of HF and VHF propagation across the rough sea, 1, the effective surface impedance for a slightly rough highly conducting medium at grazing incidence," *Radio Sci.*, vol. 6, no. 5, pp. 517–526, 1971.

[318] D. E. Barrick, "Theory of HF and VHF propagation across the rough sea, 2, application to HF and VHF propagation above the sea," *Radio Sci.*, vol. 6, no. 5, pp. 527–533, 1971.

[319] M. Eslami Nazari and A. Ghorbani, "Predicting a three-dimensional radar coverage area : Introducing a new method based on propagation of radio waves," *IEEE Antennas Propag. Mag.*, vol. 58, no. 1, pp. 28–34, Feb. 2016, doi: 10.1109/MAP.2015.2501238.

[320] E. D. R. Shearman, "Propagation and scattering in MF/HF groundwave radar," *IEE Proc. F Commun. Radar Signal Process.*, vol. 130, no. 7, pp. 579–590, 1983, doi: 10.1049/ip-f-1.1983.0092.

[321] D. D. Crombie, "Doppler spectrum of sea echo at 13.56 mc./s," *Nature*, vol. 175, no. 4459, pp. 681–682, 1955.

[322] E. D. R. Shearman, "Remote sensing of the sea-surface by dekametric radar," *Radio Electron. Eng.*, vol. 50, no. 11, pp. 611–623, 1980.

[323] R. H. Khan and D. Power, "Aircraft detection and tracking with high frequency radar," in *Proc. Int. Radar Conf.*, 1995, pp. 44–48, doi: 10.1109/RADAR.1995.522517.

[324] D. Green, E. Gill, and W. Huang, "An inversion method for extraction of wind speed from high-frequency ground-wave radar oceanic backscatter," *IEEE Trans. Geosci. Remote Sens.*, vol. 47, no. 10, pp. 3338–3346, 2009, doi: 10.1109/TGRS.2009.2022944.

[325] R. Stewart, *Introduction To Physical Oceanography*. College Station, TX, USA: Texas A&M Univ., 2008.

[326] A. Kitaigorodskii, "Applications of the theory of similarity to the analysis of wind-generated wave motion as a stochastic process," *Izv. Geophys. Ser. Acad. Sci., USSR*, vol. 9, pp. 398–398, 1962.

[327] W. J. Pierson Jr., and L. Moskowitz, "A proposed spectral form for fully developed wind seas based on the similarity theory of S. A. Kitaigorodskii," *J. Geophys. Res.*, vol. 69, no. 24, pp. 5181–5190, 1964. [Online]. Available: https://doi.org/10.1029/JZ069i024p05181

[328] M. E. Nazari, W. Huang, and C. Zhao, "Dense radio frequency interference cancellation by CEMD and temporal windowing processing for HFSW radar," in *Proc. Marseille*, 2019, pp. 1–4, doi: 10.1109/OCEANSE.2019.8867174.

[329] E. D. R. Shearman, "Radio science and oceanography," *Radio Sci.*, vol. 18, no. 3, pp. 299–320, 1983, doi: 10.1029/RS018i003p00299.

[330] M. D. E. Turley, "Hybrid CFAR techniques for HF radar," in *Proc. Radar*, 1997, pp. 36–40, doi: 10.1049/cp:19971627.

[331] L. Z. H. Chuang, Y. Chung, and S. T. Tang, "A simple ship echo identification procedure with seasonde HF radar," *IEEE Geosci. Remote. Sens. Lett.*, vol. 12, no. 12, pp. 2491–2495, Dec. 2015, doi: 10.1109/LGRS.2015.2487363.

[332] S. Grosdidier and A. Baussard, "Ship detection based on morphological component analysis of high-frequency surface wave radar images," *IET Radar, Sonar Navig.*, vol. 6, no. 9, pp. 813–821, 2012.

[333] A. Dzvonkovskaya, K.-W. Gurgel, H. Rohling, and T. Schlick, "Low power high frequency surface wave radar application for ship detection and tracking," in *Proc. Int. Conf. Radar*, 2008, pp. 627–632.

[334] S. Park, C. J. Cho, B. Ku, S. Lee, and H. Ko, "Simulation and ship detection using surface radial current observing compact HF radar," *IEEE J. Ocean. Eng.*, vol. 42, no. 3, pp. 544–555, Jul. 2017, doi: 10.1109/JOE.2016.2603792.

[335] Z. Tian *et al.*, "Wave-Height mapping from second-order harmonic peaks of wide-beam HF radar backscatter spectra," *IEEE Trans. Geosci. Remote Sens.*, vol. 58, no. 2, pp. 925–937, Feb. 2020, doi: 10.1109/TGRS.2019.2941823.

[336] H. Zhou and B. Wen, "Wave height extraction from the first-order bragg peaks in high-frequency radars," *IEEE Geosci. Remote. Sens. Lett.*, vol. 12, no. 11, pp. 2296–2300, Nov. 2015, doi: 10.1109/LGRS.2015.2472976.

[337] K. J. Hickey, E. W. Gill, J. A. Helbig, and J. Walsh, "Measurement of ocean surface currents using a long-range, high-frequency ground wave radar," *IEEE J. Ocean. Eng.*, vol. 19, no. 4, pp. 549–554, Oct. 1994, doi: 10.1109/48.338381.

[338] B. J. Lipa and D. E. Barrick, "Extraction of sea state from HF radar sea echo: Mathematical theory and modeling," *Radio Sci.*, vol. 21, no. 1, pp. 81–100, 1986. [Online]. Available: https://doi.org/10.1029/RS021i001p00081

Meisam Amani (Senior Member, IEEE) received the B.Eng. degree in geomatics engineering from the University of Tabriz, Tabriz, Iran, in 2012, the M.Eng. degree in remote sensing engineering from the K. N. Toosi University of Technology, Tehran, Iran, in 2014, and the Ph.D. degree in electrical engineering from the Memorial University of Newfoundland, St. John's, Canada, in 2018.

He is currently a Senior Remote Sensing Engineer and the Key Specialty Leader of Data Analytics with Wood Environment and Infrastructure Solutions, Ottawa, ON, Canada, where he manages and leads various industrial, governmental, and academic remote sensing projects worldwide. Over the past 11 years, he has worked on different applications of remote sensing, including but not limited to land cover/land use classification, soil moisture estimation, drought monitoring, water quality assessment, watershed management, power/transmission line monitoring, fog detection and nowcasting, and ocean wind estimation. To do these, he has utilized various remote sensing datasets (e.g., UAV, optical, LiDAR, SAR, scatterometer, radiometer, and altimeter) along with different machine learning and big data processing algorithms.

Dr. Amani is an Associate Editor for the IEEE JOURNAL OF SELECTED TOPICS IN APPLIED EARTH OBSERVATIONS AND REMOTE SENSING and the Lead Guest Editor for a Special Issue in the Remote Sensing journal. He is also a regular Reviewer in about 15 international remote sensing journals. He was the recipient of the prestigious Professional Engineers and Geoscientists Newfoundland and Labrador Environmental Award in 2020 due to his contribution to wetland mapping in Canada using advanced machine learning and big data processing algorithms.
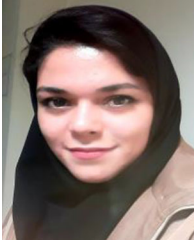
Farzane Mohseni received the B.Sc. degree in geodesy and geomatics and the M.Sc. degree in remote sensing in 2015 and 2017, respectively, from the K. N. Toosi University of Technology, Tehran, Iran, where she is currently working toward the Ph.D. degree in remote sensing.

Her research interests include soil hydrology, ground water estimation, remote sensing, water resource management, disaggregation of coarse-scale radiometric soil moisture products, and land cover mapping.

Abbas Salehi received the B.Sc. degree in geomatics engineering from the National Cartographic Center (NCC), Tehran, Iran, in 2013, and the master's degree in photogrammetry from the K. N. Toosi University of Technology, Tehran, Iran, in 2016.

His research interests include LiDAR, point cloud processing, flood mapping, and three-dimensional building modeling.

Nasir Farsad Layegh received the B.Sc. degree from Tabriz University, Tabriz, Iran, in 2012 and the M.Sc. degrees from Lund University, Lund, Sweden and from the University of Twente, Enschede, The Netherlands, in 2017, all in geo-information science and earth observation.
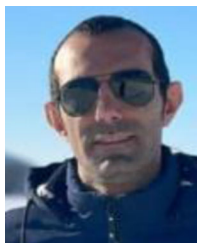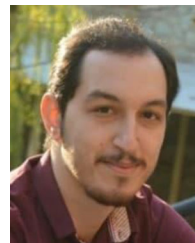
In 2017, he joined as a (Geo) Data Analyst Fugro B.V., Leidschendam, Netherlands, where he worked on LiDAR and GNSS data for railway infrastructure maintenance. In 2019, he got promoted to Technical Team Leader to lead the team of data analysts in processing big (geo) data to model the railway using LiDAR data. In late 2021, he joined Capgemini Invent, Utrecht, The Netherlands, as a Manager and Senior Data Scientist. He has authored or coauthored publications in the field of remote sensing and GIS.

Seyed Ali Ahmadi received the B.Sc. degree in surveying engineering from the Faculty of Geodesy and Geomatics, K. N. Toosi University of Technology, Tehran, Iran, in 2015, and the M.Sc. degree in remote sensing from the Faculty of Geodesy and Geomatics, K. N. Toosi University of Technology, Tehran, Iran, in 2017.

He worked on image classification and segmentation techniques, machine learning algorithms, and LiDAR data processing. His thesis was focused on classifying hyperspectral and LiDAR datasets by combining spectral and spatial features in order to increase the classification accuracy. He is currently researching on the Ph.D. thesis with the K. N. Toosi University of Technology. His research interests include machine learning, deep learning, LiDAR data processing, hyperspectral image analysis, data fusion, image processing, and computer vision techniques for remote sensing and earth observation applications.

Mohsen Eslami Nazari (Member, IEEE) received the B.Sc. degree in electrical engineering from the University of Kashan, Kashan, Iran, in 2010, and the M.Sc. degree from the Amirkabir University of Technology (Tehran Polytechnic), Tehran, Iran, in 2014. He is currently working toward the Ph.D. degree in electrical engineering with the Memorial University of Newfoundland, St. John's, NL, Canada.

His current research interests include applied electromagnetism, analytical, and numerical techniques in electromagnetic wave scattering from layered media, and microstrip antennas.

Hamid Ebrahimy received the M.S. degree in remote sensing and GIS from the University of Tabriz, Tabriz, Iran, in 2016.

He is currently a Researcher with the Center for Remote Sensing and GIS Research, Shahid Beheshti University, Tehran, Iran. His research interests include land covermapping, MODISLST downscaling, map accuracy assessment, and big remotely sensed data processing.

Farzam Fatolazadeh received the B.Sc. degree in civil/surveying engineering from the University of Tafresh, Tafresh, Iran, in 2012 and the M.Sc. degree in geomatics/geodesy from the K. N. Toosi University of Technology, Tehran, Iran, in 2015. He is currently working toward the Ph.D. degree in improving and downscaling GRACE and GRACE-FO data for the retrieval of terrestrial water storage and groundwater storage changes at finer scale with the Applied Geomatics Department, Université de Sherbrooke, Sherbrooke, QC, Canada.

Over the past nine years, he has worked on different applications of satellite gravimetric of GRACE and GRACE-FO on and inside the Earth, including earthquake, surface water and groundwater management, drought monitoring, and vegetation growth. He has developed tools, analytical models along with different statistical algorithms to observe and analyze the time variations in the Earth's gravity field as observed from space using GRACE/GRACE-FO satellites. He is currently improving and downscaling spatio-temporal resolution of GRACE/GRACE-FO data to better characterize local changes of different hydrological parameters in Canada, particularly in Canadian Prairies.

Mr. Fatolazadeh is a Reviewer in different international remote sensing and hydrological journals.

Arsalan Ghorbanian received the B.Sc. degree in geodesy and geomatics engineering in 2016 and the M.Sc. degree in remote sensing in 2018 from the K. N. Toosi University of Technology, Tehran, Iran, where he is currently working toward a Ph.D. degree in remote sensing.

His research interests include LULC mapping, geo-big data processing, wetland and mangrove studies, satellite image and video processing, urban heat island studies, and soil moisture estimation.

Mr. Ghorbanian is a Reviewer in several international remote sensing journals and is currently a Guest Editor for a Special Issue in the Remote Sensing journal. He was with different types of remote sensing datasets during his academic career, including multispectral, hyperspectral, synthetic aperture radar, and thermal infrared data. He was recognized as an excellent student during his B.Sc. degree and as an excellent student and ranked first during his M.Sc. degree by the K. N. Toosi University of Technology.

Shuanggen Jin (Senior Member, IEEE) was born in Anhui, China, in September 1974. He received the B.Sc. degree from Wuhan University, Wuhan, China, in 1999 and the Ph.D. degree from the University of Chinese Academy of Sciences, Beijing, China, in 2003, both in geodesy.

He is currently a Professor and the Dean with the Nanjing University of Information Science and Technology, Nanjing, China, and also a Professor with Shanghai Astronomical Observatory, CAS, Shanghai, China. He has authored and coauthored more than 500 papers in peer-reviewed journals and proceedings, ten patents/software copyrights, and ten books/monographs with more than 8000 citations and H-index>50. His main research interests include satellite navigation, remote sensing, and space/planetary exploration.

Prof. Jin was the President of International Association of Planetary Sciences (2015–2019), the President of the International Association of CPGPS (2016–2017), the Chair of IUGG Union Commission on Planetary Sciences (2015–2023), the Editor-in-Chief of *International Journal of Geosciences and Geoscience Letters*, an Associate Editor for the IEEE TRANSACTIONS ON GEOSCIENCE AND REMOTE SENSING and *Journal of Navigation*, an Editorial Board Member of *Remote Sensing, GPS Solutions,* and *Journal of Geodynamics*. He has received 100-Talent Program of CAS, Leading Talent of Shanghai. He is an IAG Fellow, IUGG Fellow, World Class Professor of Ministry of Education and Cultures, Indonesia, Chief Scientist of National Key R&D Program, China, Member of Russian Academy of Natural Sciences, Member of European Academy of Sciences, Member of Turkish Academy of Sciences, and Member of Academia Europaea.

Sahel Mahdavi received the Ph.D. degree in electrical engineering from the Memorial University of Newfoundland, St. John's, Canada, in 2018.

She is currently affiliated with the Data Analytics team at Wood Environment and Infrastructure Solutions, Ottawa, ON, Canada. Having almost ten years of academic and industrial background in Remote Sensing, she is familiar with a wide array of topics relevant to RS/GIS and their applications in various environmental aspects. She also coauthored a book entitled *Principles of SAR Remote Sensing* and has authored more than 40 peer-reviewed journals. Her research interests include object-based wetland classification using a combination of optical and full-polarimetric SAR data, feature selection, soil moisture retrieval using SAR images, image segmentation, speckle reduction in SAR images, target detection in multispectral optical images, and the relationship between environmental conditions and SAR images.

Dr. Mahdavi was a member of a provincial project on wetland classification during her Ph.D. when she identified the problem with wetland classification using remote sensing and, subsequently, proposed a novel scheme for wetland mapping. She was the recipient of the Professional Engineers and Geoscientists Newfoundland and Labrador Environmental Award in 2020, the Emera Graduate Scholarship for Distinctive Women in Engineering for three consecutive years (2016–2018), and Newfoundland and Labrador Branch of Canadian Institute of Geomatics Scholarship in 2015.

Armin Moghimi received the B.Sc. degree in geomatics engineering from Shahid Beheshti University (formerly Geomatics College of National Cartographic Center), Tehran, Iran, in 2013, and the M.Sc. degree in photogrammetry engineering in 2015 from the K. N. Toosi University of Technology, Tehran, Iran, where he is currently working toward the Ph.D. degree in photogrammetry and remote sensing.

His research interests include change detection techniques, image preprocessing, image registration, and machine learning.